Advancement of Biomaterials Characterization and Tissue Engineering to Model Human Immunity

Jonathan Michael Zatorski

Crown Point, Indiana

B.S. Chemistry, Olivet Nazarene University, 2018

A Dissertation presented to the Graduate Faculty of the University of Virginia in Candidacy for the Degree of Doctor of Philosophy

Department of Chemistry

University of Virginia

May 2024

Abstract

Amidst surging drug costs and high clinical trial failure rates, the successful development of new therapeutics demands drug testing platforms having high accuracy to human physiology. Changes in regulatory oversight, such as the FDA Modernization Act 2.0, echo the desperate need for better models. The fields of tissue engineering and bioanalytical chemistry have innovated for decades toward meeting this need, resulting in organ-on-chip technology. As immunomodulating agents are among the most expensive and failure prone areas of medicine, models of the human adaptive immune response and the lymph node are desperately needed.

Despite major advances in this space, the human immune system poses inherent challenges for advanced models. While organ-on-chip technology has enabled effective modeling of tissue-properties, a major gap in the field is a lack of established immune models in the context of organ-on-chip models. In particular few models exist for modeling the complex processes that lead to the response to infection or vaccine.

Chapter 2 of this thesis describes effective modeling of T-cell-dependent B cell activation in an organ-on-chip platform. This adaptive immune process was exploited by enabling TCR/BCR independent and dependent cross-talk. Cell-cell interactions were then inhibited with a clinically available JAK inhibitor. Chapter 3 describes efforts to construct this immune modeling platform from materials suitable for manufacturing at scale.

Chapters 4 and 5 focus on more fundamental advancements in tissue engineering and analytical chemistry. First, technological advancements regarding

mimicking tissue at the microscale is discussed. Next, analytical developments for characterizing photopolymerizable biomaterials are described. Lastly, a novel method for assessing crosslinking density within light-curing materials is described, and then demonstrated for predicting the stability of biomaterials in physiological settings.

In summary, the advancements described herein have met the need for more human relevant models of adaptive immunity, and improved analytical methods for characterizing complex biomaterials. Future applications of this work will enable more accurate models of the vaccine response. In addition, applications toward modeling complex immune signaling environments such as neuroimmunity and autoimmunity are discussed. Finally, an application of the novel crosslinking density measurement is described.

Acknowledgements

The past six years have been challenging to say the least, and I would not have succeeded this far without my supportive family and friends.

First, I want thank my incredibly supportive wife, Rachel. You encouraged me, against the advice of my high-school guidance counselors, to enroll in a high-school honors chemistry course over a decade ago. You've encouraged me then every day since, and I know I could not have done this without your love and support. Moreover, I wouldn't want to. Thank you for enduring this journey with me, and working a countless number of demanding jobs along the way to support my dream. I can't wait to start our next journey together. I love you.

Mom and Dad, I am thankful for every opportunity you took to instill within me the creative thinking and internal strength that I've needed to succeed in grad school. The science fairs and college education you provided for me were enabling, but I also want you to know the little things you taught me helped me the most. Camping under the stars and cooking together taught me to appreciate nature and ultimately made me want to be a scientist. Thank you for everything.

And of course, thank you Tim and Ellen for supporting Rachel and I, providing words of encouragement, and always making me feel welcome.

Thank you, Dr. Rebecca Pompano, for mentoring me to learn scientific techniques and writing, as well as to develop my leadership skills. There were many scientific problems which I thought were unsolvable over the years, but your guidance and encouragement empowered me to persist anyway. I am a stronger and more confident scientist as a result. Thank you for helping me to recognize my own potential.

Of course this would not have been possible without my supportive, talented, and kind lab mates. You've all been wonderful to work with and have always generated positive vibes in the lab. I want to thank everyone who's been a part of the lymph-node-chip team: Jenn O., Djuro, Tochi, Ovi, Izzy, Alyssa, Jenn H., Abhinav, and the collaborating PIs Rebecca, Jenny Munson, Chance John Luckey, and the late Thomas J. Braciale. The opportunity to work with this team has been an incredibly rewarding experience. Our combined efforts have enabled much of the technology that is described in this dissertation, which is truly the state-of-the-art. I am thankful for the opportunity to have worked alongside such brilliant thinkers.

Also, I have to thank Alex Ball, without whom I might have lost my mind and quit. Drinking tea and watching River Monsters was essential to my success.

And of course, I must acknowledge my cocker spaniel poodle mix, Honeybun. No one will ever fully appreciate how much you contributed to Chapter 5 and the absolute quantification of crosslinking density within photocrosslinking hydrogels. If society allowed it, you would be a coauthor with me on this dissertation.

Table of Contents

Table of Figures

Table of Tables

1. Introduction

1.1 Societal impact of costly and unpredictive clinical trials

The high failure rate and correlated cost of producing novel therapies is a major burden on healthcare, insurance, and all people who need medicine. To elaborate, a comprehensive metanalysis off all clinical groups in 2021 estimated the cost to produce a new, clinically-approved drug ranged from $161 million to $4.5 billion. With that, the clinical trial success rate was estimated to range from 3% to 33%.[1] Two drug categories, antineoplastic (chemotherapy) and immunomodulating agents, are tied for the highest cost ($4.5B) and lowest success rate (0.3%).[2] While the high cost of drugs is a problem society has grown accustom to, its upward trend is perplexing. Contrary to Moore's law, which broadly states that efficiency improves exponentially with technological improvements, the cost-efficiency of drug development has decreased exponentially for the last sixty years[3]. This cost impacts consumers directly. The American Hospital Association reported an increase of 38.7% in drug spendings per admitted patient from 2013 to 2015, as well as an increase in overall admissions from patients not being able to afford essential medications.[4] The major concern is that these problems form a positive-feedback loop where patient admissions and staffing cuts increase simultaneously as a result of higher drug prices. Breaking this trend is therefore essential to improving drug availability and healthcare.

There are generally thought to be three main culprits:[5] (1) The first is increased regulatory scrutiny, which began promptly following the thalidomide birth-defect disaster in the mid 1960's. (2) The second root cause is the "Better-than-the-Beatles" phenomenon, which refers to the ever-growing library of effective generic medicines. Drugs are less likely to be purchased after clinical trials if their efficacy is only slightly better than a free generic, thus decreasing drug-development efficiency. (3) The third and most significant contributing factor

(~60% of price increases) is high failure rate during preclinical and clinical trials.[5] This results from traditional *in vitro* and/or animal model tests that provide false-positives. Regulatory costs and competition against past generics are economic problems that are challenging to improve upon with scientific intervention. In contrast, the high preclinical failure rate can be alleviated by engineering better predictive models. Therefore, further development of predictive drug-testing models is key to alleviating the societal burden of drug costs.

Pharmacy is broadly placing a renewed spotlight on improved preclinical models. R&D strategies from pharma leaders such as Pfizer and AstraZeneca have echoed this, having recently reported an overall refocus away from increasing the volume of drug candidates and toward improving the early-phase drug efficacy models. AstraZeneca attributed success to a new strategy with tissue-specific activity as a central focus, and Pfizer credited an "immune-AI" computational model when describing industry-leading phase II success.[6,7] While these advancements point toward a hopeful shift, there remains a major lack of effective preclinical testing models, especially within the immune-modulating class. The lack of predictive models at preclinical stages causes vaccine development in particular to be slow and failure-prone, but fundamental advances in immune engineering are needed in order to construct predictive models.

The underlying mechanisms of several issues, such as vaccine inefficacy due to treatment of disease (i.e. chemotherapy) or aging, are poorly understood and challenging to detect with current preclinical testing regimes.[8] A rare issue, vaccine associated disease enhancement, was recently observed in a subset of Denvaxia recipients during a phase II clinical trial. This went unnoticed in preclinical tests, but it is now estimated that within five years, 28% of all severe dengue cases will be attributable to the vaccine.[9] The Denvaxia failure highlights the need for more predictive, human-relevant models.

One of the key, underlying reasons that preclinical models, both animal and classic *in vitro*, fail to accurately demonstrate efficacy, is that they do not represent human tissue. Mouse and human responses, though broadly conserved, differ in numerous ways that directly impact vaccine responses, including the response to certain microbial stimuli used as adjuvants TLR7/9/11,[10,11] the expression of lymphocyte-attractive chemokines,[12,13] as well as different mechanistic roles for some cytokines, such as IL4.[14] Thus, studies of human immunology are critical for progress.[15] The FDA recognizes this more broadly, acknowledging that a fundamental cause for the high termination rate of phase I and II clinical trials is the lack of genetic diversity among animal models when compared to the human population. The drug development pipeline is indeed constricted due to the general fact that experiments, in the traditional sense, cannot be performed in humans. Toward alleviating this burden, the Biden Administration signed the FDA Modernization Act 2.0 (2022) into law, which enables the use of specific alternatives to animal testing during preclinical tests. These include stem cells, organoids, organs-on-chips, and AI models.[16]

Therefore, fundamental advancements in tissue engineering, toward predictive model building, are needed to alleviate problem of high drug failure rate, rising drug costs, and human health in general. In particular, tissue engineering developments that progress toward predicting immune-modulation (vaccines, immunosuppressants, etc.) is where the greatest need currently exists.

1.2 Capacity of tissue engineered models to model human physiology and assess drug efficacy.

Traditional *in vitro* and *in vivo* models for predicting efficacy and safety are essential, but have limitations that generate a gap in understanding. *In vitro* models effectively optimize analytical readouts at the cost of tissue-level physiology. Cells in a dish are easy to characterize and drug, but this advantage comes at the loss of the extracellular matrix (ECM), cell

heterogeneity, interstitial fluid flow, and inter-organ communication. On the contrary, *in vivo* models retain all tissue-level properties, but are more challenging to precisely analyze.[17] Of course, the most fundamental disadvantage of *in vivo* animal models is their subtle dissimilarity to human physiology, which is a burden that scientists have accepted for centuries.[13,14]

Bioanalytical tools that arise from tissue engineering advancements have the potential to blaze a new path for predicting drug efficacy.[16–18] On a basic level, resuspending cells within an ECM mimic such as a collagen hydrogel enables cells to move and grow in three dimensions along fibers that resemble tissue. Cells in this system will exhibit a morphology more like that seen in tissue, having cytoplasm extensions and star-like shapes in gel, as opposed to round balls in a dish. This basic advancement in biomimicry is fundamental to organoid and artificial tissue technology that has contributed to both fundamental science and regenerative medicine over the past four decades. To further increase biomimicry, perfusive fluid flow has been incorporated into 3D cell cultures to mimic blood, cerebral-spinal, or lymphatic flow.[19,20]

Early organ-on-chip (OOC) models emerged by combining 3D culture with microfluidic channels, enabling perfusion.[21] Mimicking tissue in this way enables fluidic control, which increases both biomimicry and analytical precision. Beyond that, multiple different organ-on-chip models have been connected in a fluidic sequence to build multi-organ-models or “human-on-a-chip (HOC).”[22–24] This emerging technology enables assessment of systems level physiology, which has direct applications for drug-efficacy and safety testing. The goal of these models is to gain human-relevant insight on adsorption, distribution, metabolism, and excretion of drug candidates prior to clinical trials, and enable human mechanistic translational research.

Table 1-1. 2D *in vitro and in vivo systems leave gaps that tissue engineered systems can fill.*

		Tissue engineered models			
	 2D Cell culture	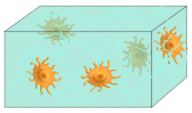 3D cell culture	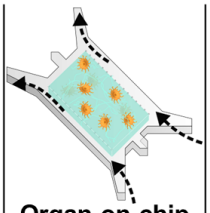 Organ-on-chip	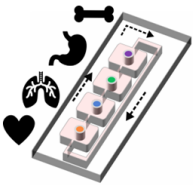 Human-on-chip	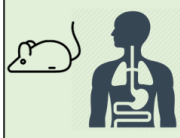 In vivo /Patient
Spatially Organized cells					✓
Extracellular matrix		✓	✓	✓	✓
Blood, lymphatic flow			✓	✓	✓
Multi-organ communication				✓	✓
Defined chemical stimulation (per cell)	✓	✓	✓	✓	
Quantifiable secretion (per cell)	✓	✓	✓		
Simple imaging	✓	✓	✓		
Simple fabrication	✓				
Downstream analysis	✓	✓	✓		

Advancements are needed at each level (3D culture, OOC, and HOC) to better mimic human tissue and physiology, but a major gap in the field is a lack of immune-organ models. Considering that immune modulating agents are among the most expensive drugs to develop and the least likely to pass clinical trials, developments in immune-tissue engineering are urgently needed. **As such, this dissertation will focus primarily on developments at the 3D culture and organ-on-chip level, with future applications related to connecting immune models to multi-organ models discussed at its conclusion.**

1.3Challenges of modeling the human immune response

At homeostasis, the adaptive immune processes in the human lymph node enable the body to respond to infection and fight cancer, among other things.[25,26] In the diseased state, the lymph node enables autoimmunity (as in Systemic lupus erythematosus), harbors viral-infected cells, becomes cancerous (as in Lymphoma) and can enable cancer metastasis.[27–29] Of the

numerous processes that compose the adaptive immune response, a key regulatory process is the T-cell-dependent B cell activation that occurs in the lymph node.[30] As such, the lymph node is a central focus when designing immunomodulators like immunosuppressants and vaccines. Despite this, there are few tissue-engineered models of the human lymph node.

A major challenging when modeling the lymph node is accurately recapitulating the balance between its spatial organization and related physiology. This is because the lymph node anatomy is highly complex.[25] Antigen-containing lymph fluid enters through afferent lymphatics into an outer sinus that envelopes a cortex. Fluid flows from the sinus into a cortex, and then leaves through the efferent lymphatics. In the cortex, B cells are arranged in follicles that surround a central T cell zone.

The cell signaling processes that underly the response to infection (or vaccine) are dependent on this organization (Fig. 1-1). After vaccination, antigen drains to the LN through the lymphatics and conduits to cognate dendritic and B cells. Through high endothelial venules, T cells enter the T cell zone, where they become activated by dendritic cells. They then skew to TFH cells and upregulate CXCR5, which enables their migration to the B zone and subsequent T cell help for B cell activation. Activated B cells mature and proliferate as antibody-secreting

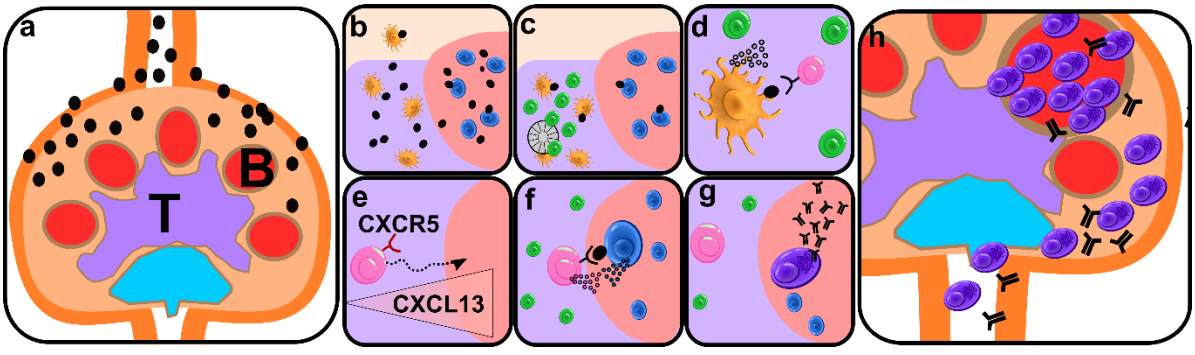

Figure 1-1. Steps of a vaccine response are linked to the LN spatial organization. (a) antigen (black) drainage. (b) Dendritic cell (yellow) and B cell (blue) uptake. (c) T cell (green) homing to the LN. (d) Antigen presentation between DC and T cell, and Tfh skewing (pink). (e) Tfh homing to the follicle border. (f) T-cell-dependent B cell activation (T cell help). (g) Plasmablast differentiation (purple) and antibody secretion. (h) egress from the LN.

plasmablasts, and finally egress the lymph node. The cells that orchestrate this process are essential, but also transient and rare.

Inherent properties of immune cells create numerous challenges for modeling. The transient cell types involved are often sensitive, which demands a highly biocompatible system. In addition, an appropriate source for cells in their unperturbed, naïve state is not easily accessible. Cell lines like Jurkat T cells, for example, are not compatible for many immune modeling approaches, as they are isolated from a leukemia patient and cannot recapitulate some wild-type T cell behaviors. The most appropriate source would be to isolate lymphocytes from human lymph node tissue. Surgically-removed tonsillar lymphoid tissue has been studied to meet this need. However, that tissue often already inflamed and responding to a challenge. The next best source, and what was utilized for the majority of the work described within this dissertation, is human peripheral blood mononucleocytes (PBMCs), from which T and B lymphocytes were isolated. Adding to the challenge, T cells and B cells specific to any one antigen ("precursor frequency"), often on the order of 1 in 10^5 - 10^6 cells in a naïve population, which means that a microscale culture have only 0 or 1 of such cells.

Other challenges relate to the necessity for autologous cells in certain models. If an OOC contains an epithelial cell layer, the immune cells may need to be derived from the same human donor. This can be difficult when OOCs contain primary cells, or impossible when OOCs utilize immortalized cell lines. In addition, donor-to-donor variability can produce irreproducible results on chip. For example, T and B cell percentages in both tonsils and peripheral blood, as well as their respective naïve and memory populations, vary significantly with age and ancestral background[31,32].These inconsistencies can be viewed as a positive or negative, depending on the approach. To illustrate, a model might include the heterogenous population to reflect human variability. On the other hand, if attempting to use purified lymphocyte populations, the model could be irreproducible with certain donors.

A final, broader challenge is that nearly all our knowledge of immunity is benchmarked against murine models, which increases the likelihood of unexplainable failures.[13,14]

Other challenges are at the tissue level. Chemotaxis around the B cell follicle border, for example, often occurs across ~100-micron distances. Problematically, most transwell-based chemotaxis assays work across greater distances. Fluid flow within the lymph node is also challenging to model, as the flow profile is non-uniform. Upon entering at the afferent lymphatics, fluid flow is constrained to the sinus and the transport inward toward the cortex is dependent on diffusion and flow. This creates unique shear profiles, of which entire models have been constructed toward recreating.[20] Lastly, the extracellular matrix used affects lymphocyte behavior on multiple levels including cell viability, state, and motility.[33–35] In general, effective tissue engineered models of the lymph node demand control and monitoring of cell phenotype as well as the ability to recreate the local signaling environment.

1.4 Advanced organ-on-chip designs can address the challenges of modeling human immunity

The field of tissue-engineering has devised numerous approaches to meet the need for modeling the multifaceted nature of tissue. Over the past decade, several design elements have emerged as being especially useful for modeling microscale tissue functions. I have comprehensively reviewed these design elements within the context of immunoengineering, both with the aim of supporting my own work as well as coauthoring a textbook chapter that is currently under revision (Fig. 1-2).

The ECM and flow profile in human tissue varies greatly and, as such, no single design element can be used to culture every tissue scenario. The most widely adopted and arguably simplest design approach is a **membrane-barrier chip**, in which two or more channels oriented parallel to one another are separated by a membrane **(Fig. 1-2a)**. This enables cells to be cultured separate and adjacent to other cell cultures, flowing media channels, or air-interfaces.

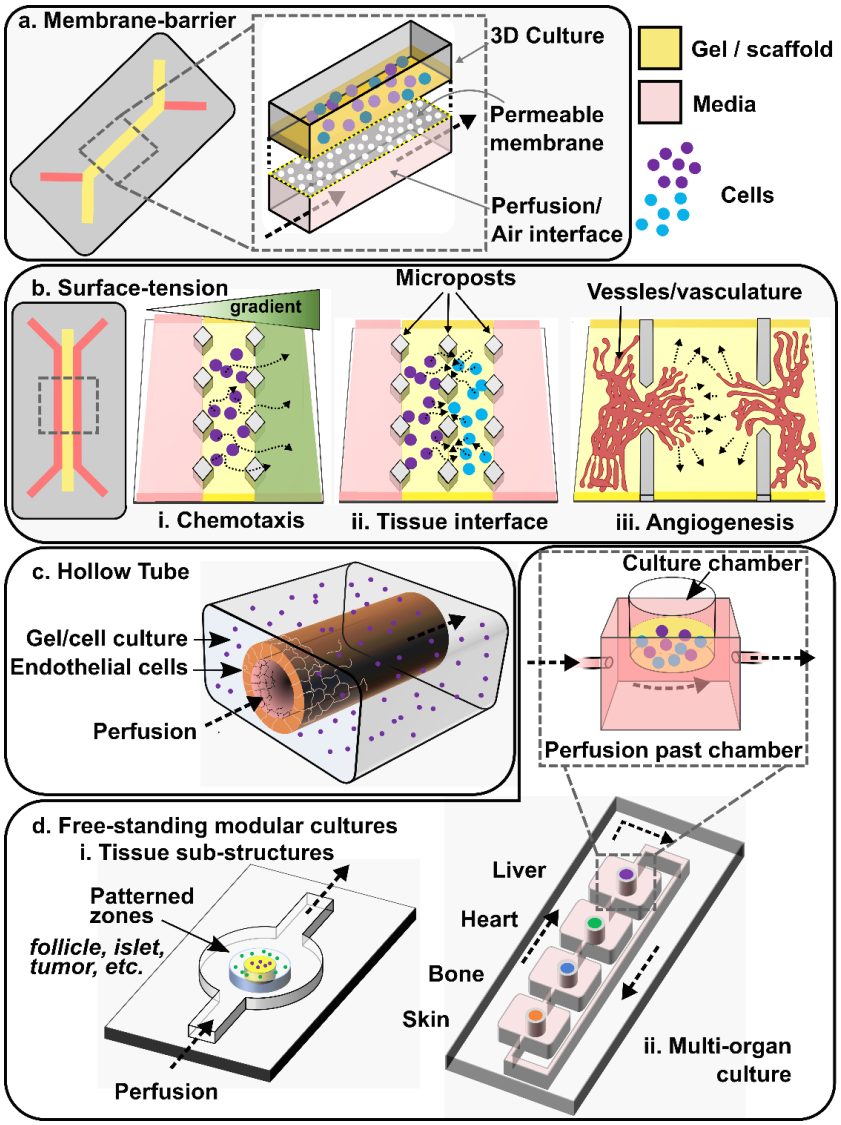

Figure 1-2 Reoccurring design elements within organ-on-chip systems. (a) Membrane-barrier chip for modular interfaces (media-media, media-air, media-hydrogel). (b) Surface-tension chips, having microposts for guiding fluids. (c) Hollow tube cultures for modeling tube-structures, most often vasculature. (d) Free-standing modular cultures, either for modeling multiple features within a single tissue, or for modeling multiple organs

This design element has been used to model a lung,[36] the intestinal lining,[37] the lymph node,[38] and numerous other models. In a similar approach, **surface-tension chips** feature parallel microfluidic lanes fabricated with partial walls or posts, which enables the use of surface tension to pattern distinct culture regions. For example, one or more cell-laden gels may be loaded into the channel(s), and cell migration and network growth is possible across the borders **(Fig. 1-2b)**.[39] This approach has been used to establish chemokine gradients, building tissue interfaces such as the blood-brain-barrier, or allowing angiogenic growth across gel lanes. In **hollow tube cultures,** endothelial cells are cultured in a tubular channel through which fluid is driven **(Fig. 1-2c)**.[40] The structure is most commonly produced using a sacrificial element, such as a rod that is embedded and later removed, or a sacrificial material that is patterned or 3D printed and later dissolved, after which endothelial cells are seeded to form a layer along the tube. This element is often used to mimic vascular or lymphatic lining, or the blood-brain barrier, and sometimes the surrounding tissue. Finally, in **free-standing modular**

cultures, multiple culture regions may be abutting or strung together. For example, nonlinear culture configurations may be enveloped in perfusing media **(Fig. 1-2di)** to enable the mechanistic study of the spatial organization of microscale tissue;[41] this approach is nascent and various fabrication strategies are being investigated. A **multiorgan chip** composed of connected modular cultures can be made by connecting multiple free-standing cultures with microfluidic channels **(Fig. 1-2dii)**, to provide powerful predictions of multiorgan interactions.[42–44]

Organ-on-chip models have been adapted to study immunity and in principle can be used to model primary immune tissues such as the lymph node, spleen, thymus, or bone marrow.[45] These immune-centric systems may enable mechanistic studies of how adaptive immune processes occur in tissue, as well as provide platforms to test vaccines and immunotherapies in the next decade. For example, one of the first lymph node organ-on-chips was introduced in 2010 termed, “Human artificial lymph node” (HuALN) and adopted the membrane-barrier design element, where culture chambers of mixed human B and T lymphocytes were cultured beside an oxygen-permeable membrane.[46] The recall formation of IgG in response to a common antigen (flu, tetanus) indicated success. Overall, however, little progress has been made toward mimicking adaptive immune responses (e.g. responses to novel vaccination or infection) or development of the immune system (e.g. B cell and T cell development in the bone marrow and thymus), despite repeated attempts.

In addition to modeling immune organs, models of other organs such as the gut, skin, lung, brain, vasculature, and even tumors have been modeled with immunity in mind. Typically, immune components are introduced into a pre-established model of the organ of interest. The simplest case includes addition of molecular cues such as cytokines (e.g. TNF to induce inflammation in a vascular model) or microbial signals (e.g. LPS). More complex models include the addition of one or more immune cells. To study tissue-resident immunity, innate immune cells such as macrophages or bone-marrow derived dendritic cells are a common starting point.

Integration of circulating lymphocytes such as neutrophils or monocytes is a further step up in complexity, often requiring the inclusion of an endothelial barrier as well as the tissue of interest. Finally, integration of adaptive immunity, e.g., by adding circulating T cells or B cells, is still in its infancy. Immune-competent organ-on-chip models offer promising insight into the mechanisms of autoimmune disorders and inflammation.

Advanced organ-on-chip designs have overcome some of the numerous obstacles for modeling human immunity, especially those related to tissue-level properties such as the ECM, chemotaxis, and modeling fluidics. Other obstacles, especially those related to cell-intrinsic properties such as the necessity for autology or the problem of low-precursor frequency, must be accounted for when designing the immune model.

A major unmet need that hinders growth in this exciting scientific space is an accurate, tissue-engineered model of the T and B cell-cell interactions that occur within the human lymph node. On a fundamental level, a tissue-engineered human lymph node model is needed to further our understanding of the immunity that leads to plasmablast formation, and ultimately the response to infection or vaccine. In parallel, this is needed at the translational and pharmaceutical level to advance drug and vaccine efficacy, as the high failure rate of immunomodulating agents is linked to a lack of appropriate models. The need is long overdue, as the skyrocketing cost of drugs, which takes root in clinical trial failure, jeopardizes healthcare at the patient and infrastructural level.

1.5 Meeting the need

My attempts to meet this need are described in this dissertation. **First,** the chapter, “Building a microphysiological model of the human lymph node B cell follicle border zone” describes the application of well-established tissue engineering methods toward modeling the lymph node. Having developed a successful model in chapter 2, **chapter 3** describes advancements made in collaboration with leaders in the microfluidics industry to construct the

lymph node model in alternative materials that are more suitable for manufacturing at large scale. The second half of the dissertation (chapters 4-5) describes fundamental advancements toward generating spatially-organized organ-on-chip models, with the broader goal of creating technology for mimicking the lymph node's spatial organization. This broad goal has been chased by numerous scientists in the Pompano Lab, so **Chapter 4** begins with a prelude that describes my specific focus on developing analytical techniques to characterize biomaterials that cure in the presence of light (photopolymerization). To that end, **Chapter 4** describes the development of colorimetric and nuclear magnetic resonance (NMR) techniques toward quantifying the extent of chemical modification of gelatin hydrogels. **Chapter 5** expands upon those concepts, with a focus on modifying the NMR technique described in chapter 4 to measure the extent of crosslinking. Returning to the initial goal of generating spatially complex tissue, the crosslinking density measurement was used to predict the stability of light-cured gels under physiological fluid flow. Following this, **Chapter 6** describes potential future directions of this work, divided between applications of the lymph node microphysiological system and applications of generating spatially complex organ-on-chip systems.

References

(1) Schlander, M.; Hernandez-Villafuerte, K.; Cheng, C.-Y.; Mestre-Ferrandiz, J.; Baumann, M. How Much Does It Cost to Research and Develop a New Drug? A Systematic Review and Assessment. *PharmacoEconomics* **2021**, *39* (11), 1243–1269. https://doi.org/10.1007/s40273-021-01065-y.

(2) Wouters, O. J.; McKee, M.; Luyten, J. Estimated Research and Development Investment Needed to Bring a New Medicine to Market, 2009-2018. *JAMA* **2020**, *323* (9), 844–853. https://doi.org/10.1001/jama.2020.1166.

(3) Ringel, M. S.; Scannell, J. W.; Baedeker, M.; Schulze, U. Breaking Eroom's Law. *Nat. Rev. Drug Discov.* **2020**, *19* (12), 833–834. https://doi.org/10.1038/d41573-020-00059-3.

(4) Association, A. H. Recent Trends in Hospital Drug Spending and Manufacturer Shortages. **2019**.

(5) Scannell, J. W.; Blanckley, A.; Boldon, H.; Warrington, B. Diagnosing the Decline in Pharmaceutical R&D Efficiency. *Nat. Rev. Drug Discov.* **2012**, *11* (3), 191–200. https://doi.org/10.1038/nrd3681.

(6) Cook, D.; Brown, D.; Alexander, R.; March, R.; Morgan, P.; Satterthwaite, G.; Pangalos, M. N. Lessons Learned from the Fate of AstraZeneca's Drug Pipeline: A Five-Dimensional Framework. *Nat. Rev. Drug Discov.* **2014**, *13* (6), 419–431. https://doi.org/10.1038/nrd4309.

(7) Fernando, K.; Menon, S.; Jansen, K.; Naik, P.; Nucci, G.; Roberts, J.; Wu, S. S.; Dolsten, M. Achieving End-to-End Success in the Clinic: Pfizer's Learnings on R&D Productivity. *Drug Discov. Today* **2022**, *27* (3), 697–704. https://doi.org/10.1016/j.drudis.2021.12.010.
(8) Wiedermann, U.; Garner-Spitzer, E.; Wagner, A. Primary Vaccine Failure to Routine Vaccines: Why and What to Do? *Hum. Vaccines Immunother.* **2016**, *12* (1), 239–243. https://doi.org/10.1080/21645515.2015.1093263.
(9) Flasche, S.; Wilder-Smith, A.; Hombach, J.; Smith, P. G. Estimating the Proportion of Vaccine-Induced Hospitalized Dengue Cases among Dengvaxia Vaccinees in the Philippines. *Wellcome Open Res.* **2019**, *4*, 165. https://doi.org/10.12688/wellcomeopenres.15507.1.
(10) Honda, K.; Ohba, Y.; Yanai, H.; Negishi, H.; Mizutani, T.; Takaoka, A.; Taya, C.; Taniguchi, T. Spatiotemporal Regulation of MyD88–IRF-7 Signalling for Robust Type-I Interferon Induction. *Nature* **2005**, *434* (7036), 1035–1040. https://doi.org/10.1038/nature03547.
(11) López-Yglesias, A. H.; Camanzo, E.; Martin, A. T.; Araujo, A. M.; Yarovinsky, F. TLR11-Independent Inflammasome Activation Is Critical for CD4+ T Cell-Derived IFN-γ Production and Host Resistance to Toxoplasma Gondii. *PLOS Pathog.* **2019**, *15* (6), e1007872. https://doi.org/10.1371/journal.ppat.1007872.
(12) Manzo, A.; Paoletti, S.; Carulli, M.; Blades, M. C.; Barone, F.; Yanni, G.; Fitzgerald, O.; Bresnihan, B.; Caporali, R.; Montecucco, C.; Uguccioni, M.; Pitzalis, C. Systematic Microanatomical Analysis of CXCL13 and CCL21 in Situ Production and Progressive Lymphoid Organization in Rheumatoid Synovitis. *Eur. J. Immunol.* **2005**, *35* (5), 1347–1359. https://doi.org/10.1002/eji.200425830.
(13) Carlsen, H. S.; Haraldsen, G.; Brandtzaeg, P.; Baekkevold, E. S. Disparate Lymphoid Chemokine Expression in Mice and Men: No Evidence of CCL21 Synthesis by Human High Endothelial Venules. *Blood* **2005**, *106* (2), 444–446. https://doi.org/10.1182/blood-2004-11-4353.
(14) Mestas, J.; Hughes, C. C. W. Of Mice and Not Men: Differences between Mouse and Human Immunology. *J. Immunol.* **2004**, *172* (5), 2731–2738. https://doi.org/10.4049/jimmunol.172.5.2731.
(15) Davis, M. M. A Prescription for Human Immunology. *Immunity* **2008**, *29* (6), 835. https://doi.org/10.1016/j.immuni.2008.12.003.
(16) Zushin, P.-J. H.; Mukherjee, S.; Wu, J. C. FDA Modernization Act 2.0: Transitioning beyond Animal Models with Human Cells, Organoids, and AI/ML-Based Approaches. *J. Clin. Invest. 133* (21), e175824. https://doi.org/10.1172/JCI175824.
(17) Lee, S. H.; Sung, J. H. Organ-on-a-Chip Technology for Reproducing Multiorgan Physiology. *Adv. Healthc. Mater.* **2018**, *7* (2), 1700419. https://doi.org/10.1002/adhm.201700419.
(18) Low, L. A.; Mummery, C.; Berridge, B. R.; Austin, C. P.; Tagle, D. A. Organs-on-Chips: Into the next Decade. *Nat. Rev. Drug Discov.* **2021**, *20* (5), 345–361. https://doi.org/10.1038/s41573-020-0079-3.
(19) Swartz, M. A.; Fleury, M. E. Interstitial Flow and Its Effects in Soft Tissues. *Annu. Rev. Biomed. Eng.* **2007**, *9* (1), 229–256. https://doi.org/10.1146/annurev.bioeng.9.060906.151850.
(20) Birmingham, K. G.; O'Melia, M. J.; Bordy, S.; Reyes Aguilar, D.; El-Reyas, B.; Lesinski, G.; Thomas, S. N. Lymph Node Subcapsular Sinus Microenvironment-On-A-Chip Modeling Shear Flow Relevant to Lymphatic Metastasis and Immune Cell Homing. *iScience* **2020**, *23* (11), 101751. https://doi.org/10.1016/j.isci.2020.101751.
(21) Huh, D.; Matthews, B. D.; Mammoto, A.; Montoya-Zavala, M.; Hsin, H. Y.; Ingber, D. E. Reconstituting Organ-Level Lung Functions on a Chip. *Science* **2010**, *328* (5986), 1662–1668. https://doi.org/10.1126/science.1188302.

(22) Satoh, T.; Sugiura, S.; Shin, K.; Onuki-Nagasaki, R.; Ishida, S.; Kikuchi, K.; Kakiki, M.; Kanamori, T. A Multi-Throughput Multi-Organ-on-a-Chip System on a Plate Formatted Pneumatic Pressure-Driven Medium Circulation Platform. *Lab. Chip* **2017**, *18* (1), 115–125. https://doi.org/10.1039/C7LC00952F.
(23) Wang, X.; Cirit, M.; Wishnok, J. S.; Griffith, L. G.; Tannenbaum, S. R. Analysis of an Integrated Human Multiorgan Microphysiological System for Combined Tolcapone Metabolism and Brain Metabolomics. *Anal. Chem.* **2019**, *91* (13), 8667–8675. https://doi.org/10.1021/acs.analchem.9b02224.
(24) Tan, K.; Keegan, P.; Rogers, M.; Lu, M.; R. Gosset, J.; Charest, J.; Sundhar Bale, S. A High-Throughput Microfluidic Microphysiological System (PREDICT-96) to Recapitulate Hepatocyte Function in Dynamic, Re-Circulating Flow Conditions. *Lab. Chip* **2019**, *19* (9), 1556–1566. https://doi.org/10.1039/C8LC01262H.
(25) Willard-Mack, C. L. Normal Structure, Function, and Histology of Lymph Nodes: *Toxicol. Pathol.* **2016**. https://doi.org/10.1080/01926230600867727.
(26) Buettner, M.; Bode, U. Lymph Node Dissection – Understanding the Immunological Function of Lymph Nodes. *Clin. Exp. Immunol.* **2012**, *169* (3), 205–212. https://doi.org/10.1111/j.1365-2249.2012.04602.x.
(27) Miyaji, K.; Furuse, A.; Nakajima, J.; Kohno, T.; Ohtsuka, T.; Yagyu, K.; Oka, T.; Omata, S. The Stiffness of Lymph Nodes Containing Lung Carcinoma Metastases. *Cancer* **1997**, *80* (10), 1920–1925. https://doi.org/10.1002/(SICI)1097-0142(19971115)80:10<1920::AID-CNCR8>3.0.CO;2-R.
(28) Travis, L. B.; Curtis, R. E.; Glimelius, B.; Holowaty, E.; Van Leeuwen, F. E.; Lynch, C. F.; Adami, J.; Gospodarowicz, M.; Wacholder, S.; Inskip, P. Second Cancers among Long-Term Survivors of Non-Hodgkin's Lymphoma. *J. Natl. Cancer Inst.* **1993**, *85* (23), 1932–1937.
(29) Pacheco, Y.; Acosta-Ampudia, Y.; Monsalve, D. M.; Chang, C.; Gershwin, M. E.; Anaya, J.-M. Bystander Activation and Autoimmunity. *J. Autoimmun.* **2019**, *103*, 102301. https://doi.org/10.1016/j.jaut.2019.06.012.
(30) *Follicular Helper CD4 T Cells (TFH) | Annual Reviews*. https://www.annualreviews.org/content/journals/10.1146/annurev-immunol-031210-101400 (accessed 2024-04-01).
(31) Bergler, W.; Adam, S.; Gross, H.-J.; Hörmann, K.; Schwartz-Albiez, R. Age-Dependent Altered Proportions in Subpopulations of Tonsillar Lymphocytes. *Clin. Exp. Immunol.* **1999**, *116* (1), 09–18. https://doi.org/10.1046/j.1365-2249.1999.00850.x.
(32) Qin, L.; Jing, X.; Qiu, Z.; Cao, W.; Jiao, Y.; Routy, J.-P.; Li, T. Aging of Immune System: Immune Signature from Peripheral Blood Lymphocyte Subsets in 1068 Healthy Adults. *Aging* **2016**, *8* (5), 848. https://doi.org/10.18632/aging.100894.
(33) Stachowiak, A. N.; Irvine, D. J. Inverse Opal Hydrogel-Collagen Composite Scaffolds as a Supportive Microenvironment for Immune Cell Migration. *J. Biomed. Mater. Res. A* **2008**, *85* (3), 815–828. https://doi.org/10.1002/jbm.a.31661.
(34) Pruitt, H. C.; Lewis, D.; Ciccaglione, M.; Connor, S.; Smith, Q.; Hickey, J. W.; Schneck, J. P.; Gerecht, S. Collagen Fiber Structure Guides 3D Motility of Cytotoxic T Lymphocytes. *Matrix Biol. J. Int. Soc. Matrix Biol.* **2019**. https://doi.org/10.1016/j.matbio.2019.02.003.
(35) Previtera, M. L. Mechanotransduction in the Immune System. *Cell. Mol. Bioeng.* **2014**, *7* (3), 473–481. https://doi.org/10.1007/s12195-014-0338-7.
(36) Huh, D. (Dan). A Human Breathing Lung-on-a-Chip. *Ann. Am. Thorac. Soc.* **2015**, *12* (Suppl 1), S42–S44. https://doi.org/10.1513/AnnalsATS.201410-442MG.
(37) Ashammakhi, N.; Nasiri, R.; Barros, N. R. de; Tebon, P.; Thakor, J.; Goudie, M.; Shamloo, A.; Martin, M. G.; Khademhosseini, A. Gut-on-a-Chip: Current Progress and Future Opportunities. *Biomaterials* **2020**, *255*, 120196. https://doi.org/10.1016/j.biomaterials.2020.120196.

(38) Goyal, G.; Prabhala, P.; Mahajan, G.; Bausk, B.; Gilboa, T.; Xie, L.; Zhai, Y.; Lazarovits, R.; Mansour, A.; Kim, M. S.; Patil, A.; Curran, D.; Long, J. M.; Sharma, S.; Junaid, A.; Cohen, L.; Ferrante, T. C.; Levy, O.; Prantil-Baun, R.; Walt, D. R.; Ingber, D. E. Ectopic Lymphoid Follicle Formation and Human Seasonal Influenza Vaccination Responses Recapitulated in an Organ-on-a-Chip. *Adv. Sci. Weinh. Baden-Wurtt. Ger.* **2022**, *9* (14), e2103241. https://doi.org/10.1002/advs.202103241.
(39) Huang, C. P.; Lu, J.; Seon, H.; Lee, A. P.; Flanagan, L. A.; Kim, H.-Y.; Putnam, A. J.; Jeon, N. L. Engineering Microscale Cellular Niches for Three-Dimensional Multicellular Co-Cultures. *Lab. Chip* **2009**, *9* (12), 1740–1748. https://doi.org/10.1039/B818401A.
(40) Gjorevski, N.; Avignon, B.; Gérard, R.; Cabon, L.; B. Roth, A.; Bscheider, M.; Moisan, A. Neutrophilic Infiltration in Organ-on-a-Chip Model of Tissue Inflammation. *Lab. Chip* **2020**, *20* (18), 3365–3374. https://doi.org/10.1039/D0LC00417K.
(41) Ortiz-Cárdenas, J. E.; Zatorski, J. M.; Arneja, A.; Montalbine, A. N.; Munson, J. M.; Luckey, C. J.; Pompano, R. R. Towards Spatially-Organized Organs-on-Chip: Photopatterning Cell-Laden Thiol-Ene and Methacryloyl Hydrogels in a Microfluidic Device. *Organs---Chip* **2022**, 100018. https://doi.org/10.1016/j.ooc.2022.100018.
(42) Edington, C. D.; Chen, W. L. K.; Geishecker, E.; Kassis, T.; Soenksen, L. R.; Bhushan, B. M.; Freake, D.; Kirschner, J.; Maass, C.; Tsamandouras, N.; Valdez, J.; Cook, C. D.; Parent, T.; Snyder, S.; Yu, J.; Suter, E.; Shockley, M.; Velazquez, J.; Velazquez, J. J.; Stockdale, L.; Papps, J. P.; Lee, I.; Vann, N.; Gamboa, M.; LaBarge, M. E.; Zhong, Z.; Wang, X.; Boyer, L. A.; Lauffenburger, D. A.; Carrier, R. L.; Communal, C.; Tannenbaum, S. R.; Stokes, C. L.; Hughes, D. J.; Rohatgi, G.; Trumper, D. L.; Cirit, M.; Griffith, L. G. Interconnected Microphysiological Systems for Quantitative Biology and Pharmacology Studies. *Sci. Rep.* **2018**, *8* (1), 4530. https://doi.org/10.1038/s41598-018-22749-0.
(43) Chramiec, A.; Teles, D.; Yeager, K.; Marturano-Kruik, A.; Pak, J.; Chen, T.; Hao, L.; Wang, M.; Lock, R.; Tavakol, D. N.; Lee, M. B.; Kim, J.; Ronaldson-Bouchard, K.; Vunjak-Novakovic, G. Integrated Human Organ-on-a-Chip Model for Predictive Studies of Anti-Tumor Drug Efficacy and Cardiac Safety. *Lab. Chip* **2020**, *20* (23), 4357–4372. https://doi.org/10.1039/D0LC00424C.
(44) Maschmeyer, I.; Lorenz, A. K.; Schimek, K.; Hasenberg, T.; Ramme, A. P.; Hübner, J.; Lindner, M.; Drewell, C.; Bauer, S.; Thomas, A.; Sambo, N. S.; Sonntag, F.; Lauster, R.; Marx, U. A Four-Organ-Chip for Interconnected Long-Term Co-Culture of Human Intestine, Liver, Skin and Kidney Equivalents. *Lab. Chip* **2015**, *15* (12), 2688–2699. https://doi.org/10.1039/C5LC00392J.
(45) Hammel, J. H.; Cook, S. R.; Belanger, M. C.; Munson, J. M.; Pompano, R. R. Modeling Immunity In Vitro: Slices, Chips, and Engineered Tissues. *Annu. Rev. Biomed. Eng.* **2021**. https://doi.org/10.1146/annurev-bioeng-082420-124920.
(46) Giese, C.; Marx, U. Human Immunity in Vitro - Solving Immunogenicity and More. *Adv. Drug Deliv. Rev.* **2014**, *69–70*, 103–122. https://doi.org/10.1016/j.addr.2013.12.011.

2 Building a microphysiological model of the human lymph node B cell follicle border zone

2.1 Abstract

There is a need for human-centric models of human immune processes that occur within the lymph node. Here, we configured a microphysiological system to facilitate monitoring and skewing of human T and B lymphocytes. We then combined T and B lymphocytes and established an artificial model of T cell help that enabled prediction of B cell maturation. Having engineered the system to enable live-cell motility imaging of 3D culture, we investigated the effect of synergistic T/B activation on cell motility in the presence of an artificial antigen. Finally, we utilized the model to test a clinically available immunosuppressant on bystander lymphocyte activation.

2.2 Introduction

Emergent models of human microphysiological systems (MPS) have ushered an era of unparalleled experimental control and predictive drug testing.[1,2] Composed of tissue-specific human cells in microfluidic housing, MPSs have been demonstrated to accurately model numerous human organs. A lymph node MPS (LN-MPS) is urgently needed for both fundamental and translational study, because our basic knowledge of immunology is derived from animal models, and immunomodulating agents remain the least-likely to pass clinical stages (0.1%).[3]

As the site of numerous essential immune processes, the homeostatic LN is responsible for the antibody response to infection, vaccines and cancer. In disarray, the LN is central to autoimmunity and cancer metastasis. Underlying these processes are numerous, highly-regulated and spatially organized cell-cell interactions that occur at

the edge of a B cell follicle.[4] One such interaction that is key to the infection and vaccine response is T cell help for B cell activation.[5]

Several LN-MPS models have made advancements by demonstrating recall responses to common antigens such as the flu vaccine in the presence of mixed immune cells.[6–8] While a recall response is a useful benchmark for validating B cell activity, the response alone does not provide insight to the mechanism of cell-signaling or drug activity. Instead, an effective LN-MPS requires mechanistic control over the transient cellular states, from naïve T and B lymphocytes to t follicular helper and plasmablast formation.

Other models have enabled mechanistic study of fundamental LN tissue processes, such as the effect of chemokines, shear stress, or hydrogel chemistry on immune cell activity.[9–16] While these models do provide insight into underlying immune cell behavior, their use has not been extended toward modeling translationally relevant lymph node immune processes such as T cell help. Therefore, a lymph node MPS (LN-MPS) having the capability to manipulate and monitor sensitive transient cell states as well as the cell-cell interactions is needed.

Herein, we developed a LN-MPS capable of simultaneously modeling fundamental such as chemotaxis, and then extended the utility of the model for predicting T cell dependent plasmablast formation. We validated both T and B cell activation within the chamber, while simultaneously monitoring chemotaxis and secreted factors in response to stimuli. To mimic T cell help, we first skewed T cells from the naïve to follicular-helper state, and then cocultured with B cells to initiate synergistic

activation. Using a superantigen to crosslink the T- and B-cell receptors, we tuned T cell help within the LN-MPS and characterized changes in motility and cluster formation. Finally, to further modulate T/B crosstalk and predict immunosuppressant efficacy, we added a clinically available JAK inhibitor to disrupt T/B engagement. The advancements described within this LN-MPS are key to both advancing our human experimental toolkit.

2.3 Results

2.3.1 The LN-MPS design was effective at mimicking lymphoid tissue spatial organization.

To benchmark the LN-MPS design against human tissue, we first performed immunofluorescence staining to label human T and B cells on a human lymphoid tonsil slice (Fig 1a.). We chose this approach for benchmarking, as LN slices are well-established as an acute model of adaptive immunity.[17] As expected, the tissue was highly spatially organized, and T and B lymphocytes are generally isolated from one another. It is well-established that the B cell follicle border zone, where T and B lymphocytes mix, are the site of T cell help for plasmablast formation (Fig. 1b).

Considering this, we designed the LN-MPS using a well-established[18] microfluidic chip design having parallel arrays of posts that enabled surface-tension filling (Fig. 1c). As an initial test of the posts' ability to maintain separate, fluidically-connected lanes, we resuspended naïve T and B lymphocytes in separate collagen-based hydrogels and injected them into the outer lanes (Figure 1cii). After allowing the gel to thermally set at 37 C for 30 minutes, we filled the central lane with non-cell-laden gel and cultured for 1

hour. From this we concluded that the cells were effectively patterned with spatial control over their initial positions.

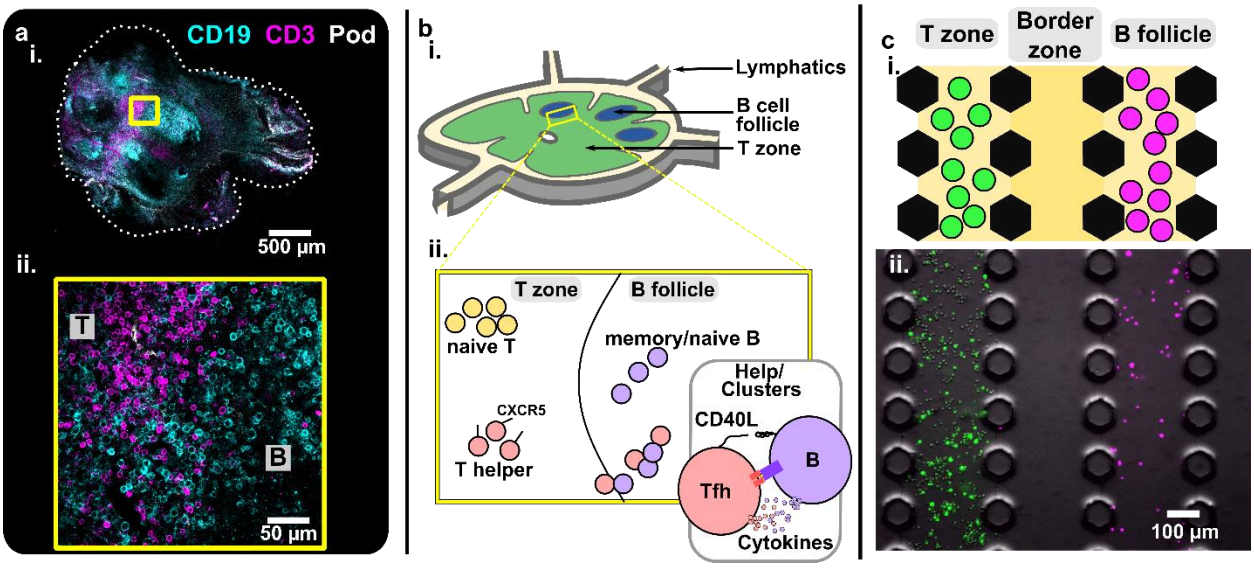

Figure 2-1 Modeling approach for the human TB-MPS. (a) (i) Image of a human tonsil slice with (ii) zoom on a T/B border zone. (b) (i) illustration and (ii) signaling diagram of t/b border processes. (c) (i) Schematic and (ii) image of the T/B border chip, where microposts enable surface-tension barriers between cell-laden hydrogels.

2.3.2 The LN-MPS was biocompatible for naïve T cells, enabled effector T cell formation and control over cell migration.

After validating the spatial control of the LN-MPS, we proceeded to study T cell behavior within the chip. First, to assess the biocompatibility of the LN-MPS, we cultured highly sensitive primary, naïve CD4+T cells on chip for five days. Using a fluorescent Live/Dead stain, we observed a minor loss in viability (< 20%) from 2D plated controls (Fig. 2a). This decrease was acceptable considering the high-sensitivity of primary human lymphocytes, as well as the ability for dead cells to become trapped in 3D cultures.

Next, to assess the responsiveness of naïve CD4+T cells within the chamber, we mimicked dendritic cell priming by injecting a polymeric α-CD3/CD28 (STEMCELL) solution into the media lane (Fig. 2b). Within 48 hours, CD69 was upregulated and imaged with immunofluorescence staining. In addition, IFN-γ was detectable within the media lanes after 24 hours, and increased daily for five days. From this, we concluded that naïve T cells were responsive to activation stimuli on chip.

Then, to assessed if naïve CD4+ T cells were capable of responding to chemokine gradients on chip, we added CCL21 to the left media lane and assessed cell migration. Within an hour, cells in chips that contained CCL21 migrated toward out of their initial lane and toward the gradient. In addition, mean cell velocity was significantly higher when measured just 30 minutes following the addition of CCL21. We concluded then, that we could both control and monitor lymphocyte motility in the LN-MPS.

These results collectively demonstrate that this LN-MPS enables culture, stimulation, and monitoring of primary T cells. While anti-CD3/CD28 stimulation for activating CD4 T cells is well established, the biomaterials innovations surrounding T cell modulation is a rapidly developing field of study.[19–21] As such, the need for human-relevant models for assessing the efficacy of novel T cell stimulants is clear, and the LN MPS was demonstrated here to meet that need.

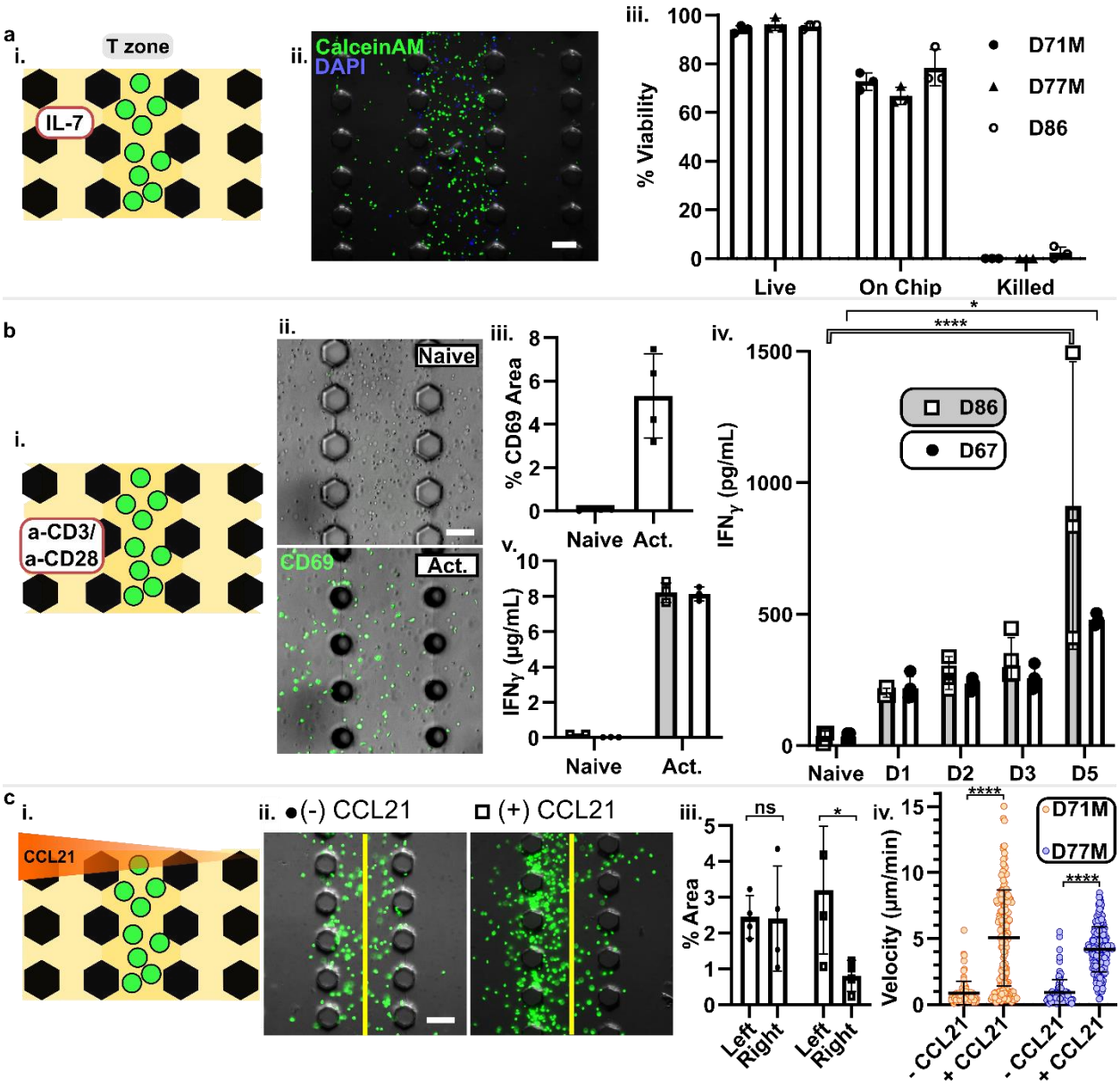

Figure 2-2 Naïve, CD4+ T cells were viable, responded to stimuli, and responded to chemokine CCL21 on chip. (a) (i) Naïve T cells were cultured with IL-7 on chip to maintain viability for four days. (ii) Images and (ii) quantification of T cell viability (Calcein/Live/green, Dapi/Dead/blue). (b) (i) Naïve T cells were activated on chip with a-CD3/CD28 (StemCelll). (ii) Images and (iii) quantification of activated T cells on chip staining CD69+ (green) after 48 hours (Unpaired T test, **:p<0.005). (iv) IFN-γ secretion by CD4+T cells activated quantified with ELISA, compared to naïve cells on chip and (v) plated controls (d) (i) A CCL21 gradient was established on chip. (ii) Images and (iii) quantification of naive CD4+ T cells after migrating toward CCL21 (left) for 1 hr and staining with CalceinAM (green). (iii) quantification of cell velocity 30 min after gradient set up. All scale bars: 100 µm. (b iv, c analyzed with ordinary two-way ANOVA with Sidak's multiple comparisons test w/single pooled variance, ns: p>0.05, *:p,0.05, ****:p<0.00005).

2.3.3 Naïve B cells responded to activation stimuli on chip.

Having established the conditions for T cells on the LN chip, we sought to determine if B cells could be manipulated in a similar manner. To determine if B cells would respond to activation stimuli, we added a cocktail of CD40L, R848, and α-IgG/IgM. We first examined the effect of the activation cocktail on B cell viability, and saw that both naïve and activated B cells remained viable after 48 hours (Fig. 3a). Indicative of activation, we saw B cells cultured with the cocktail were more blast-like and took up more CalceinAM stain (Fig. 3a ii-v). To further characterize the B cell state, we immunostained the cells for CD69 and CXCR5. As expected, B cells cultured with the cocktail exhibited increased expression of both markers (Fig. 3b ii-v).

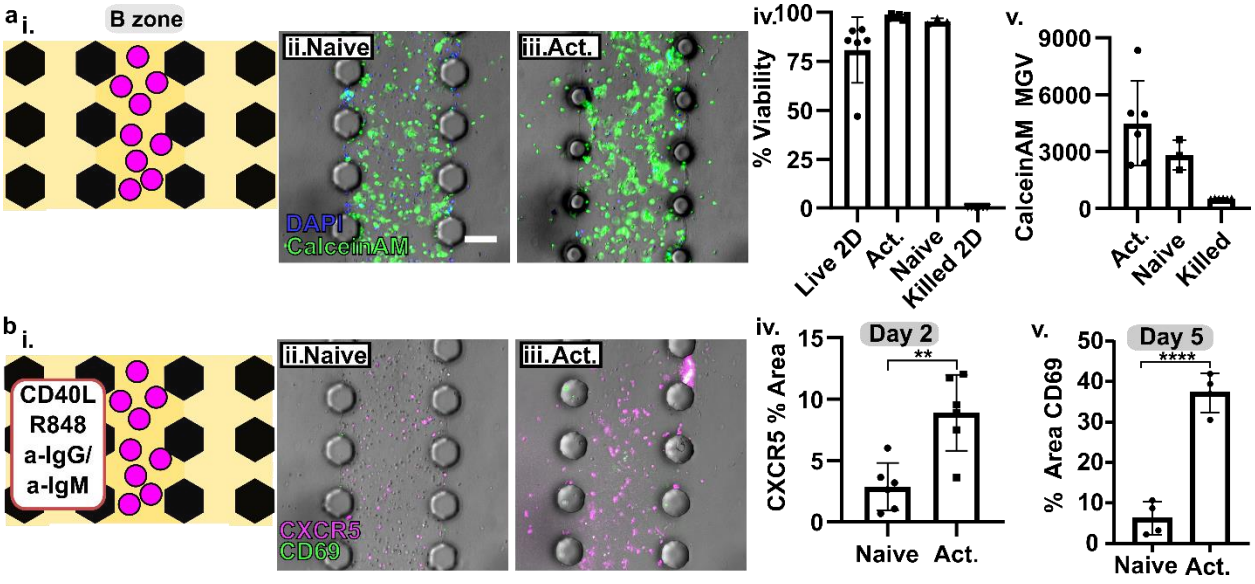

Figure 2-3. B cell receptor, toll-like-receptor, and CD40L stimulation enables effector B cell formation on chip. (a) i. Schematic for B cell culture on chip. Composite (fluorescence overlayed over brightfield) microscope images of (i) activated and (ii) naïve B cells on chip with viability stain (Calcein/Live/green, Dapi/Dead/blue) after 48 hour culture. Scale bar: 100 µm. (iii) Quantification of % viability. (iv) Quantification of calceinAM brightness. (b) I. Schematic for activating naïve B cells on chip. Images of (ii) activated and (iii) naïve B cells on chip with stained with anti-CXCR5 (magenta) and anti-CD69 (green). Quantification of (iv) CXCR5+ area and (v) CD69+ area after varying culture times (unpaired T test, **:p<0.005, ****:p<0.00005.).

2.3.3 Naïve T cells were skewed to T follicular helper cells on chip when cultured with IL12 and activin A.

Having established culture conditions for maintaining T and B lymphocytes in their naïve and activated states, we next sought to model the early stages of T cell help by generating T follicular helper (Tfh) cells on chip. Before a T cell provides help for B cell activation, it first becomes primed by antigen specific dendritic cells via α-CD3/CD28 stimulation, as well as secretion of a variety of cytokines. Numerous cytokines have been shown to be involved in Tfh skewing, and several inconsistencies have been identified between mouse and humans. Its been demonstrated that cytokines IL12 and activin A are capable of driving naïve T cells to TFHs in a dish. Upon engagement with skewing cytokines, T cells are known to upregulate CXCR5, BCL6, and PD-1.

As we sought to mimic this process on chip, we loaded the LN MPS with naïve T cells, and then added α-CD3/CD28, IL12, and activin-A to the media lanes. After five days culture, we observed small, CXCR5+ clusters form on chip in the presence of the skewing cocktail, compared to no clusters in the plain media. To further characterize the T cell state, we recovered the cells from the chip and analyzed the cells via flow cytometry. We did this by adding a solution of collagenase D to the media lanes for fifteen minutes, massaging the elastic PDMS housing, and then rinsing across the media lanes with an ice-cold solution of dilute FBS. In order to recover enough cells for a confident analysis, we pooled cells from twenty chips, and then repeated this analysis across three human donors.

The resulting flow plots showed a significant increase in CXCR5, PD-1, and BCL6, indicating successful Tfh skewing from naïve T cells on chip across multiple human donors.

The utility of PD-1 expression on TFHs is apparent in the context of T cell dependent B cell activation, were PD-1 is a key regulator.[22] As such, it was essential to validate the presence of these markers prior to using the LN-MPS for predicting plasmablast formation.

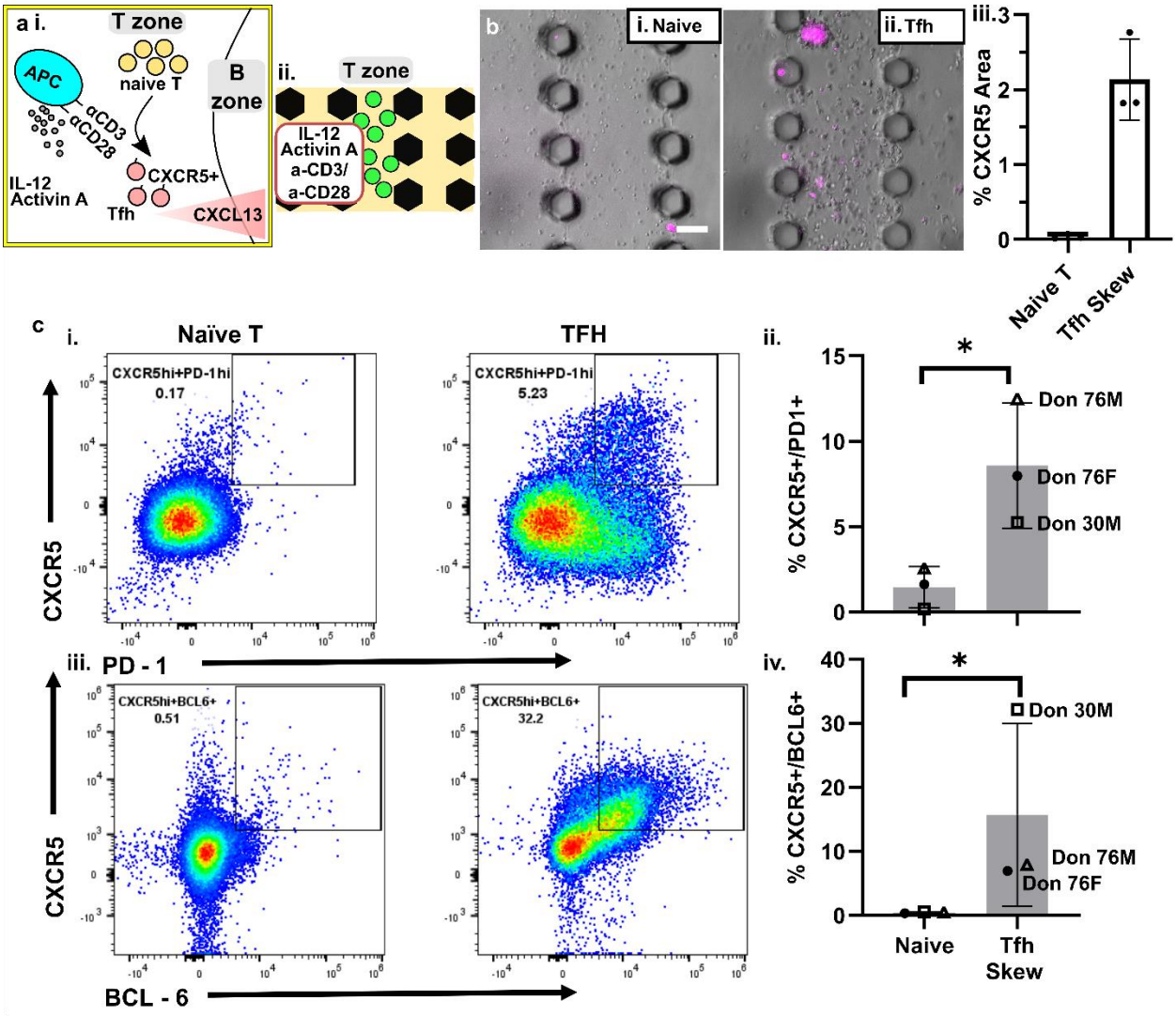

Figure 2-4 IL-12 and Activin A were sufficient for skewing naïve CD4 T cells to TFHs on chip. a. i. Schematic of Tfh skewing at the T/B border zone. ii. Schematic of culture conditions

on chip. b. Image overlays of fluorescence (AF647-antiCXCR5, magenta) and brightfield for (i) naïve and (ii) Tfh skewed CD4 T cells after 3 days culture. (iii) Quantification. Scale bar: 100 µm. c. Flow cytometry characterization of TFH markers from cells recovered from chips. (Pooled 20 chips/donor). (i) 2D plots of CXCR5 vs PD-1. (ii) Quantified results from three donors. (iii) 2D plots of CXCR5 vs BCL-6. (iv) Quantification from three donors. One tailed t-test. $P<0.05$.

2.3.5 Tfh skewed cells provided help to B cell activation in 2D culture and on chip.

A central checkpoint during the infection/vaccine response is T cell help, as the production of plasmablasts is dependent on antigen-mediated TCR/BCR engagement. Having successfully skewed Tfhs and effector B cells in the LN MPS, we next sought to combine the two cells to create a model of this decisive step. One well-established tool for bypassing antigen-specificity is the superantigen Staphylococcus enterotoxin B (SEB), which crosslinks the TCR and BCR.[23,24] To confirm the ability for SEB to trigger plasmablast formation, we added SEB to a T/B coculture in a round-bottom well for seven days, and phenotyped the cells via flow cytometry. We observed the formation of plastmablasts (CD38hi, CD20lo) and detected increased IgG concentration in the media when SEB was present, verifying the anticipated effect of SEB (Fig. 5).

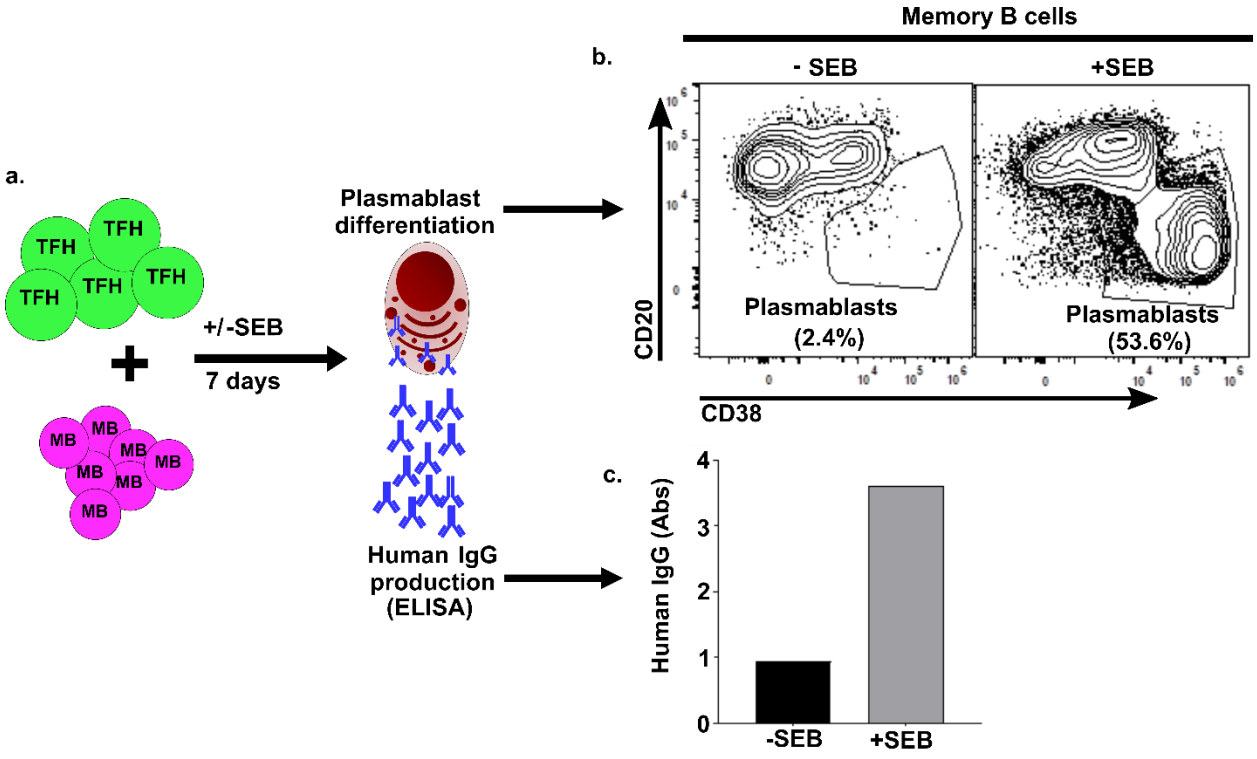

Figure 2-5. SEB mediated plasmablast formation in a round-bottom dish. (a) Schematic for experiment. (b) 2D flow plots (CD20 vs CD38), gated on B cells, of cells after 7 days culture. (c). Quantification of IgG secretion via ELISA

Next, we configured the LN MPS to be a tractable model of T cell help. We did this by first activating naïve B cells and skewing naïve T to TFHs in 2D culture for four days, and then cultured on chip with or without SEB for five days (Fig. 6a). While TCR/BCR engagement is critical to T cell help, another influential process is bystander activation, where local effector T and B lymphocytes influence T/B interactions through antigen-independent interactions.[25,26] To test the effect of bystander effect on T cell help, we compared the effect of pre-activating T and B lymphocytes mixed versus in separate culture wells.

Regardless of the lymphocytes being mixed or separated during the initial activation steps, SEB enabled the formation of CD38+ clusters on chip (Fig. 6b,c). As evidence of synergistic bystander activation, we did occasionally see non-SEB-

mediated CD38 signal when cells were pre-mixed (Fig 6e, Donor 33F). In conclusion, the LN MPS enabled the prediction of bystander effect on CD38+ B cell formation when configured as a model of T cell help.

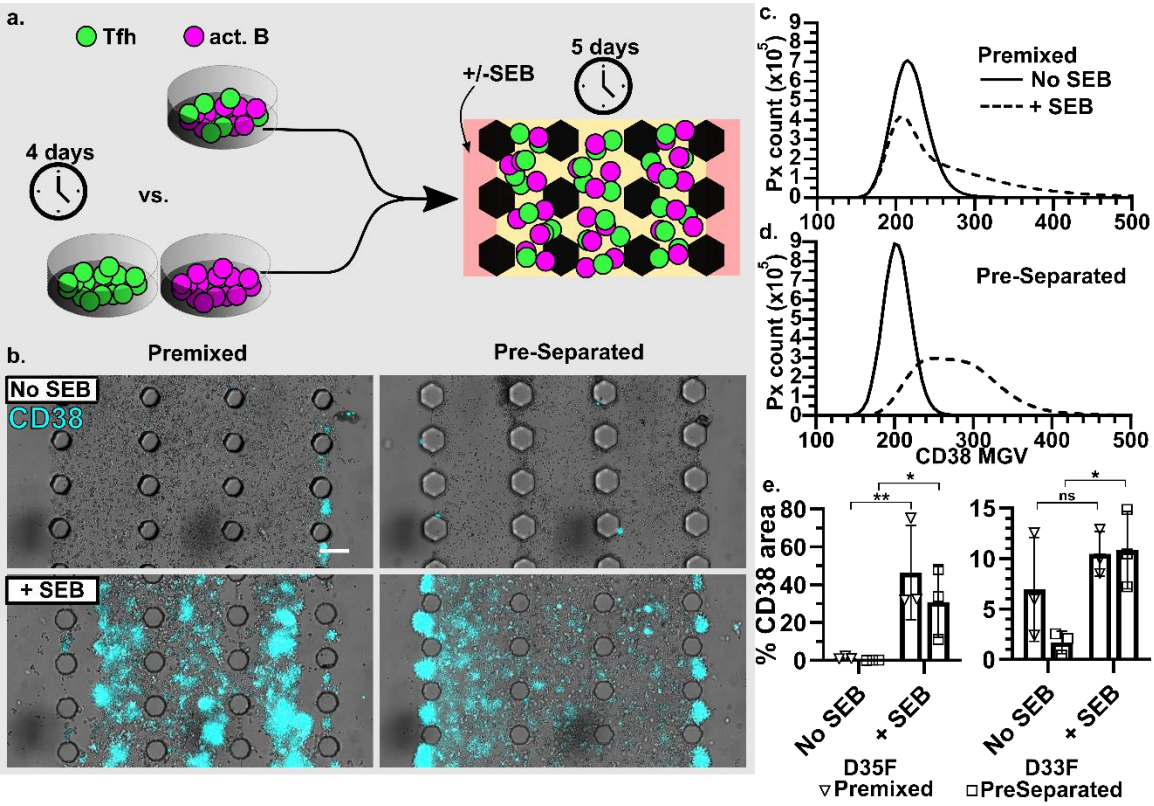

Figure 2-6 Skewed Tfh cells provided help for SEB-mediated B cell activation on chip. (a) schematic of experiment. (b) Fluorescence (CD38, cyan) brightfield overlay images of Tfh/actB cocultures in each condition. Scale bar: 100 µm. (c) Histograms of CD38 signal from premixed Tfh/actB cocultures. (d) Histograms of CD38 signal from pre-seperated Tfh/actB cocultures. (e) Quantification of CD38+ area from two donors. (* $p<0.05$, ** $p<0.005$, Ordinary two-way ANOVA. Multiple comparisons with uncorrected Fishers LSD, with a single pooled variance.)

2.3.6 SEB-mediated T cell help on chip resulted in high-velocity lymphocyte clusters.

Having confirmed SEB-mediated T-cell-help and CD38+ B cell formation, we next investigated how T-cell-help affected lymphocyte clustering and motility. As T cell help is primarily dependent on long-term (>24 hour) TCR/BCR engagement, we

hypothesized that CD38+ B cells would be surrounded by clusters of lymphocytes, and that cell motility would be localized CD38+ areas (Fig 7a). Of the conditions tested premixed, non-SEB condition and pre-separated, +SEB conditions exhibited an appropriate minimal cell-motility and mean CD38 signal to test this hypothesis. In contrast, we observed too few moving cells in the pre-separated, non-SEB negative control, and too high CD38 signal in the Premixed, +SEB positive control to test assess our hypothesis. Confirming our hypothesis, we saw random lymphocyte motility in the non-SEB condition, and clusters of motile cells surrounding CD38+ regions in the +SEB conditions (Fig. 7b).

Extending this observation further, we hypothesized that T-cell-help conditions would exhibit higher mean cell velocity due to the high-number of CD38+ clusters seen in +SEB conditions, and this was certainly the case (Fig. 7c). In both +SEB conditions, the mean cell velocity was significantly higher than the non-SEB conditions. Also, the premixed T/B coculture exhibited significantly higher velocity than the pre-separated. This data, combined with the overall increase in CD38 signal shown in Fig. 6, confirmed that synergistic bystander T/B activation prior TCR/BCR engagement enhanced T/B interactions.

A current gap in knowledge is the relationship between bytstander activation, lymphocyte state, and cell motility in the lymph node, and the few attempts to investigate this have generally relied upon intravital imaging of the LN T/B border zone.[27] Our results suggest, that antigen-independent cell-cell interactions prior to an artificial antigen (SEB) enhanced motility. While these results are not sufficient for

exhaustively characterizing the relationship between motility and bystander effects, they do reflect the utility of the LN-MPS for enabling new discovery in this area.

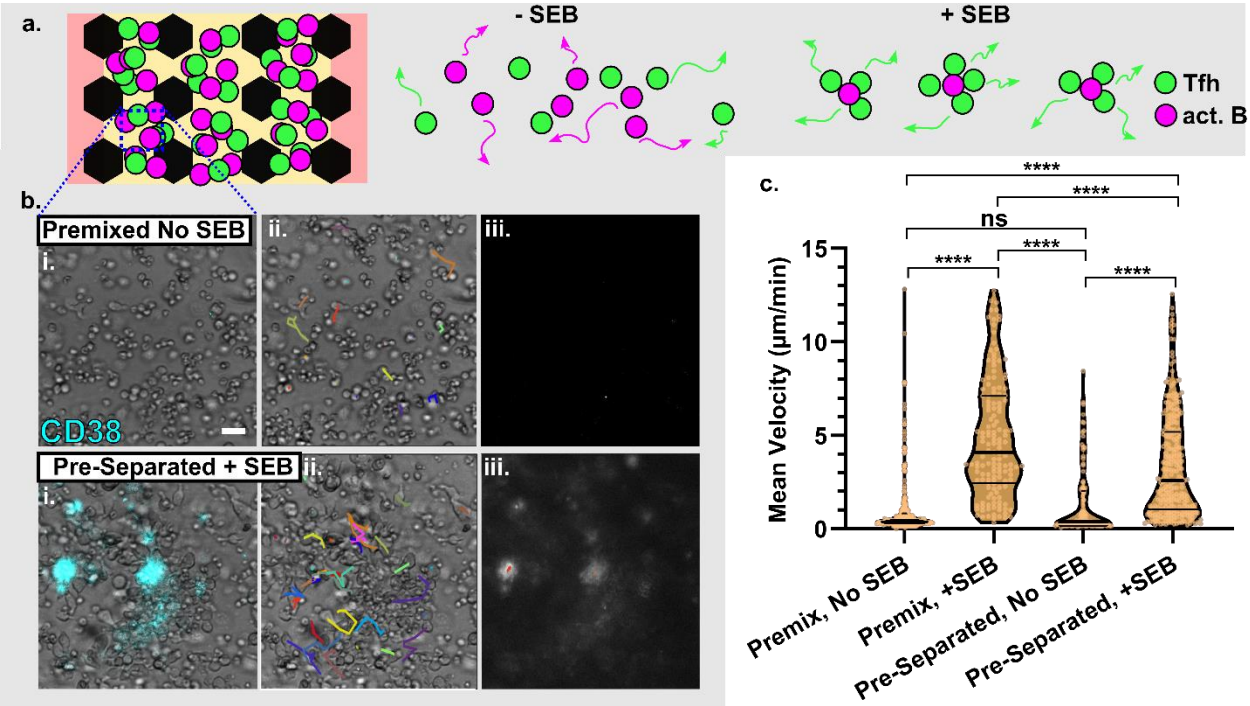

Figure 2-7 Cell motility was enhanced by SEB and synergistic T/B pre-activation. (a) Schematic of SEB mediated cluster formation. (b) Images of T/B cocultures on chip. (i) Composite fluorescence (CD38, cyan) brightfield overlay, (ii) brightfield and cell motility tracks (multicolor lines) overlay, (iii) CD38 and cell motility tracks overlay. Scale bar: 20 μm. (c) Truncated violin plots illustrating mean cell velocity of cells in various culture conditions. Ordinary one-way ANOVA with turkey's multiple comparisons, with a single pooled variance. (****=$p<0.00005$, ns=$p>0.05$).

2.3.7 Synergistic T/B interactions were suppressed via JAK inhibition

Having observed that a pre-activation coculture of T and B lymphocytes enhanced the subsequent T-cell-help, we next modulated the underlying signaling that supported the interactions. As it is known that T-cell-help occurs by both TCR/BCR engagement and supportive cytokine signaling[5], we hypothesized that synergistic T/B bystander activation could be suppressed via JAK-inhibition.

To enable bystander T/B interactions on chip, we premixed and cultured naïve T and B cells having Tfh skewing and B cell activation signals. After a four-day preculture, the coculture was injected onto the LN MPS, and then cultured for an additional 7 days. This was compared to a coculture having only the B cell activation ingredients (Fig. 8a). As expected, the Tfh/actB coculture on chip resulted in both increased CD69 and CD38 signal compared to the naïveT/actB coculture (Fig. 8b,c). To test the effect of JAK-inhibition on the Tfh/actB coculture, we added the clinically available immunosuppressant, Tofacitinib, to the chip media lanes.[28] Confirming our hypothesis, we observed decreased CD38 signal in the tofacitinib-treated condition. (Fig. 8b,d).

While tofacitinib has been heralded as a the first JAK-inhibitor for the treatment of autoimmune disorders such as rheumatoid arthritis and inflammatory bowel disease, its effect on immune cell-cell interactions is still being investigated.[29] In addition to using Tofacitinib as an effective cytokine blocker for this experimental design, we simultaneously demonstrated the utility of the LN MPS as an instrument for observing drug-efficacy on lymphocyte cell-cell interactions.

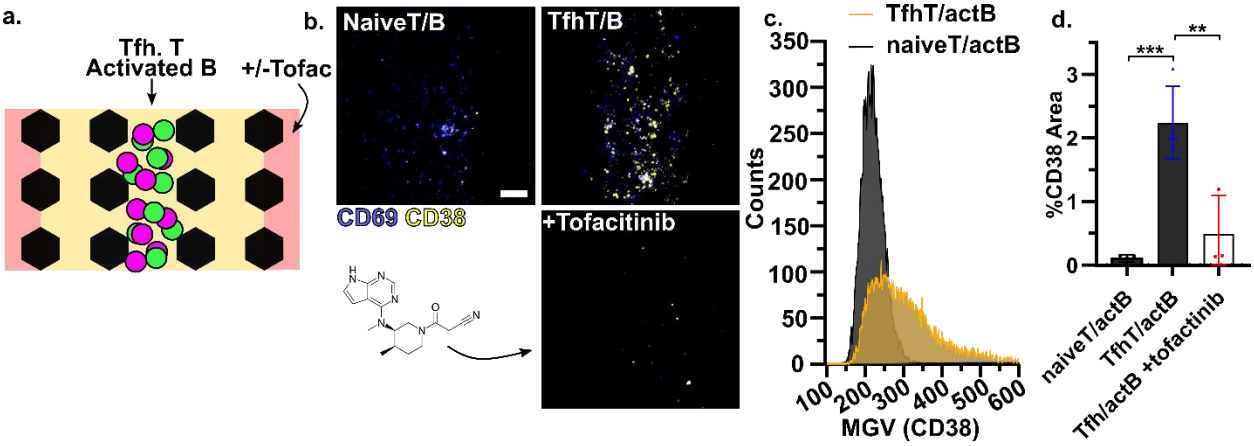

Figure 2-8 Tofactinib as a modulator of bystander T/B interactions. (a) Schematic for modulating T/B interactions on chip. (b) Fluorescence overlay images (FITC-CD69 and AF546-

CD38) of T/B cocultures in various conditions. Scale bar: 100 µm. (c) Histogram of CD38 signal from images. (d) % CD38 area quantified from each condition. Ordinary one-way ANOVA, with turkey's multiple comparisons test with single pooled variance. (**=p<0.005, ***=p<0.0005).

2.4 Conclusion

We successfully used the LN MPS to enact spatial control over lymphocyte motility via chemotactic cues. Then, we modeled naïve-to-effector-T and B cell differentiation in isolation. Using the LN MPS as a lens into *in vivo* like motility and clustering, we modulated T and B coculture to predict B cell maturation. Finally, we modeled a drug test and inhibited T/B crosstalk through the use of a clinically available immunosuppressant, tofacitinib.

2.5 Method

The methods described here are abbreviated for clarity, as this manuscript is currently in progress.

Cell sourcing and culture media (activation, skewing)

Naïve, human CD4+ T cells and naïve B cells were purified from TRIMA collars, a derivative product of platelet apheresis. Donors were healthy and deidentified, although age and gender information was retained (STEM CELL, Crimson Core, Brigham and Women's Hospital, Boston, MA and INOVA Laboratories, Sterling, VA). Cells were cultured in AIM V media with streptomycin sulfate and gentamicin (Gibco, P/N 12055083). In 2D culture, T and B lymphocytes were cultured at 1-3 x 10^6 cells/mL. For maintaining viable naïve CD4+ T cells, IL-7 was added at a concentration of 4 ng/mL. To activate naïve CD4+ T cells in 2D and 3D culture, ImmunoCult™ Human CD3/CD28 T Cell Activator (StemCell Technologies) was added to the media at the recommended concentration. For Tfh skewing, naïve, CD4+T cells were activated with

ImmunoCult™ and cultured with IL-12 (5 ng/mL) and activin A (100 ng/mL). To activate B cells in monoculture, a cocktail of human α IgG/IgM (10 µg/mL), R848 (500 ug/mL), and CD40 ligand (100 ug/mL) was added to the culture media. When B cells were activated in coculture with T cells, CD40 ligand was not added to the cocktail. Staphylococcus enterotoxin B (SEB) was added at a concentration of 0.25 ng/mL. Tofacitinib was used at a dose 0.1 uM.

Tonsil lymphoid tissue sourcing

Tonsils were provided by the UVa hospital and then processed, sliced, and immunostained by Parris Anabaei

Hydrogel

Collagen/fibrinogen hydrogel was prepared by diluting 5 mg/mL rat tail I collagen (Ibidi) and 2 mg/mL fibrinogen (Sigma Aldrich) to a final concentration of 1.5 mg/mL collagen and 1 mg/mL fibrinogen. Experiments shown involving T or B lymphocytes in isolation on chip, cells were resuspended in hydrogel at $10x10^6$ cells/mL. Experiments shown with T/B cocultures, cells were resuspended in hydrogel at $25x10^6$ cells/mL per cell type, (total cell density $50x10^6$ cells/mL).

Microfluidic chip

The LN MPS described here is a microfluidic chip with comprised of five parallel channels separated by arrays of hexagonal micropillars (100 µm in diameter, with 50 µm spacing between pillars). The outer channels each had 8-mm diameter inlets and outlets that served as media reservoirs, while the inner gel channels had 0.75-mm inlets and outlets. The inlet/outlet diameters of the outer media channels and inner gel

channels were 8 and 0.75 mm respectively. Excluding the converging, angled channel regions, the media lanes were 2.05 x 0.13 x 3.5 mm3 and the gel lanes were 0.3 x 0.13 x3.5 mm3.

Viability staining

Viability staining was performed by adding a solution of CalceinAM/DAPI (10 uM/1 uM) in PBS to the media resvoirs, and then incubating the chip for 1 hr. The media resvoirs were then rinsed with excess (500 uL) PBS once every thirty minutes for 1 hr, and them imaged.

Chemotaxis

For assessing chemotactic activity of naïve CD4+ T cells on chip, a solution of CCL21 in AIMV media (0.1 uM) was added to the left media reservoir and then incubated for 30 min for assessing live-cell motility or 1 hr for assessing total cell displacement. Cells were imaged with no labeling for live-cell imaging, and cells were labeled with 10 uM CalceinAM prior to imaging for total cell displacement.

Cell Motility imaging

To perform live-cell motility imaging, chips were imaged on a stage-top incubator set to 37 C at 30 sec intervals for 5 min. For calculating mean cell velocity, individual cells were tracked using CellTracker with semi-automated tracking.

Immunofluorescence microscopy staining

For immunofluorescence staining on chip, the media in the chips resvoirs was replaced with the appropriate antibody cocktail prepared in HBSS (gibco). Chips were stained for 1.5 hours, while incubated at 37 C, and then the media resvoirs were rinsed with AIM V media every 20 minutes for one hour.

Antibody	Fluorophore	Vender/PN/Lot	dilution in HBSS
CD69	FITC	BioLegend/310904/B372054	100
CXCR5	AF647	BD Pharmingen/558113/	100
CD38	AF546	Santa Cruz Biotechnology /sc-7325 AF546/A0924	100

Cytokine and antibody secretion Detection

IFN- γ and antibody secretions were quantified with ELISA kits (Biolegend).

2.6 References

(1) Low, L. A.; Mummery, C.; Berridge, B. R.; Austin, C. P.; Tagle, D. A. Organs-on-Chips: Into the next Decade. Nat. Rev. Drug Discov. 2021, 20 (5), 345–361. https://doi.org/10.1038/s41573-020-0079-3.

(2) Zushin, P.-J. H.; Mukherjee, S.; Wu, J. C. FDA Modernization Act 2.0: Transitioning beyond Animal Models with Human Cells, Organoids, and AI/ML-Based Approaches. J. Clin. Invest. 133 (21), e175824. https://doi.org/10.1172/JCI175824.

(3) Ringel, M. S.; Scannell, J. W.; Baedeker, M.; Schulze, U. Breaking Eroom's Law. Nat. Rev. Drug Discov. 2020, 19 (12), 833–834. https://doi.org/10.1038/d41573-020-00059-3.

(4) Willard-Mack, C. L. Normal Structure, Function, and Histology of Lymph Nodes: Toxicol. Pathol. 2016. https://doi.org/10.1080/01926230600867727.

(5) Follicular Helper CD4 T Cells (TFH) | Annual Reviews. https://www.annualreviews.org/content/journals/10.1146/annurev-immunol-031210-101400 (accessed 2024-04-01).

(6) Goyal, G.; Prabhala, P.; Mahajan, G.; Bausk, B.; Gilboa, T.; Xie, L.; Zhai, Y.; Lazarovits, R.; Mansour, A.; Kim, M. S.; Patil, A.; Curran, D.; Long, J. M.; Sharma, S.; Junaid, A.; Cohen, L.; Ferrante, T. C.; Levy, O.; Prantil-Baun, R.; Walt, D. R.; Ingber, D. E. Ectopic Lymphoid Follicle Formation and Human Seasonal Influenza Vaccination Responses Recapitulated in an Organ-on-a-Chip. Adv. Sci. Weinh. Baden-Wurtt. Ger. 2022, 9 (14), e2103241. https://doi.org/10.1002/advs.202103241.

(7) Lubitz, A.; Giese, C. Human Artificial Lymph Node Model (HuALN). In Encyclopedia of Immunotoxicology; Vohr, H.-W., Ed.; Springer Berlin Heidelberg: Berlin, Heidelberg, 2014; pp 1–6. https://doi.org/10.1007/978-3-642-27786-3_1573-1.

(8) Dauner, A.; Agrawal, P.; Salvatico, J.; Tapia, T.; Dhir, V.; Shaik, S. F.; Drake, D. R.; Byers, A. M. The in Vitro MIMIC® Platform Reflects Age-Associated Changes in Immunological Responses after Influenza Vaccination. Vaccine 2017, 35 (41), 5487–5494. https://doi.org/10.1016/j.vaccine.2017.03.099.

(9) Shanti, A.; Samara, B.; Abdullah, A.; Hallfors, N.; Accoto, D.; Sapudom, J.; Alatoom, A.; Teo, J.; Danti, S.; Stefanini, C. Multi-Compartment 3D-Cultured Organ-on-a-Chip: Towards a Biomimetic Lymph Node for Drug Development. Pharmaceutics 2020, 12 (5), 464.

(10) Pruitt, H. C.; Lewis, D.; Ciccaglione, M.; Connor, S.; Smith, Q.; Hickey, J. W.; Schneck, J. P.; Gerecht, S. Collagen Fiber Structure Guides 3D Motility of Cytotoxic T Lymphocytes. Matrix Biol. J. Int. Soc. Matrix Biol. 2019. https://doi.org/10.1016/j.matbio.2019.02.003.

(11) Stachowiak, A. N.; Irvine, D. J. Inverse Opal Hydrogel-Collagen Composite Scaffolds as a Supportive Microenvironment for Immune Cell Migration. J. Biomed. Mater. Res. A 2008, 85 (3), 815–828. https://doi.org/10.1002/jbm.a.31661.

(12) Kobayashi, Y.; Watanabe, T. Gel-Trapped Lymphorganogenic Chemokines Trigger Artificial Tertiary Lymphoid Organs and Mount Adaptive Immune Responses In Vivo. Front. Immunol. 2016, 7.

(13) Luther, S. A.; Bidgol, A.; Hargreaves, D. C.; Schmidt, A.; Xu, Y.; Paniyadi, J.; Matloubian, M.; Cyster, J. G. Differing Activities of Homeostatic Chemokines CCL19, CCL21, and CXCL12 in Lymphocyte and Dendritic Cell Recruitment and Lymphoid Neogenesis. J. Immunol. 2002, 169 (1), 424–433. https://doi.org/10.4049/jimmunol.169.1.424.

(14) Birmingham, K. G.; O'Melia, M. J.; Bordy, S.; Reyes Aguilar, D.; El-Reyas, B.; Lesinski, G.; Thomas, S. N. Lymph Node Subcapsular Sinus Microenvironment-On-A-Chip Modeling Shear Flow Relevant to Lymphatic Metastasis and Immune Cell Homing. iScience 2020, 23 (11), 101751. https://doi.org/10.1016/j.isci.2020.101751.

(15) Tomei, A. A.; Siegert, S.; Britschgi, M. R.; Luther, S. A.; Swartz, M. A. Fluid Flow Regulates Stromal Cell Organization and CCL21 Expression in a Tissue-Engineered Lymph Node Microenvironment. J. Immunol. Baltim. Md 1950 2009, 183 (7), 4273–4283. https://doi.org/10.4049/jimmunol.0900835.

(16) Valignat, M.-P.; Theodoly, O.; Gucciardi, A.; Hogg, N.; Lellouch, A. C. T Lymphocytes Orient against the Direction of Fluid Flow during LFA-1-Mediated Migration. Biophys. J. 2013, 104 (2), 322–331. https://doi.org/10.1016/j.bpj.2012.12.007.

(17) Belanger, M. C.; Ball, A. G.; Catterton, M. A.; Kinman, A. W. L.; Anbaei, P.; Groff, B. D.; Melchor, S. J.; Lukens, J. R.; Ross, A. E.; Pompano, R. R. Acute Lymph Node Slices Are a Functional Model System to Study Immunity Ex Vivo. ACS

Pharmacol. Transl. Sci. 2021, 4 (1), 128–142. https://doi.org/10.1021/acsptsci.0c00143.

(18) P. Huang, C.; Lu, J.; Seon, H.; P. Lee, A.; A. Flanagan, L.; Kim, H.-Y.; J. Putnam, A.; Li Jeon, N. Engineering Microscale Cellular Niches for Three-Dimensional Multicellular Co-Cultures. Lab. Chip 2009, 9 (12), 1740–1748. https://doi.org/10.1039/B818401A.

(19) Cheung, A. S.; Zhang, D. K. Y.; Koshy, S. T.; Mooney, D. J. Scaffolds That Mimic Antigen-Presenting Cells Enable Ex Vivo Expansion of Primary T Cells. Nat. Biotechnol. 2018, 36 (2), 160–169. https://doi.org/10.1038/nbt.4047.

(20) Mandal, S.; Hammink, R.; Tel, J.; Eksteen-Akeroyd, Z. H.; Rowan, A. E.; Blank, K.; Figdor, C. G. Polymer-Based Synthetic Dendritic Cells for Tailoring Robust and Multifunctional T Cell Responses. ACS Chem. Biol. 2015, 10 (2), 485–492. https://doi.org/10.1021/cb500455g.

(21) Kim, H. S.; Ho, T.-C.; Willner, M. J.; Becker, M. W.; Kim, H.-W.; Leong, K. W. Dendritic Cell-Mimicking Scaffolds for Ex Vivo T Cell Expansion. Bioact. Mater. 2023, 21, 241–252. https://doi.org/10.1016/j.bioactmat.2022.08.015.

(22) Good-Jacobson, K. L.; Szumilas, C. G.; Chen, L.; Sharpe, A. H.; Tomayko, M. M.; Shlomchik, M. J. PD-1 Regulates Germinal Center B Cell Survival and the Formation and Affinity of Long-Lived Plasma Cells. Nat. Immunol. 2010, 11 (6), 535–542. https://doi.org/10.1038/ni.1877.

(23) Origuchi, T.; Eguchi, K.; Kawabe, Y.; Mizokami, A.; Ida, H.; Nagataki, S. Synovial Cells Are Potent Antigen-Presenting Cells for Superantigen, Staphylococcal Enterotoxin B (SEB). Clin. Exp. Immunol. 1995, 99 (3), 345–351. https://doi.org/10.1111/j.1365-2249.1995.tb05556.x.

(24) Reincke, M. E.; Payne, K. J.; Harder, I.; Strohmeier, V.; Voll, R. E.; Warnatz, K.; Keller, B. The Antigen Presenting Potential of CD21low B Cells. Front. Immunol. 2020, 11. https://doi.org/10.3389/fimmu.2020.535784.

(25) Pacheco, Y.; Acosta-Ampudia, Y.; Monsalve, D. M.; Chang, C.; Gershwin, M. E.; Anaya, J.-M. Bystander Activation and Autoimmunity. J. Autoimmun. 2019, 103, 102301. https://doi.org/10.1016/j.jaut.2019.06.012.

(26) Benson, M. J.; Elgueta, R.; Schpero, W.; Molloy, M.; Zhang, W.; Usherwood, E.; Noelle, R. J. Distinction of the Memory B Cell Response to Cognate Antigen versus Bystander Inflammatory Signals. J. Exp. Med. 2009, 206 (9), 2013–2025. https://doi.org/10.1084/jem.20090667.

(27) Wan, Z.; Lin, Y.; Zhao, Y.; Qi, H. TFH Cells in Bystander and Cognate Interactions with B Cells. Immunol. Rev. 2019, 288 (1), 28–36. https://doi.org/10.1111/imr.12747.

(28) The JAK inhibitor tofacitinib regulates synovitis through inhibition of interferon-γ and interleukin-17 production by human CD4+ T cells - Maeshima - 2012 - Arthritis & Rheumatism - Wiley Online Library. https://acrjournals.onlinelibrary.wiley.com/doi/full/10.1002/art.34329 (accessed 2024-04-02).

(29) Kubo, S.; Yamaoka, K.; Kondo, M.; Yamagata, K.; Zhao, J.; Iwata, S.; Tanaka, Y. The JAK Inhibitor, Tofacitinib, Reduces the T Cell Stimulatory Capacity of Human Monocyte-Derived Dendritic Cells. Ann. Rheum. Dis. 2014, 73 (12), 2192–2198. https://doi.org/10.1136/annrheumdis-2013-203756.

3 Comparing soft lithography and micromilling approaches for fabricating immune-competent microphysiological systems with high-aspect ratio feature.

3.1 Introduction

We investigated the process of converting from conventional fabrication of immune-competent microphysiological organs-on-chip in PDMS and glass to a scalable design using thermoplastics that can be micromilled and hot embossed or injection molded.

Identifying a thermoplastic as a PDMS alternative remains challenging because few materials rival the gas-permeability and optical clarity of PDMS. It is likely that no single material would be able to replicate the properties of PDMS sufficiently to enable microfabrication, and combinations of materials may need to be applied to harness advantageous properties congruently.[17–19] One common need in MPS design is to generate separate zones that remain fluidically connected for analytical and/or biomimicry purposes, such as studies of chemotaxis.[20,21] Here, we directly compared fabrication approaches and materials by constructing a well-established four-lane chemotaxis chip via micromilled polycarbonate (PC) combined with various other materials and molded PDMS. We examined filling strategies, gas exchange, and optical clarity. Finally, we compared cell viability and chemotactic responses on both platforms.

3.2 Results

To meet the need for PDMS alternatives and streamline the prototype-to-product transition for immune-competent organs-on-chip, we developed a scalable fabrication approach (micromilling polycarbonate) and tested the resulting chips against those produced by the more traditional PDMS/soft-lithography in terms of cell patterning and ability to perform chemotaxis experiments (Scheme 1a). As a case study, we focused

on a well-established multi-lane design,[20] in which microposts between lanes enable surface-tension pinning of thermally-setting hydrogels (e.g. collagen/fibrinogen) that are flowed into the lane in the liquid state. After thermal gelation and phase conversion, the second gel lane is filled and set, and finally the media lanes are filled. We have previously fabricated this chip design in PDMS bonded to a glass bottom. This design was interesting for conversion because it enables spatial localization of cell populations in parallel lanes and the generation of chemokine gradients through the media lanes, which are common needs in more advanced organ-on-chip platforms.

First, we considered how to adapt this geometry from soft lithograph to micromilling and future hot embossing. The microposts generated via soft lithography typically contain sharp corners and a high aspect ratio (Scheme 1b), but these features are challenging to produce with modern micromilling. Therefore, after several iterations, we produced an alternative geometry that contained trenches rather than microposts (Scheme 1c), for compatibility with micromilling of polycarbonate (PC). In the new design, the trenches did not make contact with the ceiling, which provided surface-tension pinning in the z-plane, and contact between lanes allowed for fluidic connectivity across the lanes.

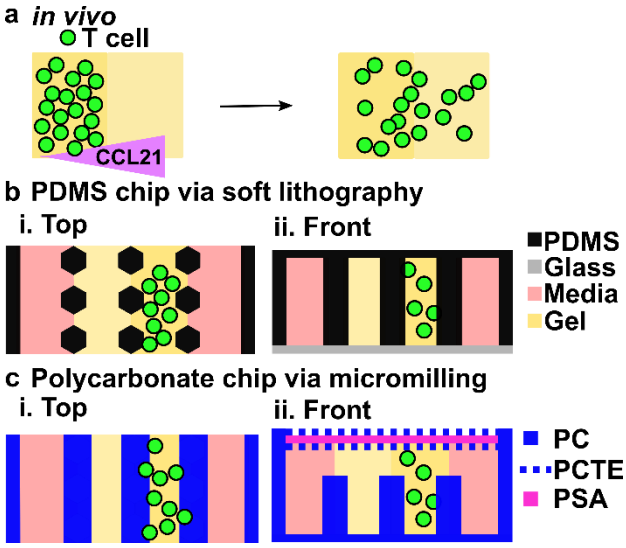

Figure 3-1 Approach for designing a chemotaxis chip out of micromilled polycarbonate to pivot from PDMS a. Schematic of the key biological function that the chips were designed to mimic: T cells in tissue responding chemotactically to a CCL21 gradient. (b,c) Schematic of (b) a PDMS chemotaxis chip designed with microposts and (c) a polycarbonate chemotaxis chip designed with trenches and a track-etched polycarbonate-membrane top (not shown to scale).

permeability for maintaining oxygen in 3D on chip cultures. We designed the chip to have an open-top PC chamber that was sealed with a lid via pressure sealed adhesive. Preliminary viability assessments in PDMS indicated that gas exchange for maintaining viable cell cultures primarily occurred through the media resvoirs, and not through the PDMS (data not shown), which led us to an initial micromilled chip design having a gas-impermeable, PC lid. Unexpectedly, we observed that thermally-setting collagen fibrinogen hydrogel degasses during gelation, resulting in bubble formation in the chamber (Fig 1a,ii). We had never considered this effect when using PDMS, as the gas released during gelation was likely absorbed into the PDMS (Fig 1a,i). To address this, we tried using track-etched polycarbonate (PCTE) membrane, but a single layer of PCTE was too delicate to resist the force of injection (data not shown). In contrast, laminating two PCTE layers with silicone-based pressure sealed adhesive in between

resulted in a sufficiently rigid layer for injecting. To assess the gas-permeability of each lid material, we filled the gel lanes with 0 °C collagen/fibrinogen gel followed by 4 °C PBS, imaged any initial bubble nucleation at 1 hr, and incubated the chips in a 37 °C cell-culture incubator overnight before final imaging. We observed that PC chips configured with PDMS and PCTE roofs were sufficiently degassed after overnight incubation to avoid major disruption of cell cultures, whereas PC chips with a PC roof did not.

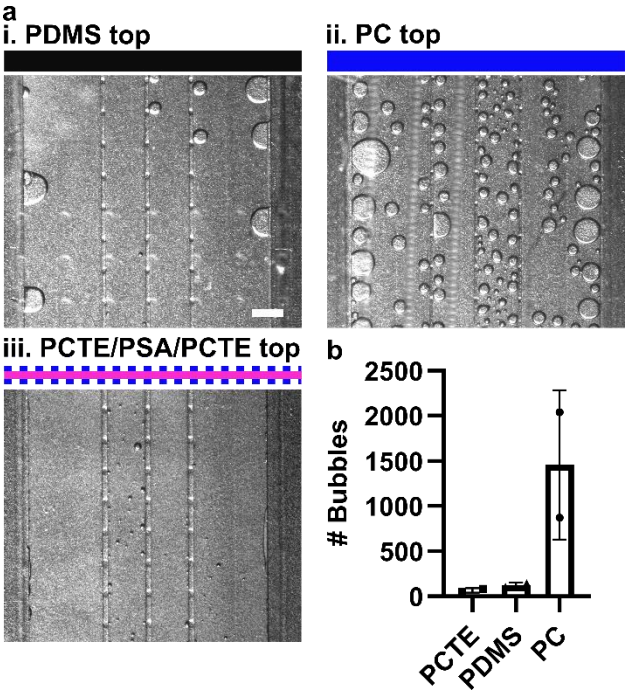

Figure 3-2 Laminated track-etched polycarbonate membranes enabled gas exchange. (a) Brightfield images of micromilled polycarbonate chips enclosed with a (i) PDMS, (ii) PC, and (iii) PCTE top that were filled with hydrogel and media, and then incubated overnight. Scale bar is 1 mm. (b) Quantification of bubbles remaining within the chips.

Next, we compared the micromilled “trench” against the soft-lithography micropost for their ability to maintain separation between cell populations during loading. Pre-labeled CD4+ T cells were resuspended in a thermally-setting, collagen-fibrinogen hydrogel, then injected into a gel lane. After allowing gelation to occur in a 37 °C incubator, the

second lane was filled with CD4+ T cells that were labeled using a different color fluorescent dye. We observed both the PDMS micropost and PC trench geometries effectively maintained separation of cell populations prior to gelation, resulting in adjacent and abutting 3D cultures. The resulting spatial arrangements were complementary. In the PDMS chip, neighboring cell populations could interact freely in the x/y plane between posts, whereas neighbors in the PC chip were connected at a higher plane, meeting atop the central trench (Fig 3 a,b iii).

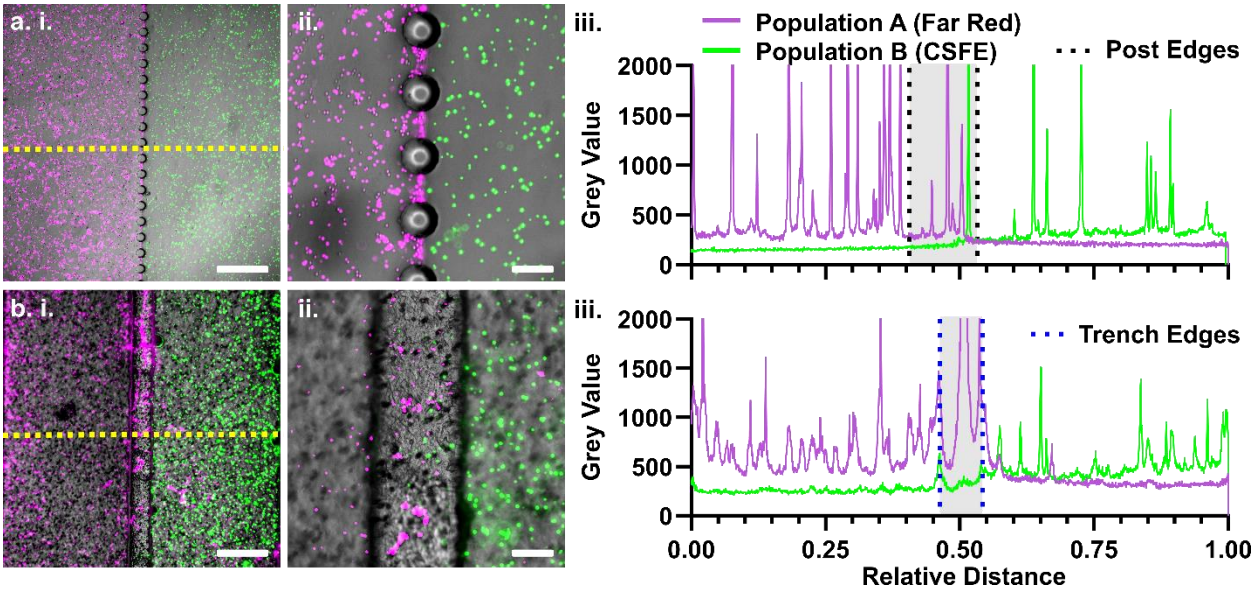

Figure 3-3 PDMS and PC chemotaxis chips enable patterning of adjacent and abutting, fluidically connected cell populations. Fluorescence images of (a) PDMS chip and (b) PC chip loaded wit h separate populations of CD4+ T cells labeled with Celltrace FarRed (magenta) and CFSE (green). (i) Scale Bar: 500 µm. (ii) Zoom on border. Scale Bar: 100 µm. (iii) Line scan measurements of fluorescent channels.

To determine if the PC and PDMS chips were functionally equivalent MPSs for lymphocyte culture, we cultured primary, human naïve CD4+ T cells on chip for 72 hr, then assessed the cells' viability and chemotactic responsiveness (Fig 3). We observed no difference in viability between the off-chip controls (2D culture), PC, and PDMS chips at 72 hr (Fig 3a,b). To assess cell migration, we set up a CCL21 gradient on chip, which

is a well-established gradient that naïve CD4+ T cells migrate toward *in vivo* via CCR7, by flowing CCL21 into the media opposite to the lane in which cells were cultured, then assessed cell migration into the adjacent lane after 1 hr. We observed a chemotaxis response in the PDMS chip, measured by % cell area in the entire width of the adjacent lane, but saw a different response in the PC chip (Fig 3c,d). There, we observed cells migrated to the right side of the trench top (Fig 3e), and saw a significant difference when measuring in that area specifically. The difference in chemotaxis responses in the PC chip when compared to the PDMS chip may be caused by cells moving in the z-plane to overcome the trench prior to entering the right lane.

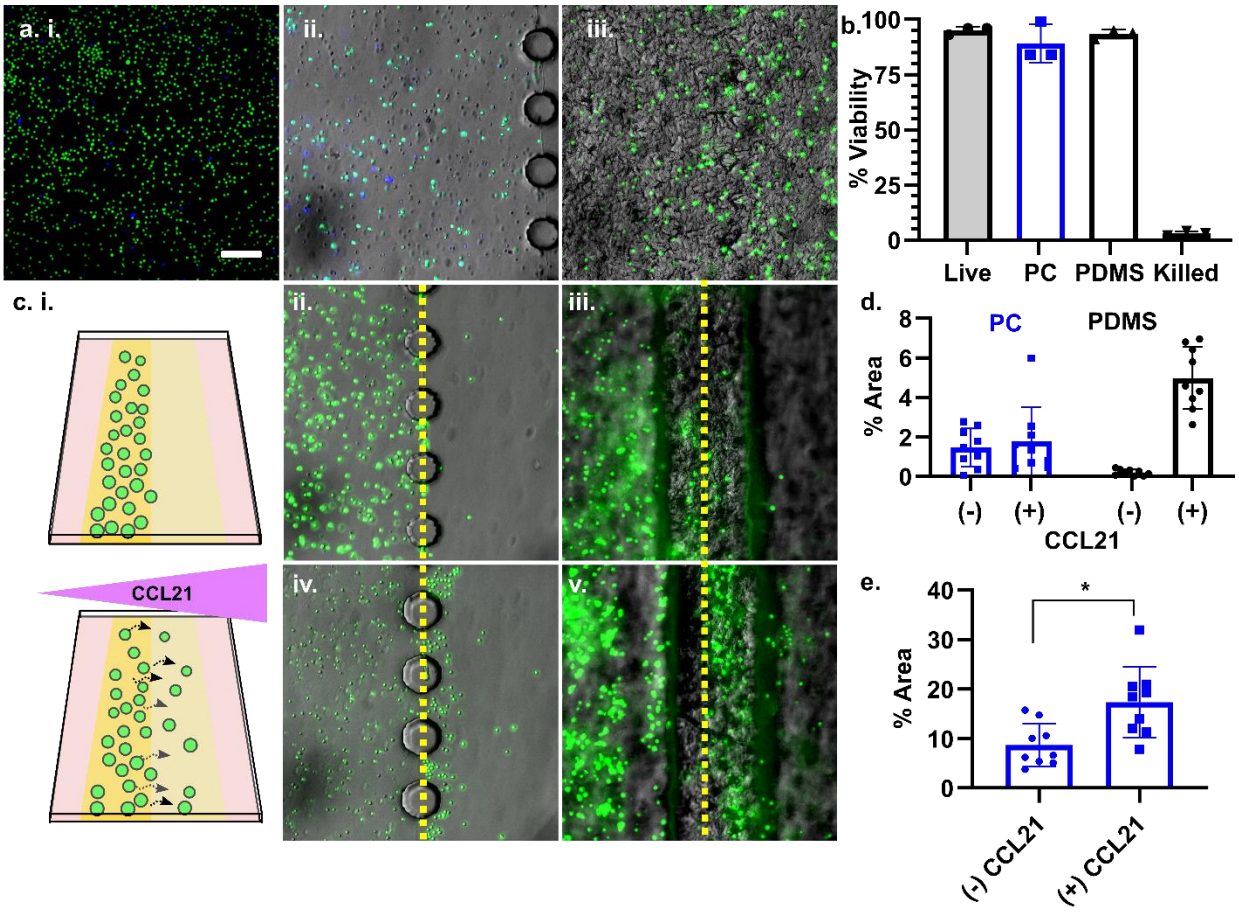

Figure 3-4 PDMS and PC chemotaxis chips enable 72 hr cell viability and chemotaxis response across gel lanes. (a) Images from viability assessment (calceinAM/Live/Green, DAPI/dead/Blue) of the (i) 2D control, (ii) PDMS chip, (iii) PC

chip. (b) Quantification of viability of CD4+ T cells cultured on PDMS and PC chips, versus a “live” off-chip control held in standard 2D culture. (c) (i) schematic of chemotaxis assay. Fluorescence images of before (ii. PDMS, iii, PC) and after (iv. PDMS, v. PC) images of calceinAM labeled CD4+ T cells on PDMS and PC chips following 60 minutes of culture with a CCL21 gradient. (d) quantification of chemotaxis response determined by calculating % cell area on the right side of the yellow dotted line. (e) alternative analysis of PC chips by calculating % cell area on the right side of the trench only. Scale bar: 100 µm.

3.3 Discussion

The results presented herein indicate successful production two complementary MPSs with orthogonal fabrication approaches. The process of fabricating and using the micromilled PC chip led to our observation that the collagen/fibrinogen matrix off-gasses during gelation, which we had not previously appreciated due to PDMS’s high gas-permeability (Fig 2). Overcoming this problem required a multi-layer approach with track-etched PC membranes and pressure sealed adhesive to both seal the chamber and allow gas-exchange.

In addition to gas-permeability, we had not previously appreciated the rigidity of PDMS when used at 2-3 mm thickness for microfluidic devices. PDMS of this thickness does not expand significantly when a 100-150 µm high channel is filled with fluid, and this undervalued property is convenient when using a micropost-enabled surface tension barrier system. When switching to a PCTE/PSA/PCTE chamber roof, which was <100 µm thick, we discovered a surface tension barrier could not form because the roof would expand slightly under fluid pressure. This problem was addressed by holding a rigid glass slide on top of the chip during filling. Lastly, the elasticity of PDMS is considerably useful when producing inlets for pipetting or making larger punches to produce cell-culture reservoirs as the elasticity seals to the injecting port and prevents backflow. This simple feature of every microfluidic chip can be challenging to replicate in

hard plastic. We found that hard-plastic pipette tip adaptors aided in filling only when an additional rubber adaptor was used to “squeeze” the pipette tip into the inlet.

While these problems may seem inconsequential for operating a single chip, small adaptor requirements (glass slides, pipette tip adaptors, etc.) increase the time/chip requirement. Longer replicates can significantly increase the labor requirement for setting up an experiment. For example in this work, the PDMS chip was filled in ~10 seconds, whereas a single PC chip was filled in 5 minutes. Therefore, an experiment with four conditions (n=3 chips/condition) would require two minutes of labor when operating the PDMS chips compared to one hour of labor with the PC chips.

3.4 Conclusion

We successfully converted a microfluidic chemotaxis chip from molded PDMS to micromilled polycarbonate, while learning that some materials properties such degassing and rigidity were more important than anticipated. We optimized the device layout to have a gas-permeable roof, and validated that separation of cell populations, cell viability, and a chemotaxis response was nearly equivalent on the PDMS and PC chips. Some work would remain for this design to be made more user friendly, and these lessons should be taken into account in future conversions.

3.5 Method

3.5.1 Fabrication of chemotaxis chips

The PDMS/glass chip was designed in AutoCAD LT 2023 to have four parallel channels separated by arrays of hexagonal microposts. The outer media channels each had 8-mm diameter inlets and outlets that served as media reservoirs. The inner gel channels had 0.75-mm inlets and outlets. Excluding the converging, angled channel regions, the

media lanes were (WxHxL) 2.45x0.130x14.81 mm and the gel lanes were 1.4x0.130x15.4 mm.

Master molds for the single-layer PDMS/glass chips were prepared using standard photolithography methods as previously described.[22] Drawings were printed on transparency sheets at 20,000 DPI (CAD/Art Services, Inc, Brandon, Oregon). SU8 was spin-coated onto 3” silicon wafers (University Wafer, South Boston MA, USA) to reach a thickness of 115-130 µm. Wafers were exposed to ozone and vapor silanized with Trichloro (1H,1H,2H,2H-perfluorooctyl) silane (Sigma Aldrich) for 2 h. PDMS was combined with crosslinker (Sylgard 184 Silicone Elastomer, Ellsworth Adhesives, Germantown WI, USA) at 10:1, degassed, poured over SU8 molds, then degassed again to ensure air was not trapped in the recessed micropost area. Finally, PDMS was cured at 70 °C for a minimum of 2 h.

Once prepared, PDMS layers were punched to form 8 mm cell culture media resvoirs and 0.75 mm gel lane inlets. Layers were exposed to ozone for 90 sec followed by bonding to a standard (1 mm) glass slide. Ozone cleaning followed by bonding at 120 °C for two hours was sufficient for sterilization.

Micromachining the polycarbonate chips was performed by ALINE (California). The micromachined chip chamber dimensions were identical to the PDMS design, with continuous trenches rather than microposts.

Once polycarbonate bottom layers were prepared, top layers (PC and PDMS) were cut to shape. The PCTE-PSA-PCTE layer was prepared by taping a 10 cm diameter hydrophobic 10 µm pore PCTE membrane (Lynntech) to a hard surface. A larger piece

of silicone-based pressure-sealed adhesive (Lynntech) was layered over the PCTE, and finally a second PCTE membrane was layered on the PSA. The layer was then cut to the appropriate size. After bonding, chips were sterilized by UV light in a biosafety cabinet for 10 min prior to cell work.

3.5.2 Collagen/Fibrinogen Hydrogel Loading

Collagen (IBIDI) was prepared to 1.5 mg/mL via diluting and pH adjustment according to manufacturer's protocol. Fibrinogen (sigma) was diluted into the gel to a final concentration of 1 mg/mL. Once mixed, cells were resuspended in the collagen gel at $1x10^7$ cells/mL, or neat gel was injected directly into the channel inlet. 5 µL were injected with a standard 10 uL pipette tip into each end of a gel lane so that the gels would meet in the middle. For the polycarbonate chip, an 8 mm PDMS round with a 0.75 mm punch was used as a pipette tip adapter to prevent backflow while injecting. After filling one gel lane, the chips were incubated for 30 min in a 37 °C cell culture incubator in a petridish containing PBS-soaked sponges (sponges prevented chips from dehydrating and remained for the remainder of the experiment). Immediately after, the second gel lane was filled followed by repeated incubation. Cell-laden gel could be loaded during the first or second step. After both lanes were filled, 100-200 µL of AIM V media (ThermoFisher) was added to each of the four media reservoirs. Media lanes were filled by pipetting at an angle so that the tip made contact with the lane inlet. When cells were used, chips were incubated for at least two hours prior to initiating further experiments.

3.5.3 Cell sourcing

As described previously,[22] human naïve CD4+ T lymphocytes were isolated using immunomagnetic separation from TRIMA collars obtained from healthy donors following platelet apheresis (StemCell Technologies). Purity of naïve CD4+ T cells was determined via flow cytometry (CD4+, CD45RA+, CD45RO-). Cells were used immediately or plated at 1.5-3x10^6 cells/mL in AIM V media with 10 ng/mL IL-7 (R&D Systems; Bio-techne, Inc.).

3.5.4 Microscopy

Images were taken on either the Zeiss AxioZoom or AxioObserver microscopes. The AxioZoom was fitted with an HXP 200C metal halide lamp, PlanNeoFluor Z 1x objective (0.25 NA FWD 56 mm), and Axiocam 506 mono camera. The Zeiss Filter Sets, 38 HE (Ex: 470/40, Em: 525/50), 43 HE (Ex: 550/25, Em: 605/70); 64 HE (Ex: 587/25, Em: 647/70); and 49 HE (Ex: 365, Em: 445/50) were used. Brightfiled images were acquired as transmitted light. Zen 3 Blue software was used during acquisition. Images were analyzed in ImageJ v1.53t.

The AxioObserver 7 inverted microscope was fitted with the Colibri.7 LED light source, EC Plan-Neofluar 5× objective (N.A. = 0.16, WD = 18.5 mm), and ORCA-Flash4.0 LT + sCMOS camera (Hamamatsu). For fluorescence imaging, the filter used was a Zeiss 112 HE LED penta-band.

3.5.5 Patterning separate populations of T cells

When demonstrating separation of cells on chip, cells were prelabeled with 10 µM Calcein AM or 1 µM NHS rhodamine and then loaded onto PDMS/glass or PC/PCTE chips in separate lanes. Rhodamine dye was added to the media lane and the chip was imaged after 15 minutes to both show separation of cell populations and

demonstrate fluidic connectivity via rhodamine dye diffusion across lanes. Images were analyzed with ImageJ by performing linescan quantification for each channel.

3.5.6 Cell viability assessment

Viability of T cells was assessed by loading PC/PCTE and PDMS/glass chips with cell-laden gel, culturing for 72 hr, and then replacing media with a viability stain (10 µM CalceinAM and 1 µM DAPI in HBSS). Chips were then incubated for 2 hours and imaged. Cells were also plated at $1x10^6$ cells/mL as an off-chip live control. For killed controls, cells were incubated with 70% EtOH for 10 minutes and resuspended in viability stain. Images were analyzed with ImageJ using the particle analyzer, with circularity set to 0.5-1 and size 12.5-500 μm^2. Viability was calculated as #CalceinAM+ cells/(#CalceinAM+ cells + DAPI+ cells).

3.5.7 Chemotaxis assay

To assess chemotaxis response on chip, PC/PCTE and PDMS/glass chips were loaded as described. After allowing cells to rest overnight, chips were imaged, then 0.1 µM CCL21 in AIM V media was injected into the left media lane of the chip. Chips were incubated with the CCL21 gradient for 1 hour, then stained by flowing 5 uM calceinAM stain, incubating for 1 hour, and imaged. Images were analyzed with ImageJ by using the particle analyzer and finding cells within each gel lane. Chemotactic responsive cells were identified by measuring % calceinAM+ area within the gel lane closest to the CCL21 gradient, and subtracting from the image taken before the gradient was established to account for random T cell migration.

3.6 References

(1) Hassanpour-Tamrin, S.; Sanati-Nezhad, A.; Sen, A. A Simple and Low-Cost Approach for Irreversible Bonding of Polymethylmethacrylate and

Polydimethylsiloxane at Room Temperature for High-Pressure Hybrid Microfluidics. *Sci. Rep.* **2021**, *11* (1), 4821. https://doi.org/10.1038/s41598-021-83011-8.
(2) Hosic, S.; Bindas, A. J.; Puzan, M. L.; Lake, W.; Soucy, J. R.; Zhou, F.; Koppes, R. A.; Breault, D. T.; Murthy, S. K.; Koppes, A. N. Rapid Prototyping of Multilayer Microphysiological Systems. *ACS Biomater. Sci. Eng.* **2021**, *7* (7), 2949–2963. https://doi.org/10.1021/acsbiomaterials.0c00190.
(3) Campbell, S. B.; Wu, Q.; Yazbeck, J.; Liu, C.; Okhovatian, S.; Radisic, M. Beyond Polydimethylsiloxane: Alternative Materials for Fabrication of Organ-on-a-Chip Devices and Microphysiological Systems. *ACS Biomater. Sci. Eng.* **2021**, *7* (7), 2880–2899. https://doi.org/10.1021/acsbiomaterials.0c00640.
(4) Huang, C. P.; Lu, J.; Seon, H.; Lee, A. P.; Flanagan, L. A.; Kim, H.-Y.; Putnam, A. J.; Jeon, N. L. Engineering Microscale Cellular Niches for Three-Dimensional Multicellular Co-Cultures. *Lab. Chip* **2009**, *9* (12), 1740–1748. https://doi.org/10.1039/B818401A.
(5) Wu, J.; Wu, X.; Lin, F. Recent Developments in Microfluidics-Based Chemotaxis Studies. *Lab. Chip* **2013**, *13* (13), 2484–2499. https://doi.org/10.1039/C3LC50415H.
(6) Ortiz-Cárdenas, J. E.; Zatorski, J. M.; Arneja, A.; Montalbine, A. N.; Munson, J. M.; Luckey, C. J.; Pompano, R. R. Towards Spatially-Organized Organs-on-Chip: Photopatterning Cell-Laden Thiol-Ene and Methacryloyl Hydrogels in a Microfluidic Device. *Organs---Chip* **2022**, *4*, 100018. https://doi.org/10.1016/j.ooc.2022.100018.

4. Quantification of fractional and absolute functionalization of gelatin hydrogels by optimized ninhydrin assay and 1H NMR

4.0 Prelude to Chapters 4 and 5:

With the goal of making fundamental advancements toward accurately mimicking the spatial organization of tissue, efforts in the Pompano Lab have enabled the photopatterning of cell-laden hydrogels within a microfluidic chamber. A summary of published work from a prior graduate student regarding this effort is included here to illustrate this method:

4.0.1 Summary of in situ photopatterning of cell-laden hydrogels

From "Photopatterning cell-laden thiol-ene and methacryloyl hydrogels in a microfluidic device." By Jennifer Ortiz-Cárdenas, Jon Zatorski, Abhinav Arneja, Alyssa Montalbine, Jennifer Munson, Chance John Luckey, & Rebecca Pompano, R. R. (2022). Organs-on-a-Chip, 4, 100018:

The development of biomimetic organ models offers the potential to replicate human biology in a controlled in vitro system. Standard technologies to micropattern 3D cultures on-chip are limited in their ability to create complex spatial structures, and thus cannot fully replicate the intricate spatial organization of native tissues or allow full freedom of high-throughput array design. Integration of 3D cultures with microfluidics is often accomplished by direct micropatterning inside a microfluidic chip, usually through the use of laminar flow and/or physical support structures *(as shown in Chapter 2 and 3 of this dissertation)*. These patterning strategies struggle to generate free-standing islands, concentric features, or non-linear, abutting cultures.

A potential strategy to overcome these limitations is photolithography, in which light passes through a photomask to pattern a photo-crosslinkable culture matrix (Fig. 4-0-1). Patterning 3D cultures on-chip with the goal of recapitulating complex organ architecture requires crosslinking cell-laden hydrogels without cytotoxicity, while still

achieving biomimetic mechanical properties and stability under fluid flow. In *Ortiz-Cárdenas et al., (2022)*, cell-laden hydrogels were patterned into customizable, free-standing structures on a microfluidic chip by *in situ* photolithography.

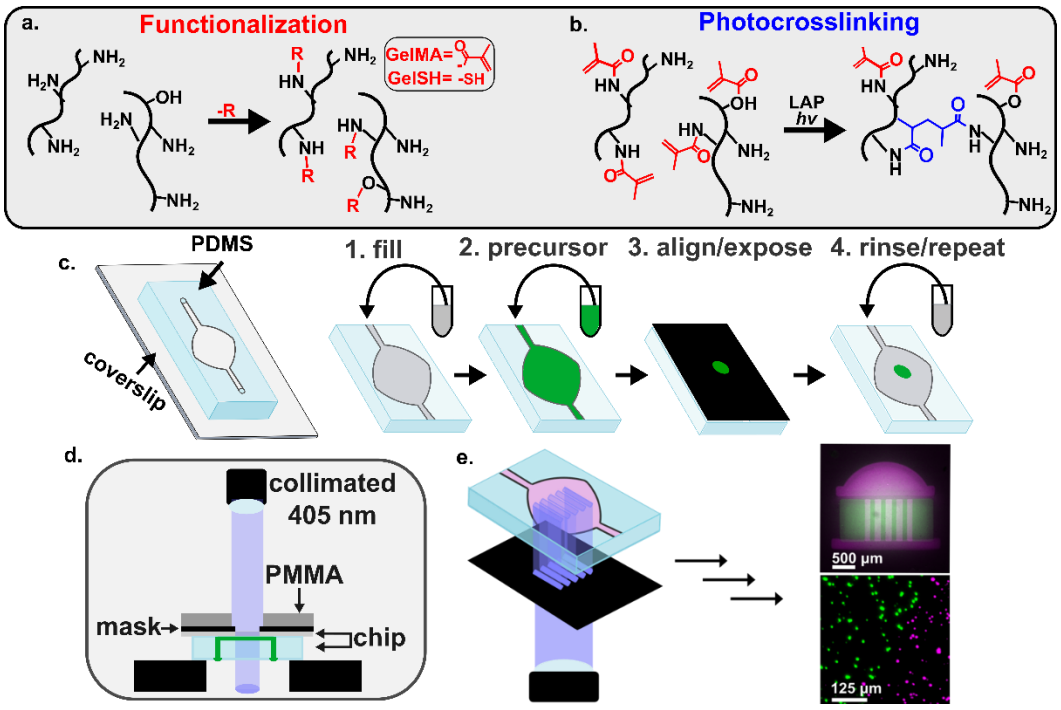

Figure 4-0-1 (From Ortiz-Cárdenas et al., (2022)). Photocrosslinkable hydrogels and photolithography enable complex tissue designs within a microfluidic chamber.
(a) Gelatin hydrogels were chemically modified to have methacryloyl or thiol functionalizations. (b) In the presence of a photoinitiator and blue light, functional groups crosslink. (c) Photopatterning approach: A microfluidic chamber was 1. injected with PBS (grey), then 2. displaced with hydrogel precursor (green). 3. A photomask was overlaid prior to exposure, and 4. the uncrosslinked hydrogel was rinsed away. (d) Exposure schematic with hydrogel-filled chip, photomask, and light source. (e) Repeated exposures enabled complex, cell-laden architecture.

***In situ* photopatterning of cell-laden hydrogels fundamentally advanced biofabrication methodology by enabling complex, microscale tissue mimics. However, this effort also revealed a challenging inverse relationship between cell viability and the need for mechanically stable gels.** We observed that stable photopatterned gels required a high gel-density such that cells could no longer move, and viability was adversely affected. Adding to this, we struggled to screen patterning conditions due to a lack of methods for predicting the stability of photopatterned hydrogels under physiological conditions. Toward

solving this problem, we committed to a two-pronged approach: One approach was to tune hydrogel composition, with the goal of improving cell motility and viability. The other was to develop analytical methods to characterize photocuring hydrogels.

4.0.2 A three-lane surface-tension chip enabled identification of a more biocompatible photocrosslinking gel formula.

While I did not lead the effort to tune gel composition for improving biocompatibility, I did develop the strategy to test cell motility within mechanically unstable gels. Using the microfluidic chamber described in Chapter 2 of this dissertation, we were able to screen gels which were not mechanically stable enough to be photopatterned. Extending this further, we utilized the adjacent lanes to assess the motility of multiple cell types simultaneously within various gel formulas. In doing so, fibroblast-T cell crosstalk was modelled in which primary T cells were loaded in the outer lanes and crosslinked before human lymphatic fibroblasts (HLFs) were loaded in the center lane and crosslinked. This produced a spatial organized co-culture (Figure 4-0-2a). Unlike monitoring random cell motility, this test assessed a more biomimetic motility process, where T cells were chemoattracted towards the lymphoid fibroblasts.

We saw HLFs spread in collagen gel, but did not spread at all in the photocuring GelSH gel, where T cells remained round and immobile (Figure 4-0-2b). In collagen gel, some of the T cells migrated into the center lane, and a small number were observed to co-localize with HLFs there when imaged after 2 days. Interestingly, co-cultures in a hydrogel blend, GelSH + 60% collagen, yielded HLF spreading and redistribution of the T cells in some regions but not others. Stromal cell morphology in the gelSH/collagen blend was distinct and more variable than the other groups. In two out of six chips, HLFs spread and formed tighter, more contractile networks than were seen in collagen gels. CD4+ T cells appeared to have moved and clustered within their lanes, unlike in neat GelSH, and migrated T cells were frequently visible within the center

lane when imaged after 2 days, though with more variability than in collagen gels (Figure Fig. 4-0-2c). Also, there was less co-localization of T cells with HLFs than was seen in collagen gels.

Thus, the surface-tension chip enabled screening for tissue-level properties, such as cell-cell colocalization, which advanced our progress toward identifying more biocompatible gel formulas.

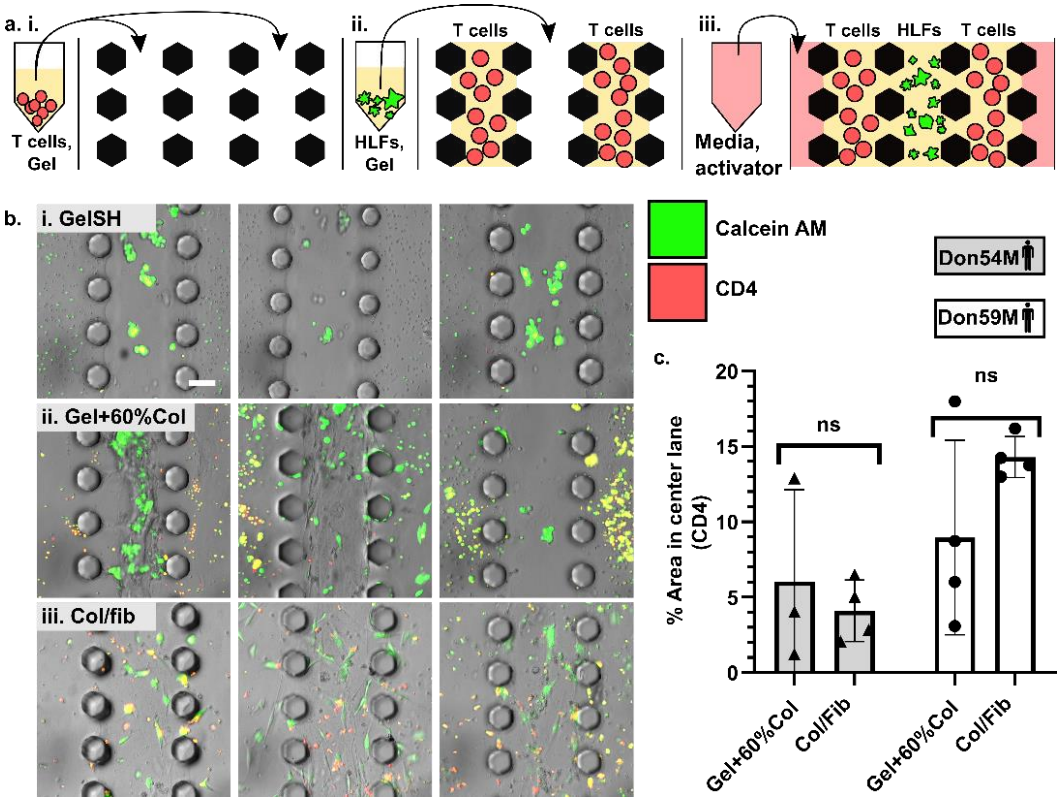

Figure 4-0-2. GelSH + 60% collagen hydrogel enabled lymphocyte-stromal colocalization in a microphysiological system.
(a) Schematic showing the establishment of CD4+ T cell and HLF co-cultures on a microfluidic chip. (i) A T cell-laden gel precursor was loaded, then cured (thermal and/or photo-exposed, depending on the hydrogel formulation). (ii) A stromal cell-laden gel precursor was loaded, then cured. (iii) Media was added to outer lanes. (b) Representative images of CD4+ T cells and HLFs in each gel after 2-day culture. Cells were labelled with anti-CD4 (red) and Calcein AM (green) (n = 2 donors, each dot is a chip). Overlays of brightfield and fluorescence images are shown; three representative images shown for each condition. Scale bar is 100 µm. (c) Quantification of CD4+ area in center lane, for two human donors. Each dot represents one chip (mean of three regions imaged per chip). Data were analyzed using two-way ANOVA with Sidak's multiple comparisons, ns $p > 0.05$. Brightfield images showed that no lymphocytes were detected in center lanes for GelSH cultures; these were omitted from the plot due to poor immunofluorescence staining in that gel.

4.0.3 Multiple analytical techniques were established for characterizing photopolymerizing hydrogels.

The other, more fundamental approach toward advancing tissue engineering was to develop analytical techniques for characterizing light-curing gel chemistries. Toward this goal, I led the development of the analytical techniques described in the remainder of Chapter 4 and Chapter 5.

4.1 Abstract

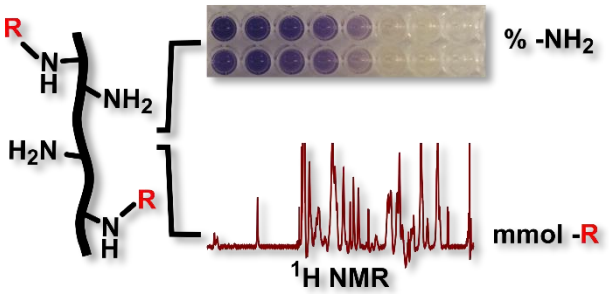

3D cell culture in protein-based hydrogels often begins with chemical functionalization of proteins with cross-linking agents such as methacryloyl or norbornene. An important and variable characteristic of these materials is the degree of functionalization (DoF), which controls the reactivity of the protein for crosslinking and therefore impacts the mechanical properties and stability of the hydrogel. Although ^{1}H-NMR has emerged as the most accurate technique for quantifying absolute DoF of chemically modified proteins, colorimetric techniques still dominate in actual use and may be more useful for quantifying fractional or percent DoF. In this work, we sought to develop an optimized colorimetric assay for DoF of common gelatin-based biomaterials and validate it versus NMR; along the way, we developed a set of best practices for both methods and considerations for their most appropriate use. First, the amine-reactive ninhydrin assay was optimized in terms of solvent properties, temperature, ninhydrin concentration, and range of gelatin standards. The optimized assay produced a linear response to protein concentration in a convenient, 96-well plate format, and yielded a fractional DoF similar to NMR in most cases. In comparing to NMR, we identified that DoF can be expressed as fractional or absolute, and that fractional DoF can be inaccurate if the amino acid content of the parent protein is not properly accounted for. In summary, the fractional DoF of methacryloyl- and norbornene-functionalized gelatins was quantified by an optimized colorimetric ninhydrin assay and orthogonally by ^{1}H-NMR. These methods will be valuable for quality control analysis of protein-based hydrogels and 3D cell culture biomaterials.

Keywords

gelatin methacryloyl, GelMA, gelatin norbornene, GelNB, assay development, protein NMR, biomaterials

4.2 Introduction

Hydrogels composed of functionalized, protein-based polymers have been used increasingly in regenerative medicine and tissue engineering [23–25]. Applications such as controlled release and tunable 3D cell culture require precisely controlled cross-linking

density, which mediates stiffness, extrudability, and shear-thinning properties. Naturally derived hydrogel materials such as gelatin are a mainstay of the field due to their low toxicity, cell-adhesion motifs, and biodegradability [24,26]. Thus, much recent work focuses on adding chemically defined and tunable functionality to these materials [27–29].

While natural gelatin offers thermal control over gelation, inclusion of photoreactive functional groups, such as methacryloyl (GelMA) or norbornene (GelNB), provides on-demand gelation with tunable stiffness (Fig. 1a,b) [27,28]. Claaßen et al. (2018) showed that for methacryloyl-modified gelatin, functionalization occurs primarily at lysine and hydroxylysine residues initially. As the ratio of methacryloyl (MA) to amines is increased and 100% of amines are reacted, functionalization also occurs at other residues such as threonine, serine, and tyrosine, though at low frequency compared to lysines [30,31]. These hydrogel chemistries are rapidly gaining popularity, and studies have recently focused on improved processability and larger batch sizes [29,32]. As interest grows in scaled-up production and novel chemical modifications of gelatin, so does the need for reproducible and simple assays for quality control and prototyping [33].

During the synthesis of modified gelatin, the degree of functionalization (DoF) -- defined as the quantity or fraction of functional groups reacted -- varies with both the gelatin starting material and the reaction conditions. Both the exact amino acid content and the availability of reactive functional groups can vary between batches and sources of gelatin (Table 4-1), a natural product that is sourced from animal-derived collagen and extensively processed in acidic or basic conditions. This variation extends to other proteins used for chemical functionalization as well, e.g. tropoelastin [31], as well as to antibodies, in which amine content may be unknown. Beyond this variability in reactive

sites, the degree of functionalization also depends strongly on reaction conditions [28,29,33,34]. Quantification of the DoF is necessary for quality control of functionalized gelatin materials, because DoF influences the rate of polymerization, resulting stiffness, and mechanical stability of the hydrogel [27,28,35].

Table 4-1. Reported lysine and amine content of bovine and porcine gelatin.

Gelatin (species, type)	Gelatin source tissue	Lysine (mmol / g gelatin)	Amines (mmol / g gelatin)	Reference
Bovine, type B	Skin	Not Reported	0.35	[32]
Bovine, type B	Skin	0.28	0.385	[29,36]
Bovine, type B	Skin	0.100[a]	Not reported[b]	[37]
Porcine, type A	Skin	0.245[a]	Not reported[b]	[37]
Porcine, type A	Skin	0.259	0.325[c]	[30]
Porcine, type A	Not Reported	0.245[a]	0.300[a,c]	[38]

[a] These data were reported as "residue / 1000 amino acids." The values were converted to "mmol / g gelatin" by assuming an average amino acid molecular weight of 110 g/mole of amino acid.

[b] Neither the hydroxylysine nor the total amine content was reported.

[c] This value was determined by adding reported data for lysine and hydroxylysine.

^{1}H-NMR and colorimetric assays have become standard methods for assessing the DoF of functionalized proteins. ^{1}H-NMR offers direct quantification of the DoF, because the spectral peak(s) corresponding to the functional group can be easily identified and integrated. Furthermore, using an internal standard has allowed for precise determination of absolute DoF in units of moles of functional group (e.g. MA) per gram of protein [30]. However, unless the amine content is known precisely, e.g. from sequencing, the fraction of amines functionalized cannot be quantified by NMR. Furthermore, despite the accuracy of NMR methods, many biomedical researchers prefer a rapid, plate-based assay whenever possible. The continued use of colorimetric DoF assays by many research groups [31,39,40] indicates that there is a need for accurate and precise assays of this type, and an understanding of their limitations. A promising

colorimetric approach to measuring DoF is the ninhydrin assay, which reacts primary amines with a small molecule, ninhydrin, to form Ruhemann's Purple (Fig. 1c). This assay was developed originally for use with solutions of free amino acids or short peptides, and has been adapted to characterize collagen content within heterogenous biomaterials [41] and functionalized gelatin methacryloyl [35,41]. By comparing to a calibration curve, the assay provides a measure of the fraction of free amines remaining after conjugation, from which a fractional DoF is determined. These protocols vary widely and often yield non-quantitative results when applied to proteins. The typical solvents and temperatures used for the ninhydrin reaction lead to protein precipitation or poor sensitivity, thus decreasing the accuracy and precision of DoF measurement. The development of a standardized ninhydrin assay for DoF of protein-based samples, particularly gelatins, would significantly advance the development of tunable biomaterials and hydrogels. While this method can detect only amine functionalization, not functionalization of other residues, amines are the primary site of functionalization by MA under typical reaction conditions [30,31].

Here we present two advancements. First, the ninhydrin assay was optimized for work with functionalized gelatin materials using unmodified gelatin for the standard curve (Fig. 1d,e). Second, the ambiguity of the DoF expression was clarified by defining absolute and fractional DoF. With this in mind, we identified the advantages and limitations of several previously published approaches for analyzing the ^{1}H-NMR spectrum of functionalized gelatin. Finally, the optimized ninhydrin assay was validated for accuracy against protein NMR as an effective, plate-based alternative.

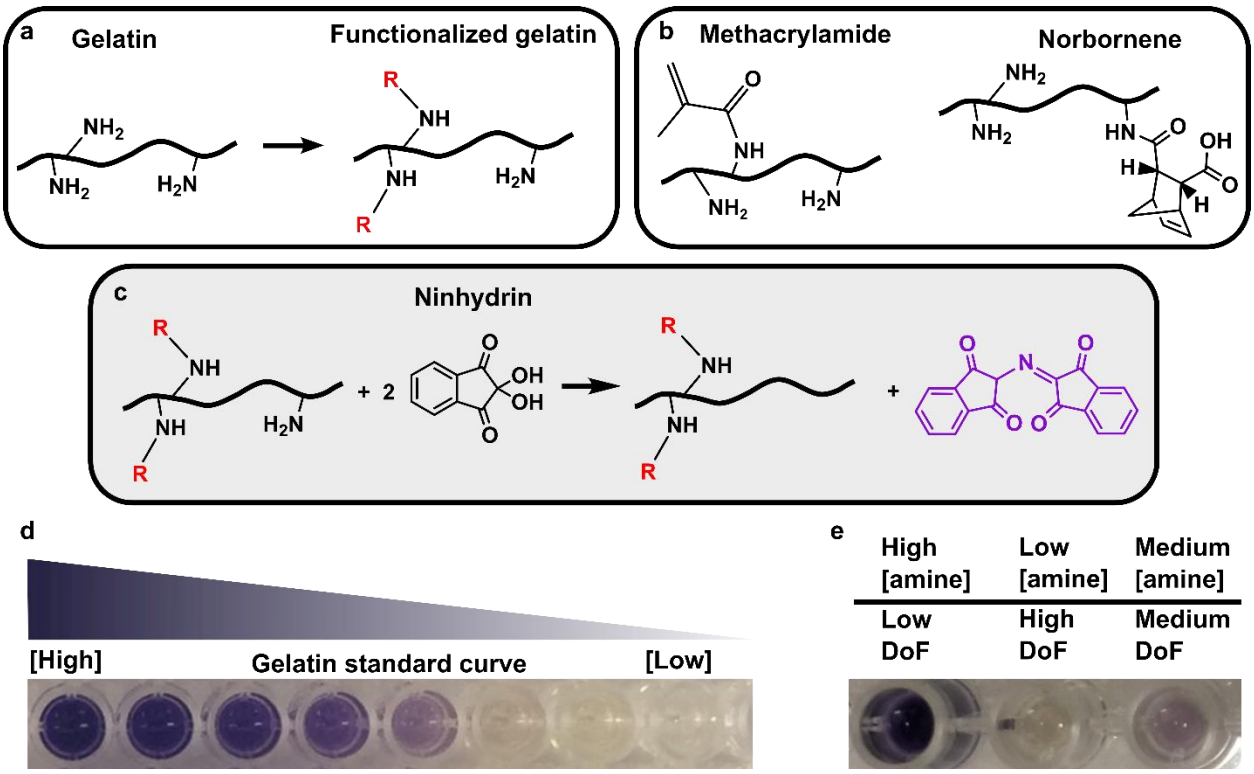

Figure 4-1 Detecting protein functionalization by loss of free amines via the colorimetric ninhydrin assay. (a) Reaction scheme for chemical functionalization of a protein by anhydrides or succinimidyl esters, which occurs primarily at free amines. (b) Structures of reaction products of amine sidechains with methacryloyl or norbornene groups. (c) Reaction scheme for the ninhydrin assay. Ninhydrin reacts with free primary amines to generate Ruhemann's Purple, a purple-colored soluble product. (d) Photo of well-plate after running the optimized assay with a gelatin standard curve. Solutions remained clear, free of precipitation, yielded a visible color change that corresponded to free amine content in the solution. (e) Photo of well plate after analyzing functionalized gelatin samples (here, GelMA). Samples yielded color changes that inversely correlate with their respective DoF values.

4.3 Results and Discussion

4.3.1 Optimization of ninhydrin assay conditions

In optimizing the ninhydrin assay for use with functionalized gelatins, we considered several factors based on our initial experience testing out a variety of reported procedures: choice of standards, prevention of precipitation via solvent selection, and optimization of ninhydrin concentration and temperature.

4.3.1.1 Selecting Standards: Standards used for the ninhydrin assay with functionalized gelatins range from purified amino acids (e.g. glycine [42]) to gelatin itself [35], and the

selection is not inconsequential. A glycine standard curve has the advantage of providing precisely known amine concentration, but does not account for absorbance by the protein itself (some modified proteins are yellow-tinged), nor for side reactions between ninhydrin and other amino acids present in the protein sample. In contrast, a gelatin standard curve more directly provides information of the fraction of amines reacted, which is useful when optimizing reaction conditions to obtain a desired DoF. Here, we chose to use the parent Type A porcine gelatin as the standard primarily because of the potential for side reactions between ninhydrin and the protein. The same lot and type of gelatin is used for the standards and the functionalized gelatin, which allows for direct determination of fractional functionalization.

4.3.1.2 Preventing precipitation. The solvent conditions described in published protocols for the ninhydrin assay vary widely depending on their application. Examples include (a) dissolving amino acids in PBS and ninhydrin in ethanol [41] and (b) dissolving gelatin in water and ninhydrin in a sodium citrate / glycerol mixture [35]. Initially, we tested these and similar protocols but found that the ethanol content in (a) caused protein precipitation, and the glycerol in (b) resulted in density gradients and irreproducible color development in our hands. Other protocols for free amino acid analysis, conducted in concentrated acids, were not tested here due to their potential to hydrolyze the protein [42]. Because of the simplicity of the components of the PBS/ethanol approach, we selected this method for further optimization with gelatin. To eliminate precipitation while achieving a measurable color change, we sought to minimize the ethanol content of the mixture while maintaining a sufficient concentration of ninhydrin. For these initial tests, the mixture was heated in polypropylene tubes in a water bath at 50 ºC and

observed for about 15 minutes. We found that a 1:8 v/v ratio of 20 mg/mL ninhydrin solution (2.2 mg/mL final ninhydrin concentration) to 20 mg/mL gelatin solution both eliminated precipitation and yielded distinct purple color development (Table 2).

Table 4-2 The concentrations and volumetric ratio of ethanolic ninhydrin solution to aqueous gelatin solution were initially adjusted to eliminate precipitation while achieving a measurable purple color change

[Ninhydrin] in ethanol, mg/mL[a]	[Gelatin] in PBS, mg/mL[a]	V_{EtOH} : V_{PBS}[c]	Final [ninhydrin], mg/mL	Absence of Precipitation?	Purple color?
3.5	3.5	20 : 1[b]	3.3	No	No
3.5	3.5	9 : 1	3.2	No	No
3.5	3.5	1 : 8	0.4	Yes	No
3.5	20	1 : 8	0.4	Yes	No
20	20	1 : 8	2.2	Yes	Yes

[a] Initial concentrations
[b] The conditions in this row were from Ma et al., (2003) [41]
[c] V_{EtOH} : V_{PBS} is the volumetric ratio of ethanol to PBS after combining reagents

4.3.1.3 Ninhydrin Concentration Optimization. Using the optimal solvent ratio (1:8 v/v EtOH:PBS), we sought to optimize the linear range of the assay by varying the concentration of ninhydrin in the final mixture. Serial dilutions of gelatin from 1-10 mg/mL were reacted in a 96-well plate at 70 °C for 30 minutes with ninhydrin at 2.2 mg/mL (12.3 mM), 4.4 mg/mL (24.7 mM), or 6.6 mg/mL (37.0 mM) (Figure 2a). We found that 2.2 mg/mL ninhydrin produced the widest linear range of absorbance. Higher ninhydrin concentrations resulted in saturated absorbance at moderate gelatin concentrations.

4.3.1.4 Reaction Temperature Optimization. The ninhydrin reaction requires elevated temperatures, and the assay is frequently conducted at temperatures between 50–100 °C [35,41]. To determine the optimal temperature for a reaction conducted in a 96-well plate format, standards (2-8 mg/mL gelatin) were prepared in the plate with 2.2 mg/mL

ninhydrin, sealed, and incubated in an oven. Color development was allowed to occur for 30 minutes at temperatures ranging from 50-80 °C (Figure 2b). A reproducible linear absorbance curve was achieved at 70 °C. Temperatures lower than 70 °C resulted in larger variability, and temperatures greater than 70 °C resulted in evaporation of the samples. Similar results were observed when standards were prepared in test tubes and allowed to incubate at 70 °C for 12 minutes.

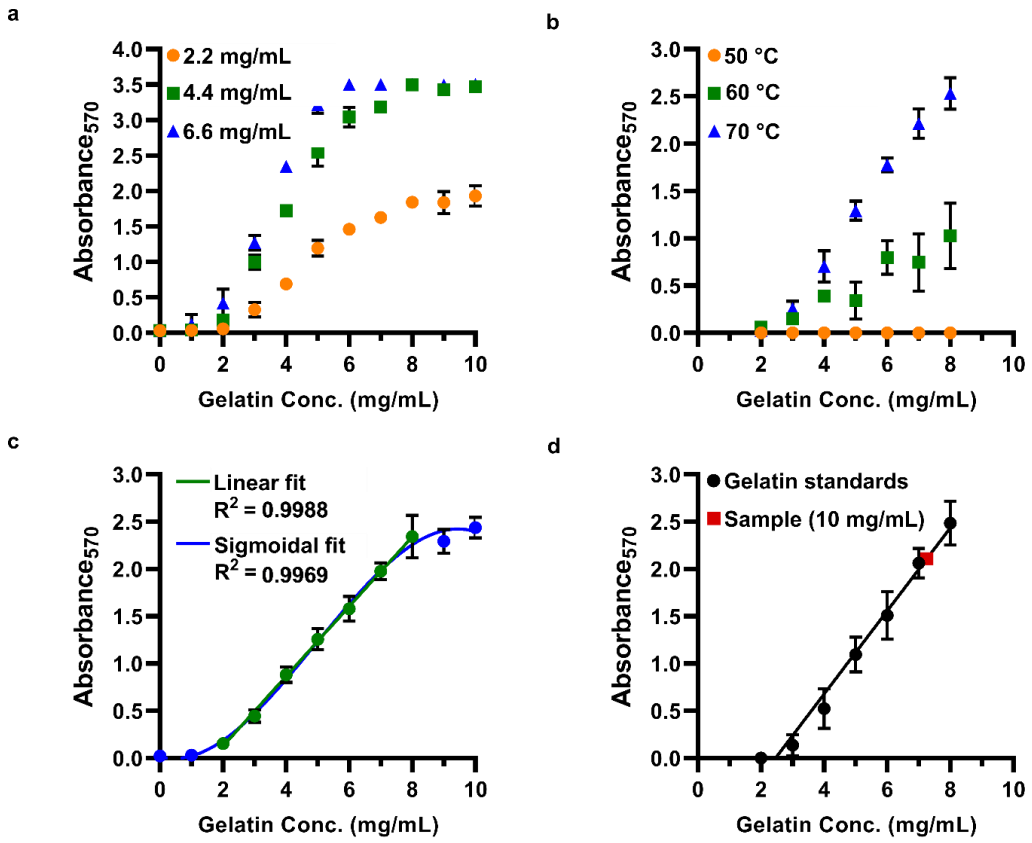

Figure 4-2 Optimization of ninhydrin assay conditions for use with functionalized gelatin in 96-well plate format. (a) Calibration curves (absorbance versus gelatin concentration) under varied ninhydrin concentrations; legend shows the final ninhydrin concentration in the reaction solution. Temperature 70 °C. (b) Calibration curves at varied reaction temperature. 2.2 mg/mL ninhydrin. (c) Expanded calibration curve, fit with a sigmoidal curve or fit in part with a linear regression. Temperature 70 °C; 2.2 mg/mL ninhydrin. (d) Determination of degree of functionalization for a representative sample of functionalized gelatin (red square). In this example, GelMA prepared at 10 mg/mL exhibited an apparent concentration of 7.3 mg/mL (DoF 27 %).

4.3.1.5 Standard Curve and Application to Functionalized Gelatin. Finally, we applied the optimized reaction conditions and tested the dynamic range of the assay in the 96-well plate assay format. As expected, no precipitation was observed, and the reaction became visibly purple at higher gelatin concentrations. A sigmoidal absorbance curve was obtained from 0-10 mg/mL gelatin, with a linear region from 2-8 mg/mL (R^2 = 0.9988) (Fig. 1d, Fig. 2c).

Functionalized gelatin samples, e.g. GelMA or GelNB, develop less purple color because fewer free amines are present. To determine the fraction of amines remaining in a sample of GelMA or GelNB, the “apparent” gelatin concentration was determined from the standard curve and normalized to the nominal concentration of the sample (Eq. 1, Materials and Methods). DoF was defined as the difference of this value from unity (Eq. 2). For example, a GelMA sample prepared at 10 mg/mL was reacted with ninhydrin and yielded an apparent concentration of 7.3 mg/mL, for a calculated DoF of 27 % (Figure 2d).

Optimizing the ninhydrin assay for intact proteins may be useful in other settings, as ninhydrin is used broadly in fields such as forensics, food science, biomedical and clinical research, and biochemistry[43]. For example, Nayuni et al., (2013) [44] showed that a clinical ninhydrin protocol was far more sensitive to free amino acids than to lysines among intact proteins, demonstrating a need for conditions that allow for color development with intact proteins.

4.3.2 Validation of ninhydrin assay versus ^{1}H NMR

Having established a robust method for colorimetric analysis, we sought to validate its accuracy and limitations in comparison to ^{1}H-NMR, the gold standard for

quantification. We tested the ninhydrin assay with both GelNB and GelMA, as these are commonly used for photopatterned cell cultures [29,35], and compared the results to DoF determined from ^{1}H-NMR.

Interestingly, multiple methods have been demonstrated for quantifying the functional group density from ^{1}H-NMR spectra, and there is no consensus in the literature on a single method of quantification. One elegant approach involves determining the molar concentration of a functional group (e.g. MA or NB) per gram of gelatin by integrating the functional group peak and normalizing to an internal standard [30]. This method provides an accurate measure of the absolute quantity of functional group present on gelatin (mmol -R / g gelatin), but does not provide a measure of fractional reaction completeness, or fraction of available sites functionalized. Alternatively, the concentration of the functional group may be normalized to the concentration of lysine or total amines to determine percent functionalization (fractional functionalization) [29]; the amino acid composition of the protein may be determined by sequencing or by reference to the literature [36]. Here, we adopted the latter approach to enable a comparison with the ninhydrin assay. By using literature values rather than sequencing each lot of gelatin, some bias is introduced into the fractional DoF due to slight variations in the amino acid composition (Table 1). Thus, the fractional NMR-DoF reported here may be slightly shifted from their true values.

First, we determined the DoF of six different batches of GelNB by both ninhydrin assay and NMR. Five batches of GelNB were synthesized as described by Mũnoz et al., (2014) [28], using varied feed ratios of the norbornene reagent, carbic anhydride (CA), to yield varying DoFs. The single peak at 6.04 ppm (Fig. 3a,b, “GelNB-CA”) was attributed

to the two identical vinyl protons of norbornene, and is similar to what has been reported previously [42]. Full spectra of all GelNB-CA samples are provided in Fig. S1. To test the versatility of the method, we also synthesized a batch of GelNB-NHS, by using the EDC/NHS conjugation approach described in detail by Hoorick et al., (2018) [29]. For GelNB-NHS, four peaks were observed in 5.8 – 6.3 ppm (Fig. 3a,b) and were attributed to norbornene stereoisomers, confirming previously reported observations [29]. The results of the optimized ninhydrin assay and ^{1}H NMR were linearly correlated with an R^2 of 0.87 (Fig. 3c; Table S1). As the ninhydrin assay detects functionalization only at amines, its close concordance with the NMR data suggested that norbornene functionalization occurred primarily at the amines under these conditions. In the future, 2D NMR could be used to quantify the extent

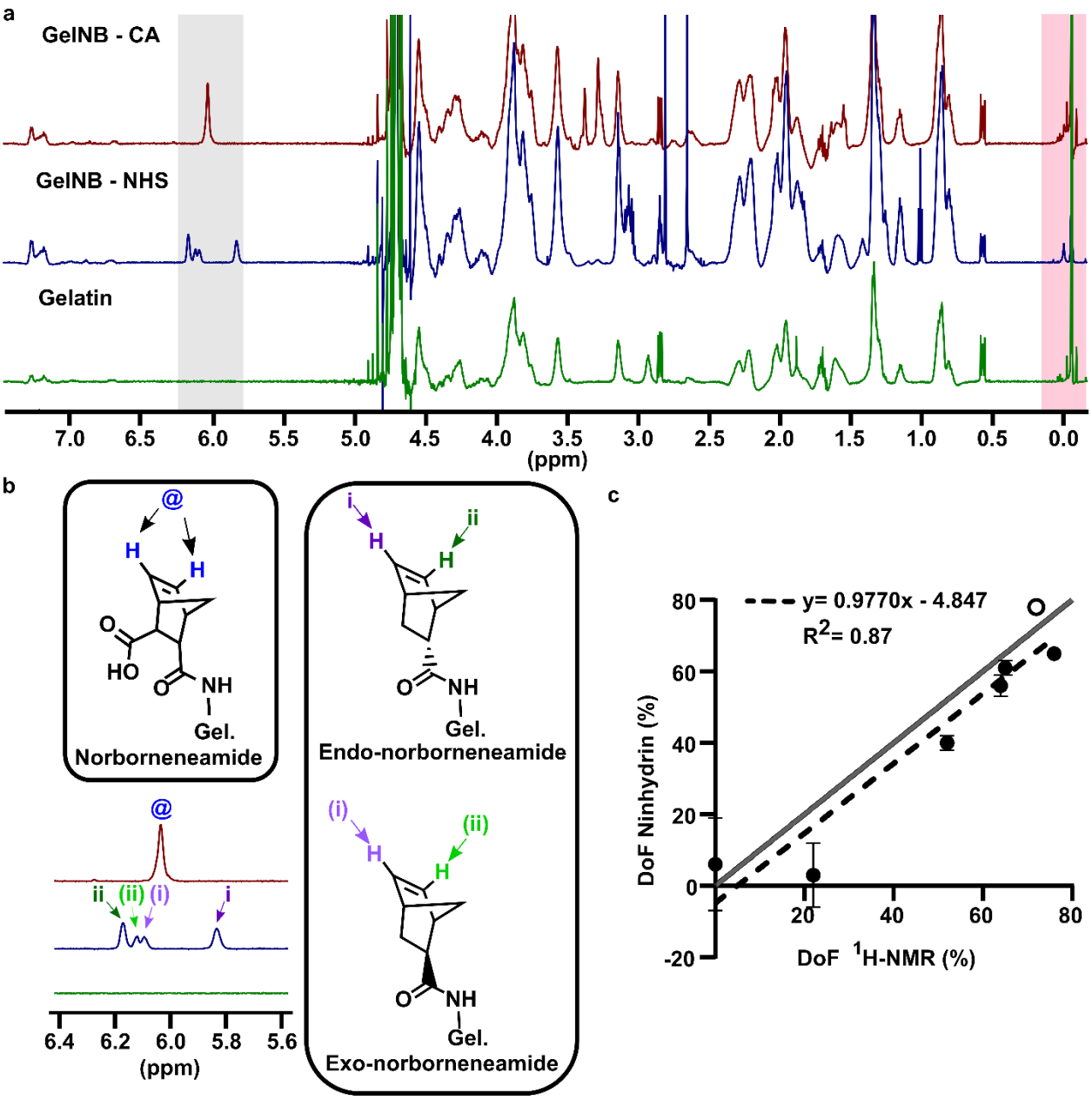

Figure 4-3 Validation of ninhydrin assay versus ^{1}H NMR using GelNB. (a) Full NMR spectra of GelNB synthesized with carbic anhydride (GelNB-CA), GelNB synthesized via NHS conjugation (GelNB-NHS), and non-functionalized gelatin. Integration ranges for the functional group peak and internal standard are highlighted in gray and pink, respectively. (b) Structures and peak assignments for protons in the norbornene functional group in GelNB-CA and GelNB-NHS [29]. (c) Fractional DoF values determined by ^{1}H NMR versus the optimized ninhydrin assay for five GelNB-CA samples (black dots) and one GelNB-NHS sample (open circle). Mean ± std dev of n = 3 technical replicates of ninhydrin assay; some error bars too small to see. Dotted line shows linear regression, y=0.9770x – 4.847, R^2=0.87 Grey line shows the ideal scenario, y=x.

of norborneneamide and possibly norborneneate functionalization under various reaction conditions [30].

Next, we determined the DoF of one batch of GelMA synthesized in-house and three commercial preparations of GelMA, which nominally had DoF of 32 %, 63 %, and 70 % according to the vendor. The peaks for GelMA appeared at the expected chemical shifts for the acrylic groups of methacrylamide and methacrylate [30] (Fig. 4a,b). An upfield peak for the additional proton from methacrylate was not observed in these samples. While the two analysis methods yielded similar results for the medium and high-functionalized commercial GelMA (Fig. 4c) and the GelMA that was synthesized in house, they produced conflicting values for the low- functionalized commercial GelMA. Furthermore, the ninhydrin-DoF and the NMR-DoF each differed oppositely from the nominal, vendor-provided, value (Table S1).

We note that the amine content and species of the original gelatin from which the commercial GelMA was manufactured are unknown. Based on these data, we speculate that the amine concentration may have been lower than the 0.300 mmol/g gelatin that was assumed for this analysis, which would cause the fractional DoF calculated by NMR to underestimate the true value. These results highlight the importance of knowing the amine content of each batch of gelatin when analyzing with NMR. Similarly, the ninhydrin assay was of necessity calibrated using a different lot of gelatin than the commercial GelMA was made from, which could potentially lead to over- or under-estimation of fractional DoF.

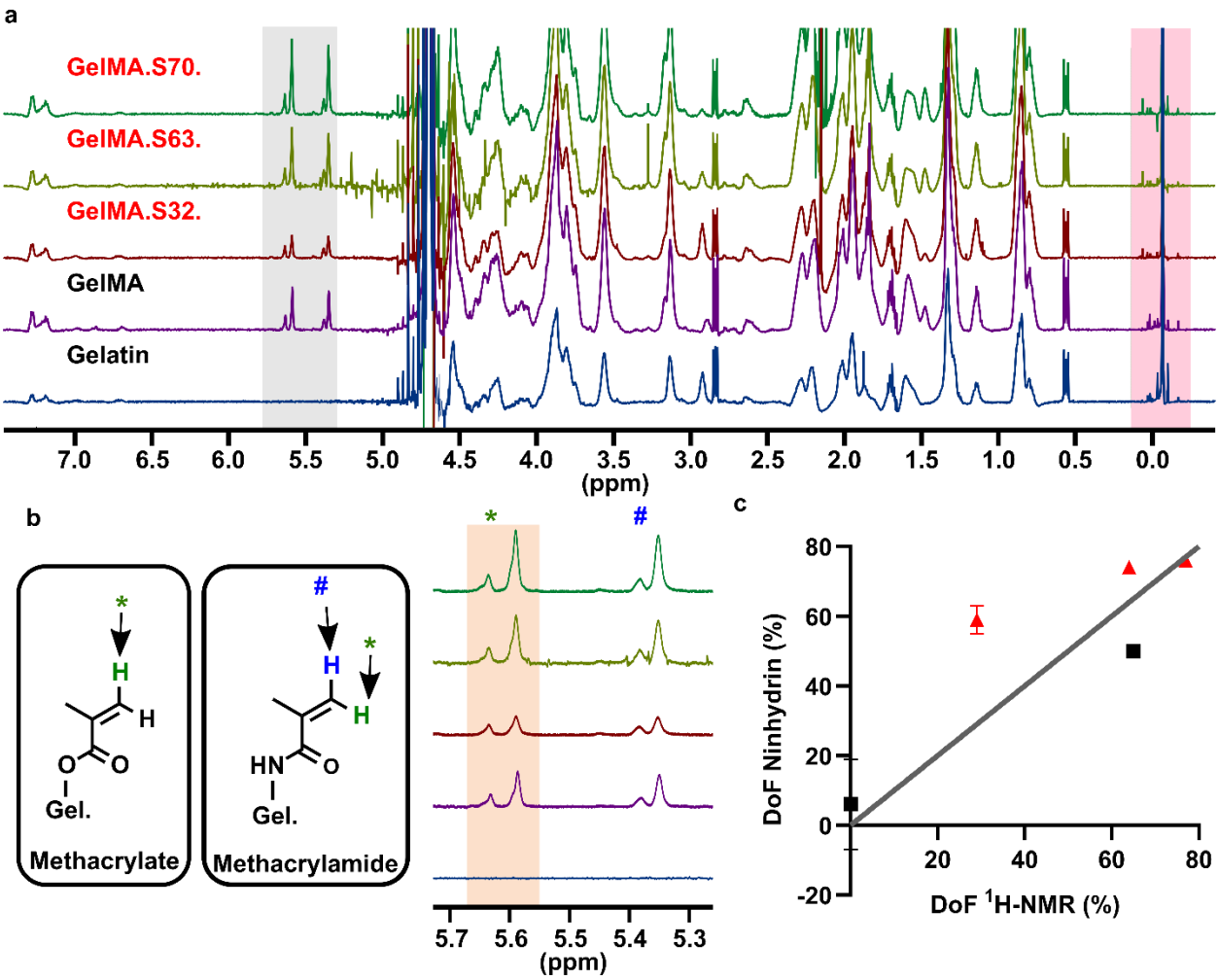

Figure 4-4. Validation of ninhydrin assay versus NMR using GelMA. (a) Full NMR spectra of non-functionalized gelatin and four GelMA samples with varying DoF. GelMA samples S32, S63, & S70 were purchased from Sigma. Integration ranges for the functional group peak and internal standard are shown in gray and pink, respectively. (b) Expanded functional group range displaying methacrylamide and methacrylate structures and peak assignments [30]. One proton of methacrylamide and of methacrylate contributes to the pair of peaks labeled as "*". This pair of peaks was integrated (tan region) for total methacryloylation. Protons from methacrylamide (blue) and modified hydroxyproline (not shown) contribute to the pair of peaks labeled as "#". (c) DoF values determined by ^{1}H NMR versus the optimized ninhydrin assay. Red circles indicate samples from Sigma; black squares indicate samples prepared in house. Mean ± std dev of n = 3 technical replicates of ninhydrin assay; some error bars too small to see. Grey line shows the ideal scenario, y=x.

4.3.3 A comment on absolute versus fractional DoF

When chemically modifying proteins, two complementary metrics describe the extent of functionalization: the quantity of functional group (-R) bound to the protein (mmol -R / g protein; absolute functionalization), and the fraction of available binding sites that were functionalized (fractional or % functionalization). These metrics are used frequently and interchangeably in the literature under the general header DoF, but they provide different information. We briefly discuss each below.

A fractional DoF is essential for assessing reaction completeness while optimizing functionalization conditions. For example, as fractional DoF approaches 100%, no amount of additional reaction optimization will increase the functionalization of the protein; measuring solely the absolute mmol -R / g gelatin would not indicate this so clearly. However, to measure fractional DoF, one must either have an independent measurement of the available reaction sites on the parent protein, or the parent protein must be analyzed in parallel with the functionalized version. To this end, the ninhydrin assay described in this paper allows the user to prepare calibration standards from the parent protein; this strategy normalizes by the available reaction sites between the standards and the sample, producing an accurate fractional DoF value. Such internal normalization is not possible with ^{1}H NMR, as the lysine peak partially overlaps with other peaks in the spectrum, so amino acid analysis or literature estimates must be used. Therefore, the ninhydrin assay may be a simpler strategy for fractional DoF. Of course, the ninhydrin assay is limited to functionalization and conjugation schemes where amines are the primary target.

Absolute functionalization, in mmol -R / g protein, may better correlate with function than fractional functionalization. For example, for GelMA and GelNB, this metric

describes the number of available crosslinking sites per gram of gel and thus correlates with rheological properties [45]. A minimum absolute functionalization may be desired for the material to gel at a desired rate, while over-functionalization may sterically impede physical gelation [45]. This consideration is similar to well established guidelines for protein conjugation in other fields; e.g., antibody conjugation with fluorophores or drugs is usually best limited to a narrow range of label ratios, to optimize the function of the label without obstructing the binding epitope [46,47]. While a ninhydrin assay with a traditional glycine standard curve could quantify absolute DoF by comparing amine content in the parent protein and the derivatized product, this analysis is limited to reactions that occur only at amines. ^{1}H-NMR with an internal standard is best suited to measure absolute DoF, as it quantifies signature functional groups regardless of which combination of amino acids are functionalized [30]. Of course, for protein functionalization, ^{1}H-NMR is limited to functional groups displaying peaks that are not buried within the protein's amino acid peaks (0.5 – 5.0 ppm). For example, it is possible to measure the DoF of thiol-functionalized gelatin with the optimized ninhydrin assay but not with ^{1}H-NMR.

4.4 Conclusion

The ninhydrin assay was optimized for use with protein-based materials to avoid precipitation and generate a quantitative and user-friendly measurement of fractional degree of functionalization. By using a gelatin standard curve, this colorimetric assay provides a fractional DoF without the need for prior knowledge of the amine content of the protein. The optimized assay was fast, inexpensive, and produced results similar to ^{1}H-NMR for both norbornene functionalized gelatin and for most samples of methacryloyl functionalized gelatin. The assay may be suitable for other proteins as

well. Considering the advantages and limitations of available methods for quantifying DoF, we recommend performing ^{1}H-NMR with an internal standard to assess the absolute molar quantity of a functional group and performing the ninhydrin assay to quantify fractional functionalization as an indicator of reaction completeness.

4.5 Method

4.5.1 Reagents and solvents

Ethanol (190 proof) was obtained from Decon Labs, Inc. Phosphate-buffered saline (PBS) was prepared in house by adding 2.7 mM KCl, 13.7 mM NaCl, 10 mM Na_2HPO_4, and 1.8 mM KH_2PO_4 to 18 MΩ Millipore water. Methacrylic anhydride, carbic anhydride, 5-Norbornene-2-carboxylic acid (endo/exo mixture), *N*-hydroxysuccinimide, *N*-(3-Dimethylaminopropyl)-*N*-ethylcarbodiimide (EDC), anhydrous DMSO, ninhydrin, and Sodium trimethylsilylpropanesulfonate (DSS) were obtained from Sigma. Ninhydrin was dissolved in ethanol to the stated concentration and used within two days. DSS was used as the internal standard (δ 0.0 ppm), and D_2O (Cambridge Isotope Laboratories, Inc.) was used as the solvent in ^{1}H-NMR experiments. DSS was dissolved in D_2O to at 0.25 mg/mL to make the internal standard solution.

4.5.2 Functionalization of gelatin

Gelatin from porcine skin, Gel Strength 300, Type A (Sigma-Aldrich) was used as the starting material for all reactions. Gelatin methacroyl (GelMA) was prepared in-house as described by Loessner et al. (2016) [35], including reaction, dialysis, and lyophilization. The ratio of methacrylic anhydride to gelatin was 13 mmol / g. Separately, three samples of GelMA were also purchased from Sigma. The Sigma GelMA was nominally 32 %, 63 %, and 70 % functionalized according to H-NMR validation by the

manufacturer. The methods by which Sigma performed H-NMR analysis were proprietary.

Gelatin norbornene (GelNB) was prepared from gelatin as described by Mũnoz et al. (2014) [28] with the following exceptions: The carbic anhydride (Acros Organics) was varied from 0.4 mM – 3.7 mM to produce GelNB samples having a range of DoFs. Additional sodium hydroxide (50 % w/v) (30 – 50 mL) was needed to reach and maintain the reaction at pH 8 as the concentration of carbic anhydride was increased. The resulting product was centrifuged at 3500 x g for 3 minutes and the supernatant was dialyzed in 4 L of ultrapure water for 10 days at 40 °C with daily water changes before freezing and lyophilization.

One batch of GelNB (GelNB-NHS) was prepared using EDC/NHS conjugation chemistry as described by Hoorick et al., (2018) [29]. Briefly, norbornene carboxylic acid (1.5 equivalents) was dissolved in 500 mL of dry DMSO, followed by the addition of EDC (1 equivalent) and NHS (1.25 equivalents), degassed 3 times and left to react for 24 hours under N_2 conditions. The next day, 10 g of gelatin were dissolved in 150 mL of dry DMSO under N_2 and reflux conditions. Once dissolved, the 5-norborene-2succimidyl ester mixture was transferred into the gelatin flask using a transfer syringe and left to react at 50 °C for 18 hours. The solution was precipitated using 10x excess acetone, then filtered through a Büchner filter. The obtained solids were dried under vacuum for 20 hours. The product was dissolved at 2.5 % in ultrapure water by stirring overnight, pH adjusted to 7 using NaOH, and dialyzed in 4 L of ultrapure water for 24 hours at 40 °C before freezing and lyophilization.

4.5.3 Ninhydrin assay and DoF calculation

Lyophilized gelatin and functionalized GelMA or GelNB samples were each dissolved at 10 mg/mL in 1x PBS. To generate a standard curve, unmodified gelatin was serially-diluted in PBS from 0 - 10 mg/mL in increments of 1 mg/mL in triplicate in a 96-well plate. The functionalized gelatin samples were plated in triplicate without dilution. A 12 mM (2.2 mg/mL) solution of ninhydrin in ethanol was added to each plated sample in a 1:8 v/v ratio of ninhydrin to gelatin solution, unless otherwise noted (total volume 100 µL per well). The plate was sealed with optical sealing tape (ThermoFisher) and incubated in an oven at 70°C until a linear pattern of color development was observed (about 20 to 30 minutes). Absorbance was measured at 570 nm using a multi-modal plate reader (Clariostar). The mean absorbance for each gelatin standard was plotted to form a standard curve.

For each functionalized sample, the fraction of amines available was determined by

$$Fraction\ of\ amines\ available = \frac{Apparent\ sample\ conc.}{Nominal\ sample\ conc.} \quad \textbf{(1)}$$

where the apparent concentration was obtained by comparison to the standard curve, and the nominal concentration was defined as the concentration at which the protein sample solution was prepared. The (percent) DoF was determined by

$$DoF\ (\%) = 100 \times \left(1 - \frac{Apparent\ sample\ conc.}{Nominal\ sample\ conc.}\right) \quad \textbf{(2)}$$

4.5.4 ^{1}H NMR assay and DoF calculation

Quantification of DoF in mmol -R / g gelatin was performed according to the method described by Claaßen et al. [30]. Samples were prepared for ^{1}H-NMR by dissolving lyophilized gelatin, GelMA, or GelNB, in the internal standard solution at 20

mg/mL gelatin. This produced a known DSS to gel ratio of 0.0573 mmol DSS / g gelatin. The ^{1}H-NMR spectra were obtained at room temperature using 5 mm diameter NMR tubes and a standard Bruker Avance III 600 MHz spectrometer for solution samples operated at 14.1 tesla. Spectra were analyzed using Mestranova software (v14.0.0). All spectra were phase adjusted and baseline corrected.

Total degree of norbornene functionalization (mmol NB) of the 5 GelNB samples was assessed by integrating the single peak at 6.0 ppm for 2 protons, corresponding to two vinyl protons of norbornene, and normalizing to the DSS peak (9 protons). The GelNB-NHS sample was assessed by integrating the four peaks appearing from 5.8 – 6.3 ppm for 4 protons, corresponding to 2 vinyl protons of endo-norbornene and 2 vinyl protons of exo-norbornene [29], and normalizing to the DSS peak (9 protons). This value was multiplied by the mmol DSS / g gel ratio to determine DoF in units of (mmol NB / g gelatin). For GelMA, total degree of methacryloylation (mmol MA) was assessed according to the method from Claaßen et al. [30]. Briefly, the two peaks at 5.5 – 5.7 ppm, corresponding to a single acrylic proton of methacrylate and a single acrylic proton of methacrylamide (Fig 4a), were integrated. The sum of both peaks was integrated for 1 proton and normalized to the DSS peak (9 protons) to determine mmol MA. This value was multiplied by the (mmol DSS / g gel) ratio to determine DoF in units of (mmol MA / g gelatin). To estimate the fractional functionalization for comparison to the ninhydrin assay, (mmol -R / g gelatin) was divided by the reported density of amines on gelatin (0.300 mmol amines / g gelatin) (see Table 1) [36].

4.6 References

1. Choi JR, Yong KW, Choi JY, Cowie AC (2019) Recent advances in photo-crosslinkable hydrogels for biomedical applications. BioTechniques 66:40–53

2. Annabi N, Tamayol A, Uquillas JA, Akbari M, Bertassoni LE, Cha C, Camci-Unal G, Dokmeci MR, Peppas NA, Khademhosseini A (2014) 25th Anniversary Article: Rational Design and Applications of Hydrogels in Regenerative Medicine. Adv Mater 26:85–124
3. Ifkovits JL, Burdick JA (2007) Review: Photopolymerizable and Degradable Biomaterials for Tissue Engineering Applications. Tissue Eng 13:2369–2385
4. Li Y, Rodrigues J, Tomás H (2012) Injectable and biodegradable hydrogels: gelation , biodegradation and biomedical applications. Chem Soc Rev 41:2193–2221
5. Yue K, Trujillo-de Santiago G, Alvarez MM, Tamayol A, Annabi N, Khademhosseini A (2015) Synthesis, properties, and biomedical applications of gelatin methacryloyl (GelMA) hydrogels. Biomaterials 73:254–271
6. Mũnoz Z, Shih H, Lin C-C (2014) Gelatin hydrogels formed by orthogonal thiol–norbornene photochemistry for cell encapsulation. Biomater Sci 2:1063–1072
7. Hoorick JV, Gruber P, Markovic M, et al (2018) Highly Reactive Thiol-Norbornene Photo-Click Hydrogels: Toward Improved Processability. Macromol Rapid Commun 39:1800181
8. Claaßen C, Claaßen MH, Truffault V, Sewald L, Tovar GEM, Borchers K, Southan A (2018) Quantification of Substitution of Gelatin Methacryloyl: Best Practice and Current Pitfalls. Biomacromolecules 19:42–52
9. Yue K, Li X, Schrobback K, et al (2017) Structural analysis of photocrosslinkable methacryloyl-modified protein derivatives. Biomaterials 139:163–171
10. Van Den Bulcke AI, Bogdanov B, De Rooze N, Schacht EH, Cornelissen M, Berghmans H (2000) Structural and Rheological Properties of Methacrylamide Modified Gelatin Hydrogels. Biomacromolecules 1:31–38
11. Zhu M, Wang Y, Ferracci G, Zheng J, Cho N-J, Lee BH (2019) Gelatin methacryloyl and its hydrogels with an exceptional degree of controllability and batch-to-batch consistency. Sci Rep 9:1–13
12. Yue K, Trujillo-de Santiago G, Alvarez MM, Tamayol A, Annabi N, Khademhosseini A (2015) Synthesis, properties, and biomedical applications of gelatin methacryloyl (GelMA) hydrogels. Biomaterials 73:254–271
13. Loessner D, Meinert C, Kaemmerer E, Martine LC, Yue K, Levett PA, Klein TJ, Melchels FPW, Khademhosseini A, Hutmacher DW (2016) Functionalization, preparation and use of cell-laden gelatin methacryloyl–based hydrogels as modular tissue culture platforms. Nat Protoc 11:727–746
14. Vlierberghe SV, Fritzinger B, Martins JC, Dubruel P (2010) Hydrogel Network Formation Revised: High-Resolution Magic Angle Spinning Nuclear Magnetic Resonance as a Powerful Tool for Measuring Absolute Hydrogel Cross-Link Efficiencies. Appl Spectrosc 64:1176–1180
15. Hafidz R, Yaakob CM, Amin I, Noorfaizan A (2011) Chemical and functional properties of bovine and porcine skin gelatin. Int Food Res J 18:813–817
16. Karim AA, Bhat R (2009) Fish gelatin: properties, challenges, and prospects as an alternative to mammalian gelatins. Food Hydrocoll 23:563–576
17. Shirahama H, Lee BH, Tan LP, Cho N-J (2016) Precise Tuning of Facile One-Pot Gelatin Methacryloyl (GelMA) Synthesis. Sci Rep 6:1–11

18. Aldana AA, Malatto L, Rehman MAU, Boccaccini AR, Abraham GA (2019) Fabrication of Gelatin Methacrylate (GelMA) Scaffolds with Nano- and Micro-Topographical and Morphological Features. Nanomaterials 9:120
19. Ma Z, Gao C, Gong Y, Shen J (2003) Paraffin spheres as porogen to fabricate poly(L-lactic acid) scaffolds with improved cytocompatibility for cartilage tissue engineering. J Biomed Mater Res B Appl Biomater 67B:610–617
20. Mario Perera M, Ayres N (2017) Gelatin based dynamic hydrogels via thiol–norbornene reactions. Polym Chem 8:6741–6749
21. Friedman M (2004) Applications of the Ninhydrin Reaction for Analysis of Amino Acids, Peptides, and Proteins to Agricultural and Biomedical Sciences. J Agric Food Chem 52:385–406
22. Nayuni NK, Cloutman-Green E, Hollis M, Hartley J, Martin S, Perrett D (2013) Critical evaluation of ninhydrin for monitoring surgical instrument decontamination. J Hosp Infect 84:97–102
23. Sewald L, Claaßen C, Götz T, Claaßen MH, Truffault V, Tovar GEM, Southan A, Borchers K (2018) Beyond the Modification Degree: Impact of Raw Material on Physicochemical Properties of Gelatin Type A and Type B Methacryloyls. Macromol Biosci 18:1800168
24. McCormack T, O'Keeffe G, Craith BM, O'Kennedy R (1996) Assessment of the Effect of Increased Fluorophore Labelling on the Binding Ability of an Antibody. Anal Lett 29:953–968
25. Vira S, Mekhedov E, Humphrey G, Blank PS (2010) Fluorescent-labeled antibodies: Balancing functionality and degree of labeling. Anal Biochem 402:146–150

5. Crosslinking density measurement via H NMR to predict biomaterial stability under physiological fluid flow

5.1 Abstract

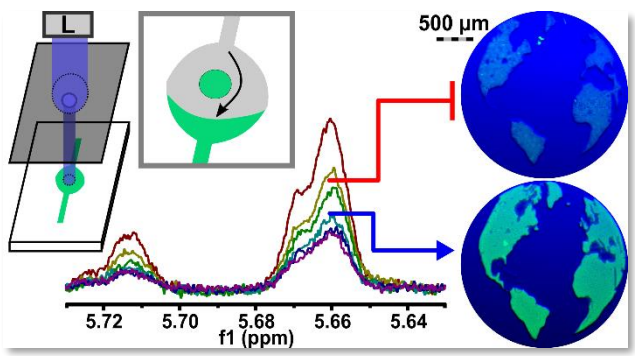

Photocrosslinked hydrogels have become a mainstay in the tissue engineering field, but analytical methods to characterize their reactivity and internal crosslinks are underdeveloped. Additionally, the stability of crosslinked gels under fluid flow is challenging to predict. We optimized an NMR measurement to assess crosslinking density within two classes of photocuring hydrogels, methacryloyl-modified gelatin and a semi-synthetic blend of thiol-modified gelatin and norbornene-terminated polyethylene glycol. The measurement was validated by controlling the polymerization rate with light exposure, and observing predictable changes in crosslinking formation. This technique was then applied to predict material stability under physiological fluid flow. DoC correlated with stability, and more intricate, smaller patterns required a higher DoC for stability. We concluded that DoC is a useful metric for predicting the stability of architecturally complex features when photopatterning.

5.2 Introduction.

Nearly every branch of tissue engineering, spanning from the production of 3D cultured microphysiological models (organs-on-chip) to fabrication of implantable organs, is dependent on well controlled biomaterial chemistry**.** Modern applications require that biomaterials platforms be formed and stable at the desired location and/or time, plus be tunable in terms stiffness, porosity, and chemical content to meet the needs of each particular use case. These properties arise out of the chemistry of the base polymer as well as the chemistry used to cross-link it. Many tissue engineering projects progress sluggishly through early materials- and chemistry-optimization stages to strike a balance between fabricating stable, high-resolution structures and the desired "soft-tissue" characteristics.[1]

An essential criterion for successful use of biomaterials in many microphysiological systems, bioreactors, and implantable materials is stability in the context of warm perfusion. Each of these contexts requires that the material maintain its integrity at physiological temperatures while immersed in culture media or body fluids, either of which may be flowing.[2] A major barrier when applying biomaterials is their unpredictable mechanical stability. That barrier is further heightened by the need to maintain tissue-specific mechanical properties such as stiffness and porosity, which can be in conflict with achieving stability under flow. Therefore, there is a need to precisely tune biomaterials to balance stability under flow and tissue stiffness. Toward this aim, radical-induced polymerization has found widespread use within biomaterials, where the stiffness and stability of the material is tuned by adjusting the crosslinking conditions.

While the tunability of radical-induced polymerization is useful for mimicking tissue stiffness, the methods for measuring the stability of the cured material are lacking. Material stiffness has been linked to stability in air,[3] but it is often improperly interpreted as a proxy for stability in warm, submerged tissue engineering settings.[4] Rather than stiffness, insufficient crosslinking may be correlated with material dissolution. We hypothesized that a method to assess the absolute degree of crosslinking (DoC) would be most predictive of hydrogel stability.

To test this hypothesis, we focused on photocrosslinkable hydrogels, particularly those based on gelatin, which are widely used to produce features of varied sizes within applications such as organs-on-chip, wound-healing applications, and 3D cell-culture.[5–9] When combined with a photointiator such as lithium phenyl-2,4,6-trimethylbenzoylphosphinate (LAP) and exposed to blue or violet light, the reactive pendant groups crosslink (Scheme 1a,b), creating an interconnected polymeric network. These materials readily mimic tissue properties and enable necessary cellular functions, but a major obstacle for progress is their unpredictable stability.[10,11]

Current materials characterization assays do not provide a direct measurement of the extent of crosslinking in photo-crosslinked hydrogels, making it challenging to predict their stability. H NMR and colorimetric methods have been extensively developed for characterizing the absolute methacryloyl- or thiol monomer content[12,13], referred to as the degree of functionalization (DoF). Protein H NMR is well-suited for this analysis because vinyl protons on methacryloyl groups are clearly distinguishable from amino acid protons. Yet, this metric only describes the upper limit of crosslinking, which may be unrelated to the crosslinking density required for a stable material. A major obstacle for using H NMR to assess the degree of crosslinking (DoC) is the decrease in spectral resolution that occurs as the material solidifies[14–17] More importantly, the metrics' usefulness for predicting mechanical stability in the intended environment needs to be investigated.

Herein, we screened various H NMR approaches for assessing absolute DoC and demonstrated that an enzyme digestion following photopolymerization can enable excellent spectral resolution of cured biomaterials. We then used this approach to test the extent to which DoC directly correlates with material stability in photocrosslinked gelatin hydrogels. To demonstrate the versatility of this approach, we performed the same analysis toward a more complex hydrogel blend of thiol-modified gelatin and norbornene-functionalized polyethylene glycol (gelSH-pegNB). Finally, after observing the positive correlation between stability and size,

we demonstrated that a higher DoC threshold must be met for features that are relatively smaller (Scheme 1c,c).

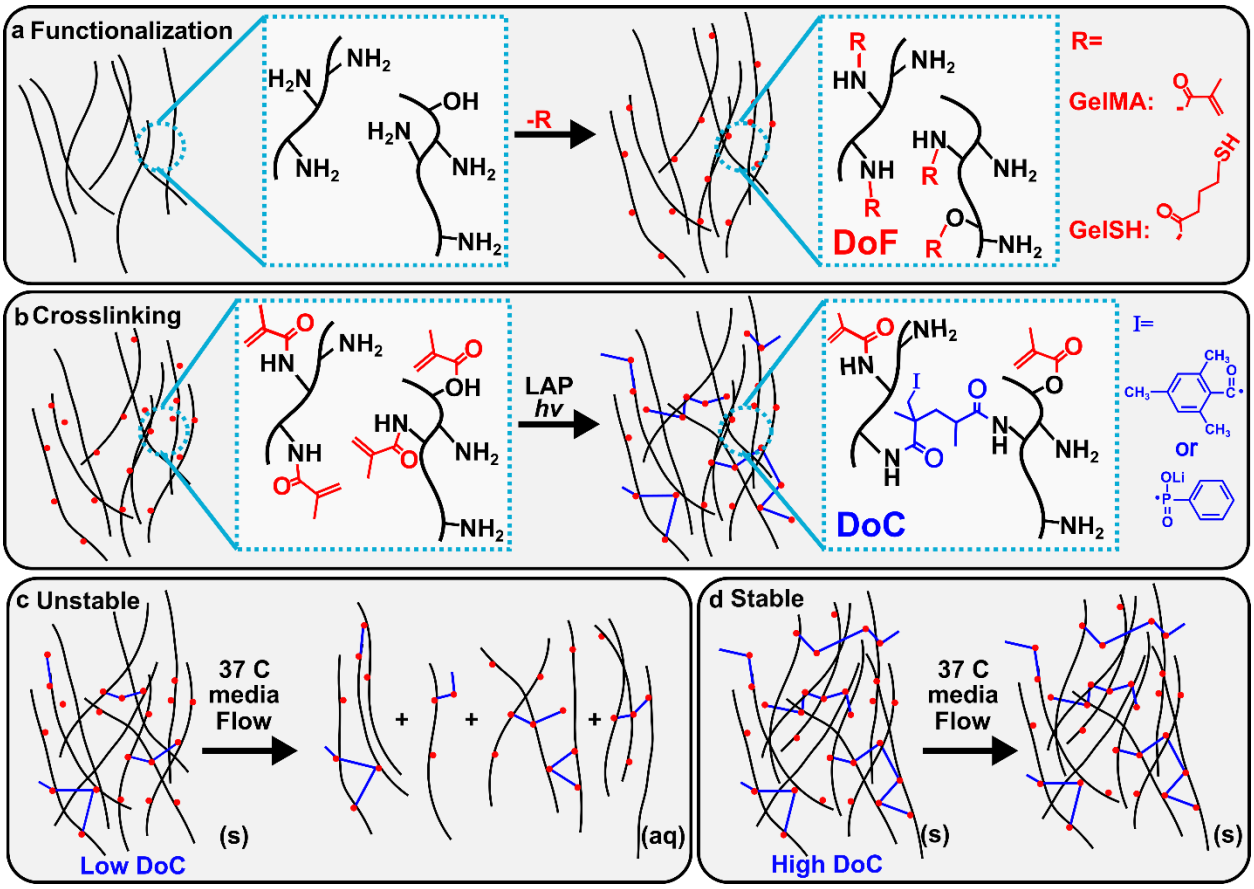

Scheme 5-1. Natural ECM materials are chemically functionalized for photocrosslinking, and may require a minimum crosslinking density to be stable.
(a) Functionalization: Amino and hydroxyl terminated amino acids on gelatin (black lines) are functionalized with methacryloyl (gelMA) or thiol (gelSH) groups. (b) GelMA Crosslinking: Photopolymerization by blue-violet light and a photointiator results in formation of crosslinks and loss of methacryloyl vinyl groups. Bound radicals from the initiator are abbreviated as **I;** growing polymer chains could also bind at that location instead. (c) Instability: An insufficient degree of crosslinking (DoC) may result in material dissolution in presence of warm media flow. (d) Stability: Sufficient crosslinking may result in a stable gel.

5.3 Results.

5.3.1 Digestion of hydrogel provided high-resolution H NMR spectra after photo-crosslinking

Prior studies have demonstrated quantification of crosslinking extents by using magic angle spinning solid-state (MAS) NMR, but this specialized technique may also not provide

sufficient resolution for highly crosslinked gels.[14–17] A development in rheology instrumentation enabled simultaneous stiffness and IR measurements during photocuring, but the low resolution afforded by IR prevented quantification of absolute DoC.[18] These studies collectively drove the field closer to enabling a precise DoC measurement, but there still remains a need to further improve spectral resolution.

We and others have previously described H NMR methods to quantify the number of functional groups on gelatin, or degree of functionalization (DoF), based on the appearance of methacroyl groups (Fig. 1a).[12,13] During crosslinking, those groups are consumed (Scheme 1b), which leads to the loss of signal in the vinyl range and enable quantification of DoC. Indeed, by standard H NMR of the photocrosslinked gel, we observed a decrease in peak height in the vinylic range when gelMA was exposed to 405 nm light for various lengths of time (Fig. 1b). However, we also observed peak broadening that pre-empted quantification, as expected due to loss of molecular motion and increase in intermolecular interactions within the crosslinked hydrogel.[19] Therefore, we screened multiple analysis strategies with the goal of obtaining an H NMR spectrum from the crosslinked gels with sufficient resolution to quantify the vinylic methacryloyl peaks against an internal standard.

We reasoned that one could mitigate the anisotropic interactions present in solids, while retaining the information on the number of functional groups, by selectively digesting the hydrogel at points other than the photocrosslinking site. The enzyme collagenase D cleaves at esters present in the gelatin peptide backbone, but does not cleave remaining methacryloyl pendant groups (Fig 1c).[20] Therefore, we tested the extent to which collagenase digestion would convert the solid cured gel into a liquid without affecting the analysis. We observed narrower peaks than an undigested gel, and a shorter peak height than an unexposed gel (Fig 1d). We compared this method to the gold standard for analysis of solids, magic angle spinning (MAS) H

NMR. Digestion of the gel yielded a sharper peak than MAS NMR, and the peak width was the same as unexposed gelMA (Fig 1d).

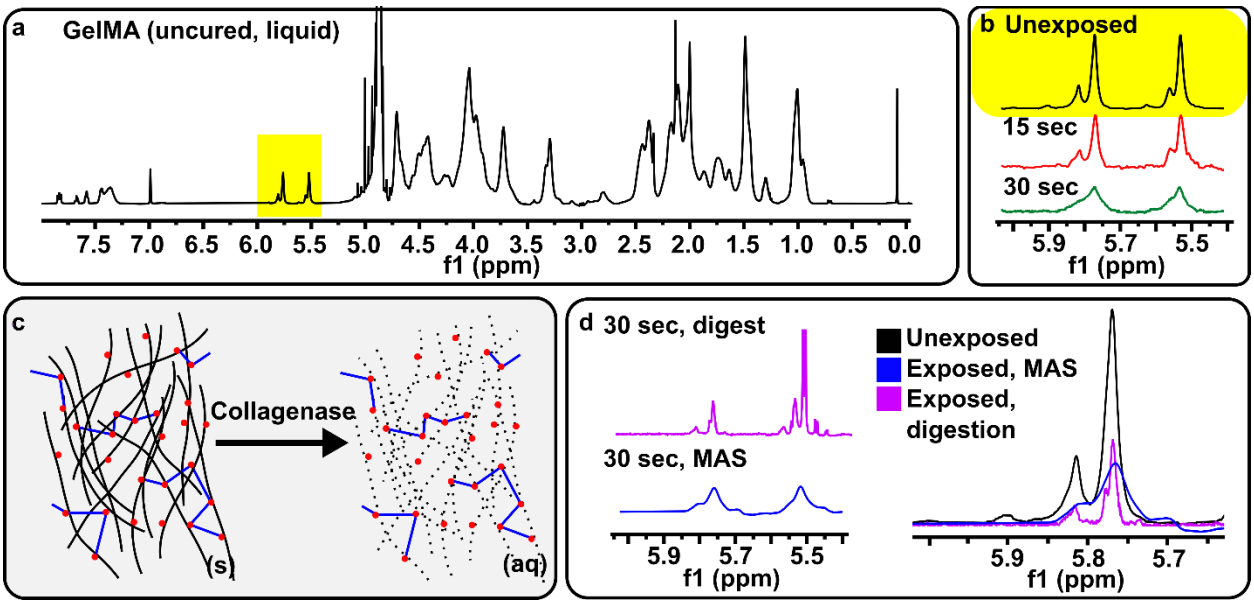

Figure 5-1 Digestion with collagenase D of gels produced quality H NMR spectra.
(a) Full H NMR spectrum of unexposed, liquid methacrylate functionalized gelatin (gelMA). Methacryloyl peaks highlighted in yellow. (b) H NMR spectra of undigested gelMA. unexposed, exposed for 15 seconds (red), and 30 seconds (green). Formation of a solid gel with light exposure caused an increase in anisotropic interactions leading to low resolution H NMR spectra that are insufficient for measuring DoC at higher exposure times. (c) Digestion schematic of cured gel. Collagenase D digested the gelatin backbone, leaving synthetic crosslinks formed during photopolymerization in an aqueous solution. (d) MAS H NMR spectra of unexposed gel (blue) compared to liquid state H NMR following enzyme digestion (magenta). Digestion provides higher resolution peaks in comparison to using MAS H NMR.

5.3.2 Enzyme digestion enabled gelMA photocrosslinking reaction monitoring.

Having shown that digesting an exposed gel improved spectral resolution, we investigated whether digestion would enable monitoring the photocrosslinking reaction of gelMA. To calculate crosslinking density (DoC) for GelMA, we reasoned that we could quantify the loss of apparent DoF to calculate the number of crosslinks formed. We first measured the apparent DoF of the sample by comparing the methacryloyl peak (5.56-5.95 ppm) integral to the internal standard integral, using sodium trimethylsilylpropanesulfonate (DSS) as an internal standard, as previously reported.[13] The unit conversion is shown in Eq. 1.

$$DoF[\frac{mmol\ MA}{g\ gelMA}] = \frac{\int methacryloyl}{\int DSS} \times \frac{9\ DSS\ protons}{1MA\ protons} \times \frac{mmol\ DSS}{g\ gelMA} \quad \text{Eq. 1}$$

DoC was estimated at each timepoint by subtracting the apparent DoF at time *n* (T_n) from the initial DoF (T_0), then dividing by a factor equal to the number of functional groups consumed per crosslink (*f).* For gelMA, we assumed *f*=2, accounting for two methacryloyl groups per GelMA linkage (Eq 2) (Fig. 2c).

$$DoC\,\frac{mmol\ crosslinks}{g\ gelMA} = \frac{1}{f}\left(DoF_{(T_0)} - DoF_{(T_n)}\right) \quad \text{Eq. 2}$$

Similarly, we reasoned that the maximum possible DoC would be reached once every functional group was consumed, which for GelMA would occur if every methacryloyl group reacted with one other (Eq. 3).

$$Max\ DoC = \frac{1}{f}(DoF_{(T_0)}) \quad \text{Eq. 3}$$

We note that the use of *f*=2 for GelMA provides a lower limit of the max DoC, as some crosslinks may include three or more methacrylates due to the chain growth mechanism. We reasoned that the distance between methacrylate functionalizations on the protein would favor dimeric crosslinks over than longer chains.

To test the effectiveness of this approach for calculating DoC, we exposed gelMA with 385 or 405 nm light in five second increments and analyzed the resulting gels after enzymatic digestion. We observed a clear decrease in peak area with exposure time, consistent with a loss of methacryloyl vinyl groups due to covalent bond formation (Fig 2a,b). The DoC vs time conversion resulted in sigmoidal growth curve with a 405 nm exposure, and an accelerated, exponential growth curve from a 385 nm exposure. This was expected as the initiator, LAP has an absorbance maximum at 375 nm (Fig. 2a-c).[21] Interestingly, both conditions levelled off at less than the predicted Max DoC, suggesting steric hindrance from the crosslinks prevented all the methacryloyl groups from reacting.[14]

Finally, as stiffness is often used as a proxy for extent of crosslinking, we tested the extent to which stiffness correlated with DoC as the reaction progressed. We observed that the DoC plateaued within the first 10 – 20 seconds (DoC_{405} t_{90}: 20.0 sec, DoC_{385} t_{90}: 10.8 sec), whereas the stiffness plateaued at least sixty seconds later (S. Mod_{405} t_{90}: 147 sec, S. Mod_{385} t_{90}: 103 sec), for both wavelengths of light (Fig. 2d). The stiffness increased beyond when the methacryloyl peaks disappeared, which we interpreted as a physical gelation process such as phase transition or solvent evaporation.

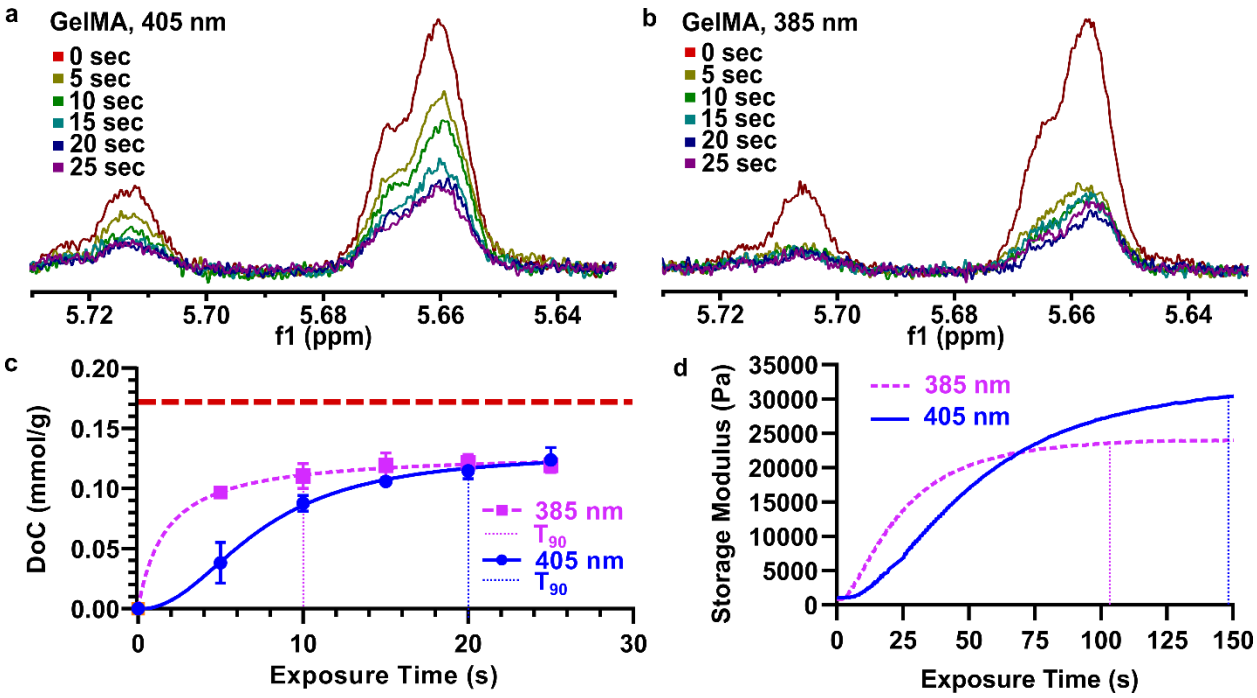

Figure 5-2. Quantification of degree of crosslinking (DoC) in GelMA using collagenase D prior to liquid state H NMR.
(a) H NMR spectra of gelMA exposed to 405 nm 25 mW cm^{-2} light. Digestion with enzyme followed by H NMR enables tracking of DoC with 5 second exposure intervals. Methacrylate peak height decreases visibly over 0 s to 25 s time course. (b) H NMR spectra of gelMA exposed to 385 nm 25 mW cm^{-2} light. Methcrylate peaks decrease faster compared to 405 nm light at the same intensity. (c) Quantification of DoC from spectra shown in Fig. 2a,b. Plot of 10% GelMA DoC (mmol/g) versus exposure time with 405 nm and 385 nm light. Max DoC represented by red line. n=3. (d) Time dependent rheological characterization of gelMA. Plot of gelMA storage modulus (PA) versus exposure time with 405 nm and 385 nm light, 25 mW/cm^2 intensity. Increased rate of crosslinking initially with 385 nm light compared to 405 nm light.

5.3.3 Stability of GelMA features was related sigmoidally to DoC at short photoexposure times.

Next, we tested the relationship between DoC and the physical stability of photocured gels. Knowing that in general, more crosslinking is associated with greater stability, we hypothesized that the relationship could be either linear or sigmoidal. To test this hypothesis, we challenged regions of photocrosslinked gels with conditions of steady-state flow at physiological temperature, as is found in many organ-on-chip experiments.

Freestanding islands of gel were photopatterned inside a simple microfluidic flow cell (Fig 3a), following procedures previously described by us and others.[6,22] The chip was filled with fluorescently labeled precursor solution, a photomask laid over the chip, and then the gel was exposed through a 800 μm diameter pinhole. This strategy allowed us to easily evaluate multiple exposure times on a single chip by exposing one region, re-positioning the mask, re-exposing, and so on. After exposure of four regions (e.g. for 2, 4, 6, and 8 seconds), the uncrosslinked gel was rinsed away (Fig. 3b). Finally, the chips were perfused with warm PBS for two hours.

Under these conditions, both fluorescent intensity as well as the % stable area of the gel increased with exposure time (Fig. 3c-e). GelMA areas that were photo-exposed for at least 6 seconds were stable, and areas exposed for 2 seconds were nearly always unstable and washed away completely (Fig. 3c). The 4-second exposure was semi-stable, as some fraction of the pattern was always present after rinsing, but it was never complete. Tto account for the increased shear stress on patterns closer to the inlet of the flow cell, we also rotated the exposure order and observed no difference in stability.

When plotted against DoC obtained from NMR measurements at the same exposure times (from Figure 2), both fluorescent intensity and % stable area were well fit by a sigmoidal curve with a DoC at half-max of 0.060 mmol/g (Fig 3f). This result suggested that physical

stability of the photocrosslinked gel patterns required that the crosslinking density surpass a critical DoC threshold (Fig 3f).

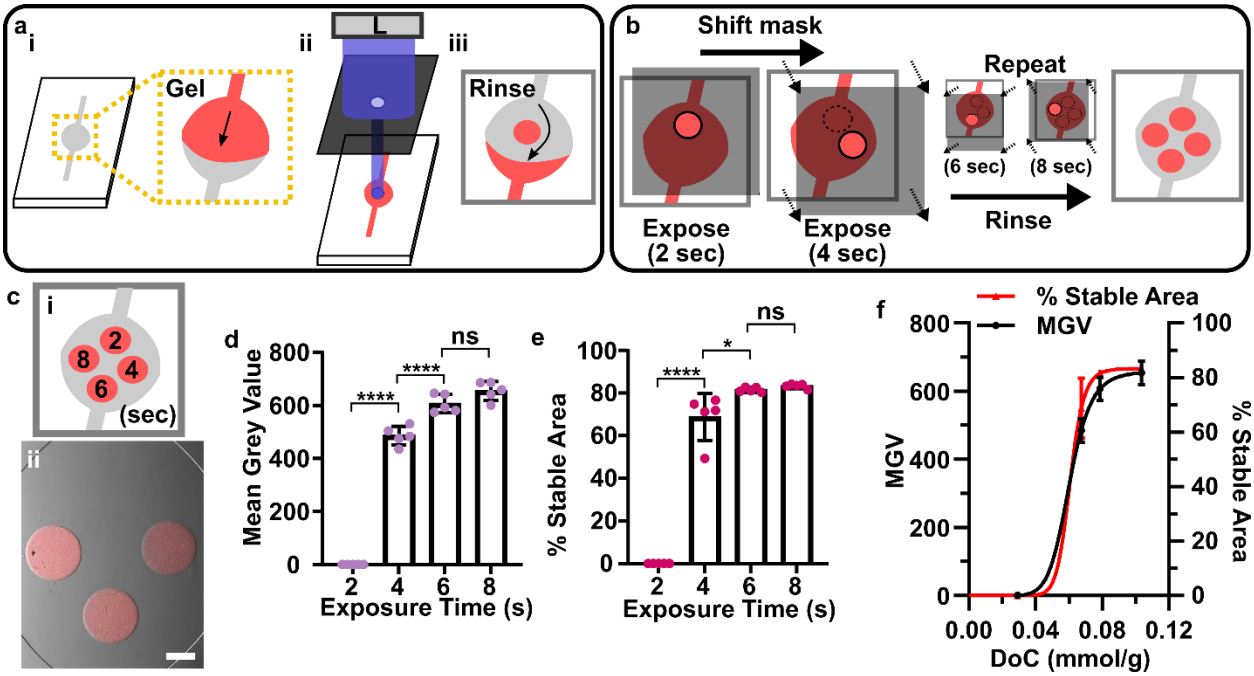

Figure 5-3 GelMA patterning stability under physiological fluid flow correlates with DoC. (a) Schematic of *in situ* photopatterning process[6] (i) Chip filled with gel precursor. (ii) Photomask aligned with chip, clamped (not shown for clarity), and exposed. (iii) Unexposed gel precursor rinsed away with PBS. (b) Schematic of creating a pattern to test multiple exposure points on a single chip by shifting the photomask and preforming sequential exposures. (c) Circular 10% gelMA features stained with NHS rhodamine on a chip exposed at differing time points with 385 nm 25 mW cm^{-2}. (i) Position of each exposure time point. (ii) Composite (fluorescence overlayed over brightfield) microscope image of chip following PBS rinse (10 min, 5 µL/min, 50 µL) and physiological fluid flow (2 hours, 5 µL/min, 600 µL). Scale bar = 500 µm. (d) Quantification of fluorescence intensity (measured in mean grey value) of circular gelMA features from Fig. 3c. (e) Quantification of % stable area of circles, defined as the area of the resulting pattern divided by the area of feature in the photomask. (f) Plot of mean grey value and % stability versus DoC (mmol/g) of GelMA features. Data fit to a sigmoidal curve. n=5 chips. Statistical analysis performed by ordinary one-way ANOVA.

DoC measurement related exponentially to a hydrogel with a step-growth crosslinking mechaniam.

To determine the extent to which the sigmoidal relationship between DoC and stability was generalizable to other crosslinking mechanisms, we assessed the same metrics using a semi-synthetic polymer blend composed of thiol-modified gelatin and an 8-arm norbornene-functionalized PEG linker (gelSH-pegNB). (Fig. 4a). This hydrogel formula was chosen because

of the recent widespread use of thiol-norbornene hydrogels and their compatibility with *in situ* photopatterning,[6,9,23] as well as its different crosslinking mechanism. Unlike gelMA, which crosslinks via a chain-growth mechanism, gelSH-pegNB crosslinks via step-growth mechanism.

Using enzymatic digestion prior to H NMR, the decrease in peak area of the vinyl norbornene protons upon photocrosslinking was easily observable (Fig. 4b).[13,23] We calculated DoC as described above (Fig 4c), using *n*=1 because we assumed each crosslink was between a single NB and SH (Eq. 3). For calculating DoF of the gelSH-pegNB, the ratio of NB protons per DSS protons is 2:9.

$$DoF[\frac{mmol\ NB}{g\ gelSH-pegNB}] = \frac{\int NB}{\int DSS} \times \frac{9\ DSS\ protons}{2NB\ protons} \times \frac{mmol\ DSS}{g\ gelSH-pegNB} \quad \textbf{Eq. 4}$$

Interestingly, unlike GelMA, the gelSH-pegNB hydrogel did reach the DoC max, which can be seen in the spectra (5.98 to 6.25 ppm), where peak-heights from exposures beyond 8 sec meet the baseline (Fig. 4b,c). We speculate that steric hindrance may have prevented some of the -MA groups from crosslinking, whereas the step-growth SH-NB linkages were able to fully consume all or nearly all of the norbornene groups.

To determine if DoC was related to stability, we then performed *in situ* photopatterning with gelSH-pegNB using the same mask-based lithography approach as above (Fig. 4d), crosslinking the gel using 405 nm light. Both the fluorescence intensity and % stable area increased sigmoidally with exposure time (Fig. 4e,f). Unlike gelMA, where fluorescence intensity and stable area leveled off together, the gelSH-pegNB intensity continued to increase exponentially after a stable gel was formed, resulting in an exponential trend (Fig. 4g). We speculate this means NMR measurement specifically showed the loss of norbornene groups as they became radicals. Conversion from radicals to thiol-norbornene crosslinks may occur after the NB peaks disappear (Fig 2c,d).

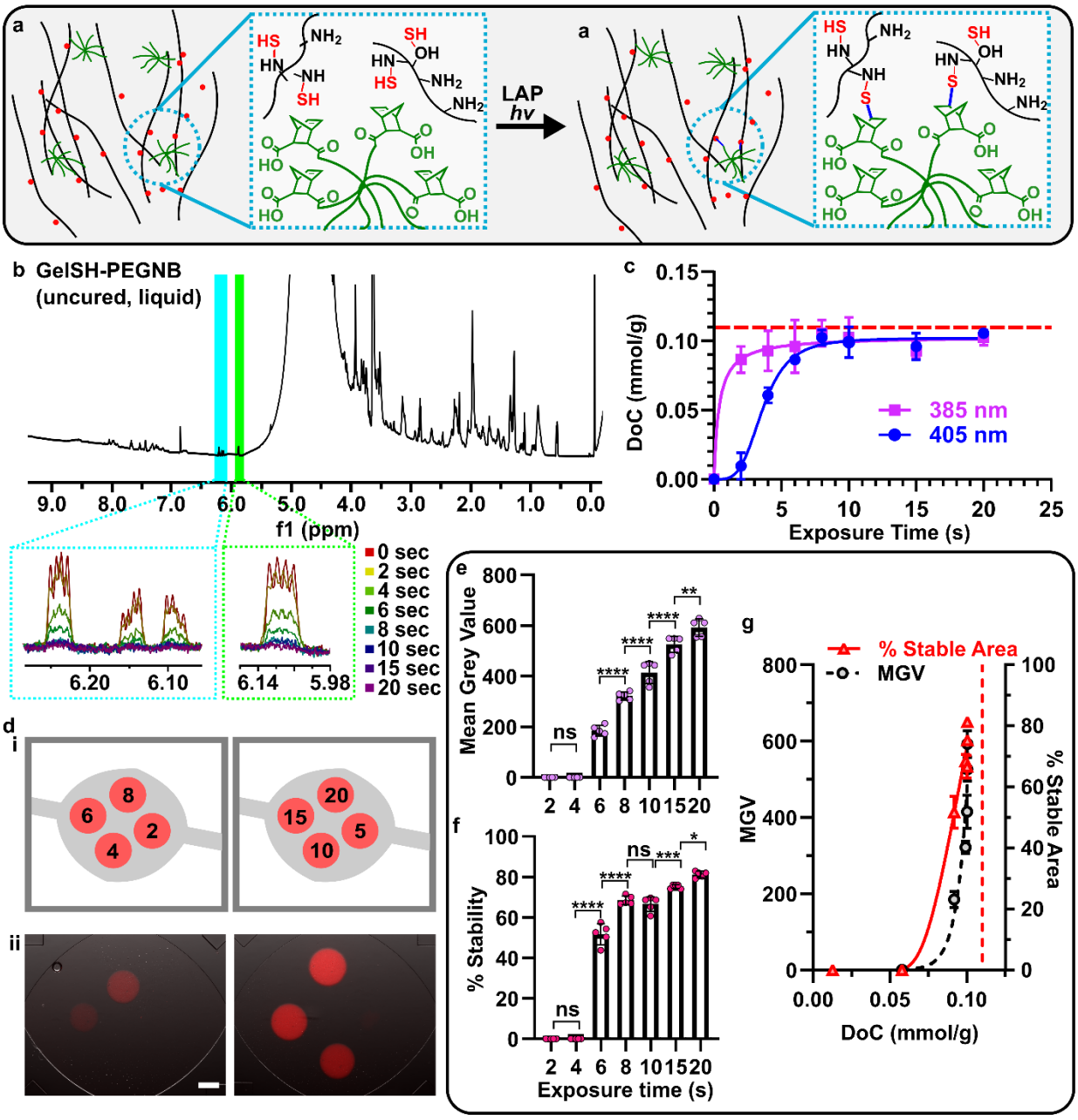

Figure 5-4 Versatility of the method demonstrated through gelSH with a 20 kDa 8-arm PEG-NB linker.

(a) Schematic illustrating semi-synthetic hydrogel blend, gelSH 8-arm PEG-NB, crosslinking reaction. (b) Full H NMR spectrum of uncured, unexposed gelSH-pegNB. NB peaks highlighted in blue and green, decreasing in height as exposure time increases. (c) Quantification of DoC from spectra shown in Fig. 4b. versus exposure time with 405 nm and 385 nm light. Increased rate of crosslinking initially with 385 nm light compared to 405 nm light. Max DoC represented by red line. (d) Circular 5% gelSH 10 mM PEG-NB features stained with NHS rhodamine on a chip exposed at differing time points with 405 nm light. (i) Position of each exposure time point. (ii) Composite (fluorescence overlaid over brightfield) microscope image of chip following PBS rinse (10 mins, 5 µL/min, 50 µL) and physiological fluid flow (2 hours, 5 µL/min, 600 µL). Scale

bar = 500 µm (e) Quantification of fluorescence intensity (measured in mean grey value) of circular gelSH features from Fig 4d. (f) Quantification of % stable area (area of circular feature/area of circular photomask) of circular gelSH features from Fig 4d. (g) Plot of MGV and % stable area versus DoC (mmol/g) of gelSH features. Red dotted line indicates DoC_{max}. n= 5 chips. Statistical analysis performed by ordinary one-way ANOVA.

5.3.4 Higher DoC is required to stabilize smaller features.

Given the need for producing gel features of various sizes, and our prior observations that smaller gels are generally less stable than larger ones[6], we investigated the relationship between DoC and feature size. Toward this, we hypothesized that smaller patterned features, which would be more susceptible to erosion from fluid flow, would require a higher DoC for stability than a larger patterned feature. We tested this by photopatterning gelSH-pegNB through a size-array photomask with varied exposure times, followed by perfusion for two hours with warm PBS. The mask was comprised of three circles that were 200, 400, and 600 µm diameter (Fig 5a), in triplicate. We combined these results with the 800 µm diameter patterns produced in Fig 4d.

At each exposure time, % stable area was dependent on feature size (Fig. 5b.) The minimum DoC for a 35% stable feature was inversely proportional to feature size (400 µm: $DoC_{35\%}$=0.099, 600 µm: $DoC_{35\%}$=0.091, 800 µm: $DoC_{35\%}$=0.086 mmol-crosslinks/g gel) (Fig. 5c). This relationship suggested that smaller hydrogel features are more susceptible to erosion due to fluid flow than larger features, and required more crosslinks to become stable. At each exposure time, the MGV was largely independent of feature size (Fig. 5d,e), This uniform brightness among feature sizes suggests that, while gel features were eroding at the edges, the thickness of the gels remained the same regardless of their size.

Together, these data supported our hypothesis. We concluded that a higher DoC is required for smaller, free-standing features to resist eroding at the edges under flow.

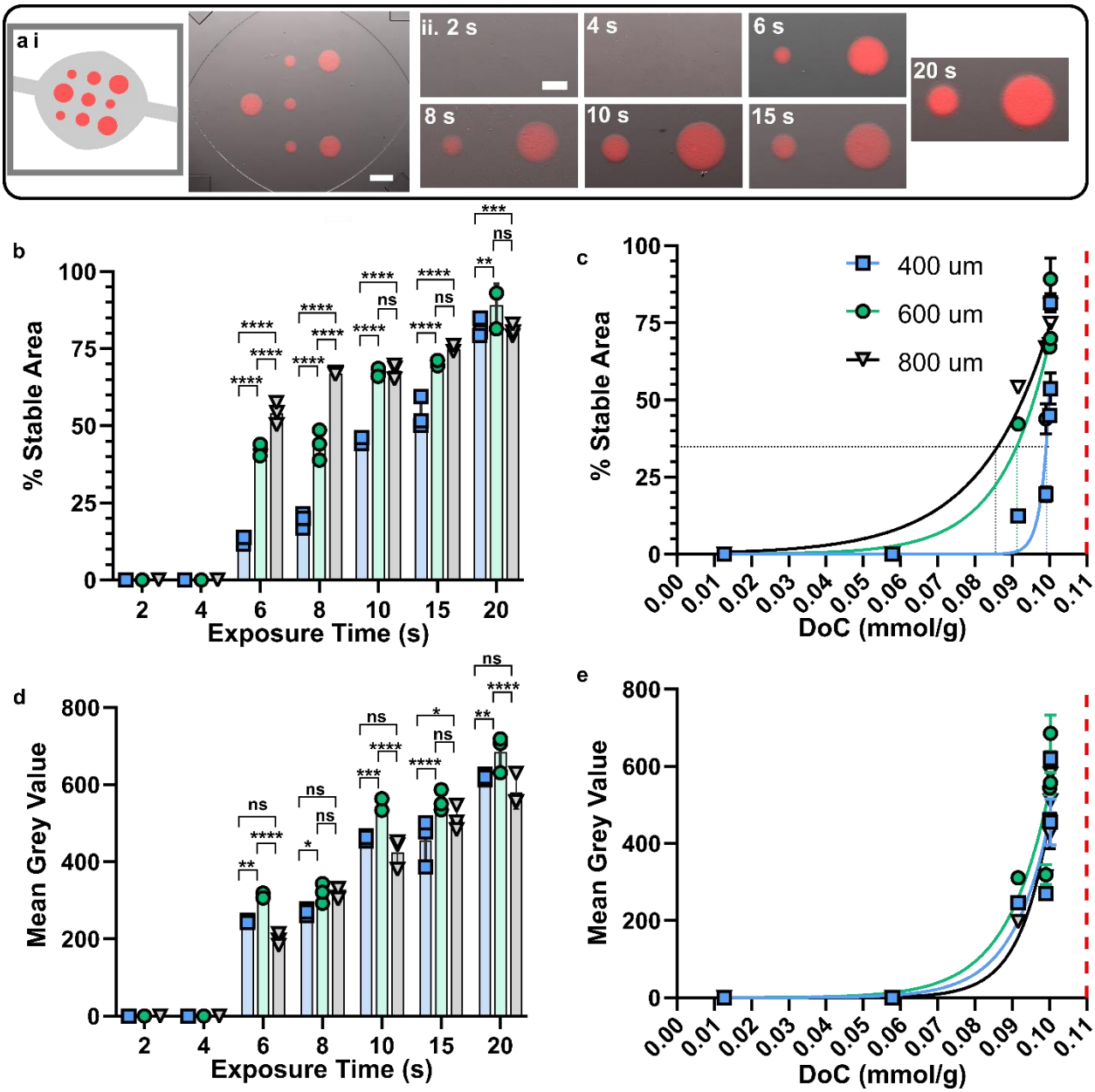

Figure 5-5 The stability of photopatterned features was related to DoC and size.
(a) (i) Schematic and (ii) Image of 5% GelSH with 20 kDa 8-arm PEG-NB photopatterned as an array of 200, 400, and 600 µm circles with 405 nm light 25 mW cm^{-2} intensity at varying time points. Scale bar = 500 µm. (iii) Zoom on 400 and 600 µm patterns for each timepoint. Scale bar = 250 µm. (b) Quantification of % stable area (area of circular feature/area of circular photomask) of circular gelSH features from Fig. 4d and 5a. (c) Plot of % stability versus DoC (mmol/g) of gelSH features. 35% stability represented by black, green, and light blue dotted lines. Max DoC represented by red line. (d) Quantification of fluorescence intensity (measured in mean grey value) of circular gelSH features from Fig. 4d and 5a. (e) Plot of mean grey value versus DoC (mmol/g) of gelSH features. n= 5 chips. Statistical analysis performed by ordinary one-way ANOVA.

5.3.5 The stability of photopatterned features with complex architecture was predicted using DoC.

Finally, we tested the extent to which the concept of a size-dependent critical DoC could be applied to predict the cross-linking conditions required for complex features. We selected a pattern having features of various size and connectivity to neighboring structures: the Atlantic face of Earth (Fig. 6a-e). This intricate pattern was exposed and then perfused for two hours as in prior experiments. We hypothesized that the relationship we observed between DoC and feature size (Fig. 5c) could be used to predict the DoC at which various island features would become stable. For example, we predicted that a larger island such as Greenland, would have become stable ($DoC_{35\%}$) at 0.09 mmol-crosslinks / g gel, and a smaller island such as Panama would have a $DoC_{35\%}$ at 0.10 mmol / g.

To test this hypothesis, we measured the % stability of various Earth features, and then overlaid those values on the growth curves from Fig. 5c. Overall, we observed that % stability of island features generally trended as expected relative to the 400, 600, and 800 μm patterned features (Fig 6f), which supported our hypothesis. We saw that the larger continents (Asia, Africa, North and South America) were crosslinked sufficiently to resist flow at 0.08 mmol crosslinks/g gel (Fig. 6b). Slightly smaller features like Greenland and Spain were stable at 0.09 mmol crosslinks/g gel (Fig. 6c). Isle nations like Great Britian and the Caribbean islands, as well as land that directly obstructed flow paths, such as Panama, were not sufficiently crosslinked to resist flow until 0.10 mmol crosslinks/g gel were formed (Fig. 6d). South America was unexpectedly more stable at lower DoC than the larger 800 and 600 um features, and we speculate that this resulted from it being shielded from the force of perfusion by other surrounding features.

Next, to assess whether diffusion or fluid flow was the dominate cause of instability, we characterized the relationship between features size and the $DoC_{35\%}$. We saw that features up to 200,000 μm^2 were best fit to an exponential growth curve, and features above 200,000 μm^2

were best fit to an exponential plateau curve (Fig. 6g). Using those exponential fits from Fig 6g, we plotted the $DoC_{35\%}$ for each feature. We hypothesized that, if diffusion was impacting stability in addition to fluid flow, it would be noticeable in smaller feature sizes, resulting in an exponential dissociation relationship. If diffusion did not impact stability, we should see an linear inverse relationship between feature size and $DoC_{35\%}$. We observed a linear relationship (Fig. 6h), and concluded that diffusion of uncrosslinked polymer did not have a significant effect on instability.

Additionally, we demonstrated that the critical DoC for stability was independent of wavelength, as we used the features patterned with 405 nm light (Fig 5) to predict island features patterned with 385 nm light (Fig 6). DoC was predictive of pattern stability when feature size was accounted for. We conclude from this that crosslinking density is a useful metric for producing patterns having complex features of varied size and flow paths.

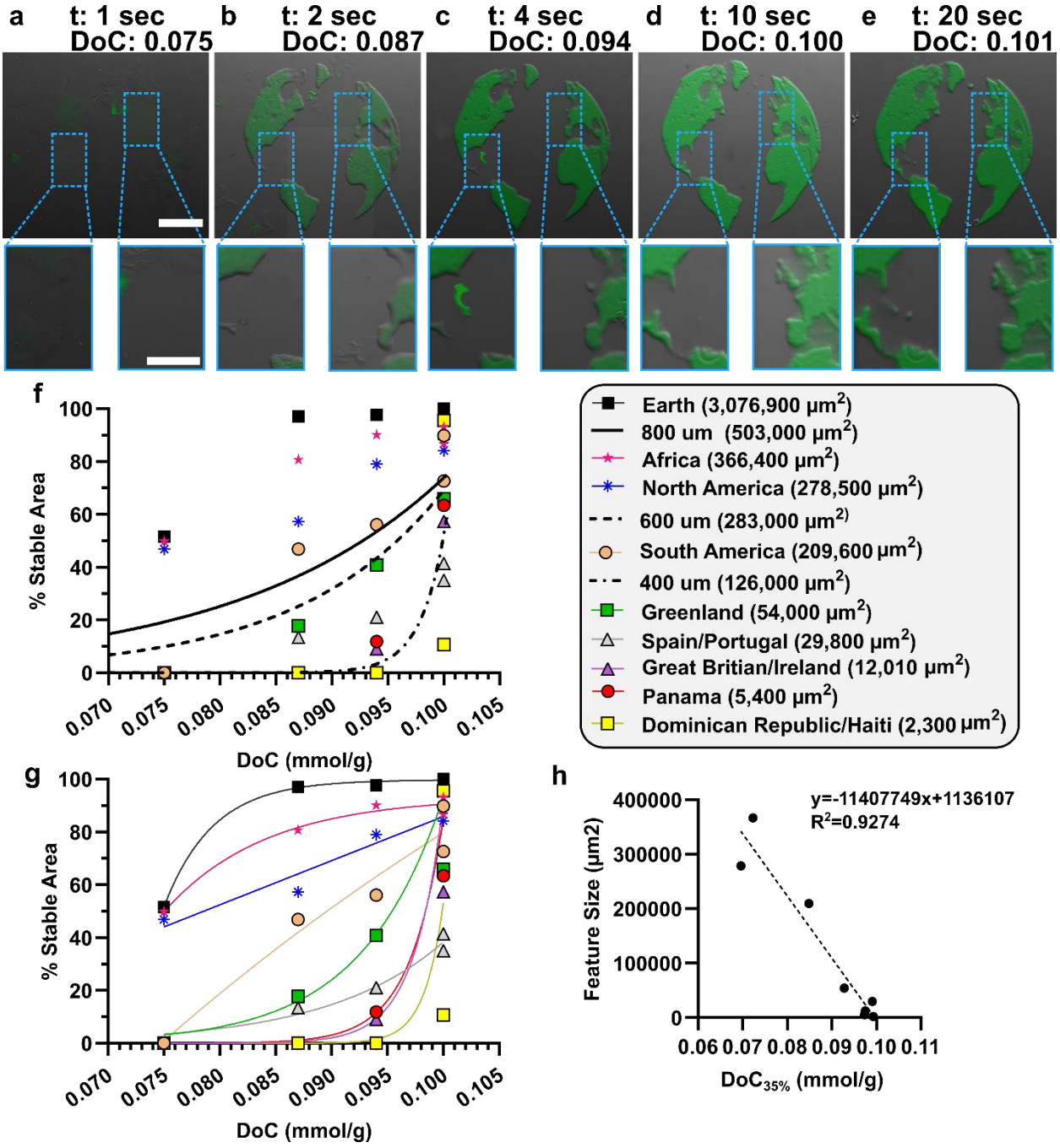

Figure 5-6 The stability of complex features was predicted using DoC and size. GelSH-pegNB was exposed with 385 nm light 25 mW cm^{-2} intensity through a photomask of the Earth.
(a-e) Composite fluorescence microscopy images of gelSH-pegNB features following exposure through an Earth photomask at various doses. The corresponding DoC values (± 0.01 mmol-bonds/g gel) are shown in the top right of each image. Scale bar is 500 µm. Blue squares show zoomed in views of island features, with scale bar of 250 µm. (f) Plot of DoC vs % Stable area for Earth continents and islands. 400, 600, and 800 µm features from Fig 5e were used as standards to predict the stability of island features. (g) Plot of DoC vs % Stable area for the same features, fitted with exponential growth or plateau curves. (h) Plot of $DoC_{35\%}$ vs feature size, determined from exponential curves shown in (g).

5.4 Conclusion

In summary, we optimized an NMR measurement to directly quantify crosslinking density within photocrosslinking hydrogels for the first time. By digesting the crosslinked gels with collagenase, we achieved higher resolution than solid-state MAS NMR. When performing *in situ* photopatterning with both gelMA and gelSH-pegNB hydrogels, we observed that pattern stability was correlated with DoC. To further our understanding of DoC and gel stability, we demonstrated that smaller photopatterned features require higher DoC to resist erosion in solution. Finally, we used the DoC analysis to enable efficient prediction of patterning conditions for a feature with complex shapes and flow paths. Thus, these findings support the hypothesis that absolute DoC quantification is useful for predicting the stability of photopatterned hydrogel features. We anticipate this analysis will be useful for biofabrication techniques that require soft materials to meet architecturally demanding designs, such as photopatterning and bioprinting.

5.5 Methods

Hydrogels Material and preparation

The hydrogel formulas used herein were the same as described previously.[6] Briefly, precursor was prepared by combining 60% functionalized gelatin methacryloyl (bloom 300, Sigma Aldrich Lot: MKCQ6360) and the photoinitiator, Lithium phenyl-2,4,6-trimethylbenzoylphosphinate (LAP, Sigma Aldrich), to a final concentration of 10% w/v gel and 0.01% w/v LAP. Thiol-modified gelatin and PEG-norbornene hydrogel precursor was prepared by combining thiol-modified gelatin (Sigma Aldrich, Lot: MKCJ5413, 0.223 mmol –SH/g gelatin) with 8-arm PEG-NB 20 kDa (Creative PegWorks) and LAP for a final concentration of 5% w/v gelSH, 10 mM PEG-NB and 0.01% w/v LAP.

For H NMR analysis, the internal standard, sodium trimethylsilylpropanesulfonate (DSS, Sigma Aldrich) was added at 0.15 mM concentration and the precursor solvent was D_2O. For *in situ* photopatterning the precursor solvent was phosphate buffered saline (PBS, gibco). After

combining hydrogel ingredients, the gel solution was incubated at 40 C for two hours and then used within a day. All other chemicals were provided by Thermofisher.

Photopolymerization and H NMR measurements

Enzyme digestion method

Precursor was polymerized in a 12 well plate by exposing at 405 or 385 nm collimated LEDs wavelegnths at 25 mW/cm^2 for various times. Specifically, a Prizmatix LED (UHP-F-405 or UHP-F-385) fitted with liquid light guide and 90° reflector attachment with collimating optics was aligned to expose an area the size of a typical 12.7x8.5 cm microwell plate. Following exposure, 0.3 mL of 0.7 mg/mL collagenase D and 5.5 mg/mL $CaCl_2$ solution (Sigma Aldrich) was added to each well, then incubated at 37 C for at least 12 hr. Following the digestion, the solution was analyzed with a Bruker Avance III 800mHz instrument. Total volume of solution was 600 uL. Methacrylate peaks were resolved with 8 scans. Norbornene peaks were resolved with 32 scans. Samples that were analyzed without digesting were exposed within the transparent, glass NMR sample tube.

Solid-state MAS NMR

Precursor solution was added to the rotor, and the uncapped rotor was placed upright underneath the LED light path. After, the rotor was capped and spectra was obtained immediately. The spectrum was obtained using a 500 MHz solid-state NMR spectrometer.

Spectral processing

Mestranova (v14.3.0-30573) was used to analyze all spectra. Baseline correction was performed using polynomial correction. Baseline correction was performed using polynomial correction. Zero (ph0) and first-order (ph1) phase correction was used to minimize phase error. The internal standard was identified and set to 0 ppm. Methacryloyl peaks were identified and integrated at 5.62 to 5.72 ppm, or norbornene peaks were integrated at 5.92 to 5.95 ppm and 6.17 to 6.27 ppm and added together to give final norbornene peak area.

Rheological characterization

Rheological characterization was performed on a MCT302 Anton Parr Rheometer. Thirty µL of Precursor solution was pipetted onto a light-transmitting stage and the LEDs (described above) were positioned underneath the stage. Hydrogel storage modulus was measured by equipping the stage with a 20 mm parallel plate and using time sweep mode at 5% strain with a 0.1 mm gap and 1 Hz frequency. Baseline shear storage modulus as measured, followed by irradiation at 25 mW/cm^2.

In situ photopatterning

In situ photopatterning was performed exactly as described in our previous work,[6] with one key exception. When assessing pattern stability by shifting the photomask on chip to test multiple timepoints, the photomask was shifted prior to each sequential exposure, then uncrosslinked gel was rinsed out after all four patterns were produced. Photomasks for preparing master molds and *in situ* photopatterning were drawn in AutoCAD LT 2019 and printed by ArtNet Pro Inc at 20,000 DPI.

Microscopy

Microscopic imaging was performed using an upright Zeiss AxioZoom microscope equipped with an Axiocam 506 mono camera, HXP 200C metal halide lamp, and PlanNeoFluor Z 1× objective (0.25 NA, FWD 56 mm). NHS-rhodamine fluorescence microscopy was performed using Zeiss Filter Set 43 HE (Ex: 550/25, Em: 605/70). Brightfield images were collected using transmitted light. Zen Blue software was used for image collection, and images were analyzed in ImageJ v1.53t.

Image analysis

To detect patterns, a threshold was set and fluorescence channel images were converted to binary. The particle detection tool was used to detect and outline NHS rhodamine-labeled patterned features. This was then used to assess both mean fluorescence and size of

the patterned features. % fractional area was determined by dividing the measured area of the pattern by the area of the pattern in the photomask.

Statistical analysis

Data was prepared and statistical analysis was performed using GraphPad Prism 8.4.2.

Author contributions

JMZ, ILL, and RRP designed the study, and assessed the findings, and drafted the manuscript.

Declaration of competing interest

The authors declare that they have no known competing financial interests or personal relationships that could have appeared to influence the work reported in this paper.

Acknowledgements

This work was supported by funding from the NIH (U01). JMZ was supported by the NSF GRFP. JMZ and IIL were supported by the UVa DoubleHoo. IIL was supported through the UVa Chemistry Summer Fellowship. This work utilized the UVa Biomolecular Magnetic Resonance Facility which is supported by the University of Virginia School of Medicine, Research Resource Identifiers (RRID): SCR_018736. Thank you to Dr. Steven Caliari for graciously allowing us to perform rheological characterization of gelMA within your space. We thank Jan-Willem Lamberink-Ilupeju, PhD, (Western University) for helpful discussions about GelMA crosslinking mechanisms.

5.6 References

(1) Gao, G.; Kim, B. S.; Jang, J.; Cho, D.-W. Recent Strategies in Extrusion-Based Three-Dimensional Cell Printing toward Organ Biofabrication. *ACS Biomater. Sci. Eng.* **2019**, *5* (3), 1150–1169. https://doi.org/10.1021/acsbiomaterials.8b00691.

(2) Swartz, M. A.; Fleury, M. E. Interstitial Flow and Its Effects in Soft Tissues. *Annu. Rev. Biomed. Eng.* **2007**, *9* (1), 229–256. https://doi.org/10.1146/annurev.bioeng.9.060906.151850.

(3) Romberg, S. K.; Islam, M. A.; Hershey, C. J.; DeVinney, M.; Duty, C. E.; Kunc, V.; Compton, B. G. Linking Thermoset Ink Rheology to the Stability of 3D-Printed Structures. *Addit. Manuf.* **2021**, *37*, 101621. https://doi.org/10.1016/j.addma.2020.101621.

(4) Wang, L.; Wang, C.; Wu, S.; Fan, Y.; Li, X. Influence of the Mechanical Properties of Biomaterials on Degradability, Cell Behaviors and Signaling Pathways: Current Progress and Challenges. *Biomater. Sci.* **2020**, *8* (10), 2714–2733. https://doi.org/10.1039/D0BM00269K.

(5) Decock, J.; Schlenk, M.; Salmon, J.-B. In Situ Photo-Patterning of Pressure-Resistant Hydrogel Membranes with Controlled Permeabilities in PEGDA Microfluidic Channels. *Lab. Chip* **2018**, *18* (7), 1075–1083. https://doi.org/10.1039/C7LC01342F.

(6) Ortiz-Cárdenas, J. E.; Zatorski, J. M.; Arneja, A.; Montalbine, A. N.; Munson, J. M.; Luckey, C. J.; Pompano, R. R. Towards Spatially-Organized Organs-on-Chip: Photopatterning Cell-

Laden Thiol-Ene and Methacryloyl Hydrogels in a Microfluidic Device. *Organs---Chip* **2022**, *4*, 100018. https://doi.org/10.1016/j.ooc.2022.100018.
(7) Cooke, M. E.; Rosenzweig, D. H. The Rheology of Direct and Suspended Extrusion Bioprinting. *Apl Bioeng.* **2021**, *5* (1), 011502. https://doi.org/10.1063/5.0031475.
(8) Liu, T.; Weng, W.; Zhang, Y.; Sun, X.; Yang, H. Applications of Gelatin Methacryloyl (GelMA) Hydrogels in Microfluidic Technique-Assisted Tissue Engineering. *Molecules* **2020**, *25* (22), 5305. https://doi.org/10.3390/molecules25225305.
(9) Mũnoz, Z.; Shih, H.; Lin, C.-C. Gelatin Hydrogels Formed by Orthogonal Thiol–Norbornene Photochemistry for Cell Encapsulation. *Biomater. Sci.* **2014**, *2* (8), 1063–1072. https://doi.org/10.1039/C4BM00070F.
(10) Min, S. J.; Lee, J. S.; Nah, H.; Kim, S. H.; Moon, H.-J.; Reis, R. L.; Kwon, I. K.; Heo, D. N. Development of Photo-Crosslinkable Platelet Lysate-Based Hydrogels for 3D Printing and Tissue Engineering. *Biofabrication* **2021**, *13* (4), 044102. https://doi.org/10.1088/1758-5090/ac1993.
(11) *Ultrafast, tough, and adhesive hydrogel based on hybrid photocrosslinking for articular cartilage repair in water-filled arthroscopy* | *Science Advances*. https://www.science.org/doi/full/10.1126/sciadv.abg0628 (accessed 2024-03-14).
(12) Claaßen, C.; Claaßen, M. H.; Truffault, V.; Sewald, L.; Tovar, G. E. M.; Borchers, K.; Southan, A. Quantification of Substitution of Gelatin Methacryloyl: Best Practice and Current Pitfalls. *Biomacromolecules* **2018**, *19* (1), 42–52. https://doi.org/10.1021/acs.biomac.7b01221.
(13) Zatorski, J. M.; Montalbine, A. N.; Ortiz-Cárdenas, J. E.; Pompano, R. R. Quantification of Fractional and Absolute Functionalization of Gelatin Hydrogels by Optimized Ninhydrin Assay and 1H NMR. *Anal. Bioanal. Chem.* **2020**. https://doi.org/10.1007/s00216-020-02792-5.
(14) Van Vlierberghe, S.; Fritzinger, B.; Martins, J. C.; Dubruel, P. Hydrogel Network Formation Revised: High-Resolution Magic Angle Spinning Nuclear Magnetic Resonance as a Powerful Tool for Measuring Absolute Hydrogel Cross-Link Efficiencies. *Appl. Spectrosc.* **2010**, *64* (10), 1176–1180. https://doi.org/10.1366/000370210792973550.
(15) Zhang, X.; Do, M. D.; Casey, P.; Sulistio, A.; Qiao, G. G.; Lundin, L.; Lillford, P.; Kosaraju, S. Chemical Cross-Linking Gelatin with Natural Phenolic Compounds as Studied by High-Resolution NMR Spectroscopy. *Biomacromolecules* **2010**, *11* (4), 1125–1132. https://doi.org/10.1021/bm1001284.
(16) Shestakova, P.; Willem, R.; Vassileva, E. Elucidation of the Chemical and Morphological Structure of Double-Network (DN) Hydrogels by High-Resolution Magic Angle Spinning (HRMAS) NMR Spectroscopy. *Chem. – Eur. J.* **2011**, *17* (52), 14867–14877. https://doi.org/10.1002/chem.201101334.
(17) Billiet, T.; Gasse, B. V.; Gevaert, E.; Cornelissen, M.; Martins, J. C.; Dubruel, P. Quantitative Contrasts in the Photopolymerization of Acrylamide and Methacrylamide-Functionalized Gelatin Hydrogel Building Blocks. *Macromol. Biosci.* **2013**, *13* (11), 1531–1545. https://doi.org/10.1002/mabi.201300143.
(18) Gorsche, C.; Harikrishna, R.; Baudis, S.; Knaack, P.; Husar, B.; Laeuger, J.; Hoffmann, H.; Liska, R. Real Time-NIR/MIR-Photorheology: A Versatile Tool for the in Situ Characterization of Photopolymerization Reactions. *Anal. Chem.* **2017**, *89* (9), 4958–4968. https://doi.org/10.1021/acs.analchem.7b00272.
(19) Shapiro, Y. E. Structure and Dynamics of Hydrogels and Organogels: An NMR Spectroscopy Approach. *Prog. Polym. Sci.* **2011**, *36* (9), 1184–1253. https://doi.org/10.1016/j.progpolymsci.2011.04.002.
(20) Lee, S.-H.; Moon, J. J.; Miller, J. S.; West, J. L. Poly(Ethylene Glycol) Hydrogels Conjugated with a Collagenase-Sensitive Fluorogenic Substrate to Visualize Collagenase

Activity during Three-Dimensional Cell Migration. *Biomaterials* **2007**, *28* (20), 3163–3170. https://doi.org/10.1016/j.biomaterials.2007.03.004.
(21) Fairbanks, B. D.; Schwartz, M. P.; Bowman, C. N.; Anseth, K. S. Photoinitiated Polymerization of PEG-Diacrylate with Lithium Phenyl-2,4,6-Trimethylbenzoylphosphinate: Polymerization Rate and Cytocompatibility. *Biomaterials* **2009**, *30* (35), 6702–6707. https://doi.org/10.1016/j.biomaterials.2009.08.055.
(22) Mora-Boza, A.; Mulero-Russe, A.; Caprio, N. D.; Burdick, J. A.; Singh, A.; García, A. J. Facile Photopatterning of Perfusable Microchannels in Synthetic Hydrogels to Recreate Microphysiological Environments. *Adv. Mater. n/a* (n/a), 2306765. https://doi.org/10.1002/adma.202306765.
(23) Hoorick, J. V.; Gruber, P.; Markovic, M.; Rollot, M.; Graulus, G.-J.; Vagenende, M.; Tromayer, M.; Erps, J. V.; Thienpont, H.; Martins, J. C.; Baudis, S.; Ovsianikov, A.; Dubruel, P.; Vlierberghe, S. V. Highly Reactive Thiol-Norbornene Photo-Click Hydrogels: Toward Improved Processability. *Macromol. Rapid Commun.* **2018**, *39* (14), 1800181. https://doi.org/10.1002/marc.201800181.
(24) Tang, T.; Liu, C.; Min, Z.; Cai, W.; Zhang, X.; Li, W.; Zhang, A. Microfluidic Fabrication of Gelatin Acrylamide Microgels through Visible Light Photopolymerization for Cell Encapsulation. *ACS Appl. Bio Mater.* **2023**, *6* (6), 2496–2504. https://doi.org/10.1021/acsabm.3c00307.
(25) *Precise control of synthetic hydrogel network structure via linear, independent synthesis-swelling relationships | Science Advances*. https://www.science.org/doi/full/10.1126/sciadv.abe3245 (accessed 2023-11-24).

6. Conclusion and Future Directions

6.1 Conclusions

Within this dissertation, I illustrated advancements in tissue engineering, biomaterials science, and analytical chemistry toward the goal of modeling human immunity. As was stated in **chapter 1**, there exists a dire need to better model human tissue to enable future research and drug efficacy testing. In particular, human immunity remains among the most challenging systems to model, and the largest gap in current tissue engineering modeling capability is of the immune system. Despite the challenges, the past two decades of pioneering advancements in the organ-on-chip field are enabling for change in the near future.

In **Chapter 2**, I led the design prototyping, validation, and application of a tissue engineered model of the human T/B border zone. The system was demonstrated as being capable of naïve-to-effector lymphocyte differentiation, monitoring cell motility in real time, and facilitating T cell help for b cell activation, which is an essential process for understanding the response to infection and vaccine. As an example of drug-efficacy testing, an immunosuppressant drug was used to predictively inhibit T/B interactions.

To facilitate broader impact of the lymph node microphysiological system, **chapter 3** describes how the device was fabricated in an alternative material more suitable for manufacturing at scale and preventing small molecule absorption.

In a shift toward making fundamental advancements, **chapter 4** begins with a prelude that outlines prior work to enable *in situ* photopatterning. This advanced biofabrication approach enables precise control over the spatial organization within organ-on-chip models, but also adversely affected lymphocyte viability. My involvement in testing cell viability within photocured gels is discussed briefly. The dissertation shifts at this point toward the development of analytical methods to characterize photopolymerizing biomaterials. The main body of chapter 4 describes the assays for the quantification chemical modification on gelatin hydrogels. The DoF

measurement described here has been used to measure the functionalization of photopolymerizing gels within numerous laboratories around the world.

Chapter 5 expands upon methods for characterizing photopolymerizable biomaterials by further modifying the method to enable hydrogel reaction monitoring. This novel method for analyzing crosslinking density within hydrogels was applied toward predicting biomaterial stability.

Overall, the work described herein enables the Pompano lab to continue the development of advanced analytical tools toward modeling immunity for years to come. On a broader level, the impact of this work is evident in that **(a) the need for more human-relevant models of adaptive immunity was met**, and (b) analytical methods for characterizing complex biomaterials have been developed.

6.2 Future Directions

6.2.1 Future applications of the T/B border model

Modeling the Vaccine Response

As the T/B border model was successfully demonstrated to model Tfh skewing, T cell help, and plasmablast formation, an obvious next direction is to expand the platform toward modeling additional steps of the vaccine response, such as antigen drainage or T/DC crosstalk, for example. Expanding the LN MPS in this way will require overcoming new obstacles, such as accounting for low lymphocyte precursor frequency, for example (See Intro 1.3). This grand vision is currently unfolding within in the Pompano Lab, as plans to convert the LN MPS into a device capable of viewing a vaccine response have been officially proposed. While I have contributed to those ideas, they are not entirely my own. As such, they will not be discussed at length here. However, in reference to this aim, it is worth stating that the tools validated in chapter 2 will be vital to the success of the next stage of this project. I feel confident in the lab's

future success. Next, I will describe a proposal for enhancing the LN MPS to allow for culture of neurons with immune cells.

Proposal for modeling Neuroimmunity-on-a-chip

In the early response to infection, the immune system communicates with the nervous system.[1,2] In areas susceptible to infection (ex. the skin), immune cells cluster around the axon terminals of pain receptors known as nociceptive neurons, which communicate via neuropeptides. Remarkably, most lymphocytes both produce and express receptors for almost all known neuropeptides, suggesting that they communicate with neurons. The environment where immune cells and axon terminals communicate is unique and not reproducible by conventional cell culture methods. Axons extend from the spinal cord into a peripheral organ so that immune cells only interact with the receptive field of the neuron. Studying this interaction by *in vivo* models is challenging due to the numerous cell types present. This may explain why the neuropeptides calcitonin gene-related peptide (CGRP), vasoactive intestinal peptide (VIP), and somatostatin have been characterized as both pro- and anti-inflammatory[1,3,4]. Because of the ambiguity regarding the role of neuropeptides and a lack of appropriate experimental models, our understanding of the fundamental cell-cell communication that drives immunity is incomplete.

The spatial and temporal features of neuron-immune cell signaling can be sustained by combining microfluidic design elements used for observing cortical-striatal neuron networks[5] (Figure 1) with the chip used for the LN MPS (Chapter 2). Microfluidic ladder designs have been optimized to encourage neuronal axon projection through channels,

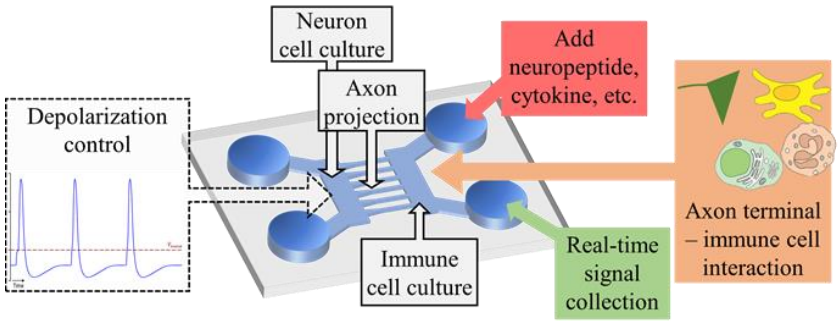

Figure 6-1 A microfluidic device for producing a neuron-immune cell signaling environment. Axon projection channels allow for immune cells to interact with the axon terminals only. The depolarization of neurons, levels of neuropeptides, and levels of cytokines can be controlled and interactions could be easily imaged with a microscope.

and these chips have been mainly utilized to study neuron-neuron interactions. In this application, nociceptive neurons and immune cells could be grown in separate culture chambers connected fluidically with the ladder design.

After establishing baseline neural growth, for example with MAP2 staining, as well as inflammatory cytokine and neuropeptide secretion, the effect of neuronal coculture on inflammation could be easily investigated.

Effect of nociceptive neuron depolarization on inflammation. When a neuron depolarizes, ion channels allow for sodium, potassium, and calcium ions to be transported in such a way that an electrical pulse travels from the cell body toward the axon terminal resulting in the release of neurotransmitters at the axon terminal. Neurons could be depolarized by adding potassium ions to the neuron cell culture. A fluorescent calcium indicator (fluor-4) could validate this. Changes in calcium levels, indicating depolarization, could then be measured with live-cell imaging.

A key link between the innate and adaptive immune responses occurs when dendritic cells travel to the lymph node after exposure to antigen. To investigate how nociceptive neurons are involved in this process, neurons could be deliberately depolarized by adding potassium to the neuron cell body culture chamber. The effect of depolarization on cell motility and secreted inflammatory cytokines could be monitored, as was demonstrated in the T cell stimulation experiments shown in chapter 2.

A neuro-immune cell signaling chip would clarify our understanding of the interactions between the two complex living systems: immunity and the central nervous system. Examining the interactions of axon terminals with immune cells on a microfluidic chip is entirely novel. Clarifying the specific roles of neuropeptides as well as the general role of nociceptive neurons in the innate immune response would expand our understanding of the immune response.

6.1.2 Future applications of *in situ* photopatterning system

Our initial attempt to model lymph node physiology with *in situ* photopatterning was stalled when we observed low lymphocyte viability within photopatterned gels. This critical failure required us to pivot away from photocrosslinking gel chemistry, and efforts to improve viability by tuning the gel chemistry have been challenging. Despite this, there are still aspects of photopatterning, such as the ability to generate follicle-like structures and non-linear flow paths, that are uniquely enabling for modeling tissue. Here, I will describe an application of the photopatterning method that aligns with what we now know about maintaining viable lymphocyte cultures.

Photopatterning biomimetic chemokine gradients to model Systemic Lupus Erythematosus (SLE).

Autoimmune disorders such as Systemic Lupus Erythematosus (SLE) are most often characterized by an overactive immune system. SLE, in particular, is due to dysregulation in B cell activity that results in rashes, inflammation, and kidney disease.[6,7] One underlying hallmark of SLE is that B cells become spatially dysregulated. Specifically, B cells over-express CXCR4, similar to when plasmablasts upregulate CXCR4 in response to acute infection, resulting in chronic disruption of the CXCR4/CXCL12 chemokine axis[6]. This constant B cell "response" causes chronic inflammation. Despite immunosuppressants being available as an effective treatment, there is no cure and the treatment leaves patients immunocompromised.[7,8]

Having tested immunosuppressant efficacy and modeled chemotaxis in the LN MPS in chapter 2 of this dissertation, one might assume the same system could be used to the test the effect of JAK inhibition on chemotactic responsiveness of cells. By generating human lupus B cells with CRISPR[9], or adding SLE patient cells directly to the chip, a SLE-LN model, capable of predicting therapeutic efficacy, would be generally straightforward to make. An SLE-LN model would provide mechanistic insight into a key feature of SLE, in particular with regard to how SLE

B cell motility toward a CXCL12 gradient might differ from homeostatic B cells. Toward this aim, I attempted to model CXCL12 and CXCL13 chemotaxis of T and B lymphocytes on the LN MPS (data not shown).

However, these attempts were generally unsuccessful. This is likely because *in vivo*, chemokine gradients are more complex than the linear gradient generated within the LN MPS (Fig 6-2). Some gradients, such as CCL21, act as attractants for cells across great distances (>1 cm) from the source.[10] Other gradients, in contrast, act as local stimulants across much smaller (20-100 µm) distances. CXCL13 for example, is involved in facilitating T/B interactions at the B cell follicle of the lymph node. Plasmablasts and over-active SLE B cells respond to a CXCL12 gradient that encourages egress. Linear chemokine gradient generators are not often designed with this level of spatial control, both with regard to the high concentration of chemokine at the source, and the follicle-shaped structures.[11]

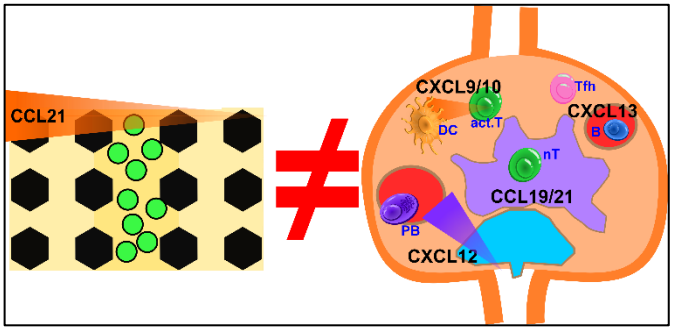

***Figure 6-2*. Chemokine gradients in tissue are not linear.** Many (CXCL13, 12, 9, 10) exist in follicle-like features and act locally across small distances. Others (CCL21) act across great lengths.

***In situ* photopatterning may enable more biomimetic chemokine gradients.**

I serendipitously discovered a unique spectacle while photopatterning that should be explored further: Chemokines, when mixed with gel precursor prior to photopatterning, become immobilized (Fig 6-3). When photopatterning a circular feature containing fluorescently-tagged CCL21, I saw an initial 40% decrease in signal within 24 hr, which then remained constant for 3 days. In addition, adding the chemokine-binding extracellular matrix component, heparin sulfate, increased the amount of chemokine contained within the gel. **More surprising was the observation that photopatterned-immobilized chemokines retained their chemotactic activity (Fig 6-3c).** Fluorescently tagged CD4+ T cells were seen clustered around the photopatterned chemokine source after 3 hr culture.

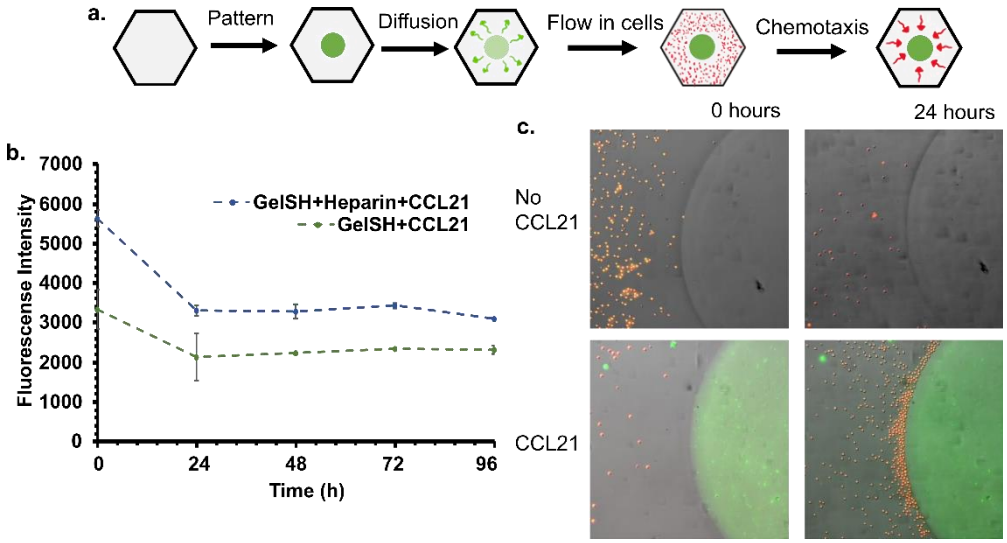

Figure 6-3 Photopatterned chemokines become immobilized and retain their activity. (a) approach for photopatterning chemokines. (b) AF488-labeled CCL21 was mixed with gelSH-pegNB hydrogel and photopatterned with a circular photomask. The fluorescence intensity within the feature was measured for 96 hours. (c) NHS rhodamine labeled cells were flown into the chip, and were observed clustering near the photopatterned chemokine source.

The utility of this phenomenon is clear when considering the need for more biomimetic chemokine gradients, as in the case for modeling SLE. Having this tool, I propose an SLE-LN, constructed as a hybrid between the surface-tension chip and *in situ* photopatterning method (Fig. 6-4). The use of the surface-tension chip would enable the loading of thermally-setting collagen/fibrinogen gel, which has already been demonstrated to be biocompatible (chapter 2).

This SLE model would be validated by recapitulating the phenomenon of overexpressing CXCR4+ B cells migrating irregularly. This underlying SLE phenomenon could then be tested with immunosuppressants or other therapeutics to assess efficacy. Alternatively, mechanistic studies could be performed to study the phenomenon in a *in vivo* like system. One would expect a CXCR4 KO cell[12], or the testing of a recently investigated CXCR4-blocker[13], to stop migration to CXCL12. A SLE-LN, capable of both fundamental- and translationally-relevant readouts, would enable deeper mechanistic study and more informative drug-readouts.

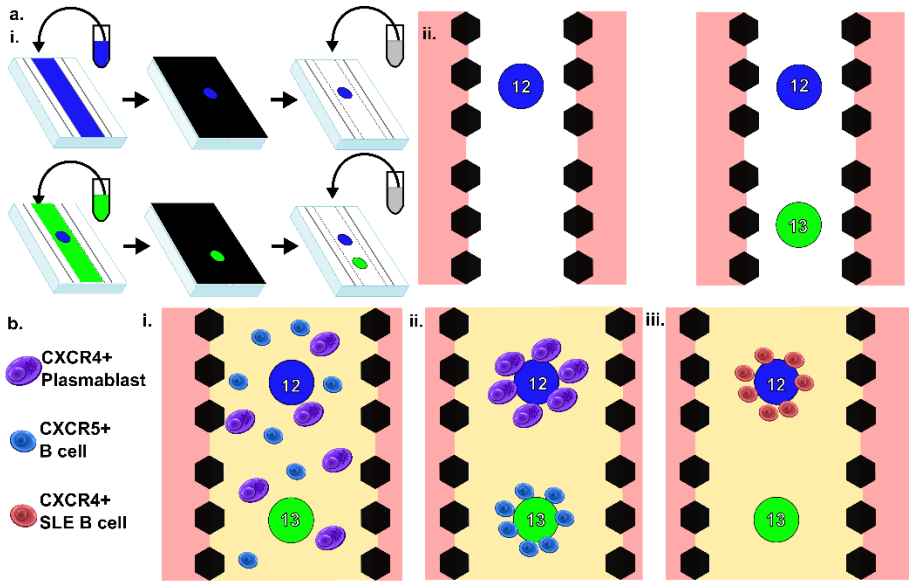

Figure 6-4. Photopatterning chemokine sources to model SLE B cell dysregulation.
(a) (i) Approach. By photopatterning chemokine laden gel sequentially, multiple chemokines could be photopatterned within a microfluidic chamber. (ii) Schematic of chip after chemokine photopatterning with CXCL12 and CXCL13. (b) (i) After chemokine patterning, cell-laden hydrogel could be loaded into the lane, and should surround the patterned chemokine sources. (ii) As positive controls, one would predict CXCR4+ plasmablasts to cluster near a CXCL12 source, and CXCR5+ effector B cells to cluster around a CXCL13 source. (iii) As a model of SLE, one would expect over-expressing CXCR4+ B cells to cluster around a CXCL12 source.

6.2.3 Future directions for characterizing photopolymerizing hydrogels

The DoF and DoC measurements described in chapter 4 and 5 were described for characterizing hydrogels composed entirely of crosslinkable base-ingredients. For example, gelMA only contains methacryl-modified gelatin, and gelSH-pegNB only contains monomers capable of making SH-NB linkages. While these materials are widely used in the biomaterials field today, another class of emerging biomaterials is hydrogel blends. The prelude in chapter 4, for example, describes how adding collagen to gelSH-pegNB improved biocompatibility. Yet, that hydrogel composition was not stable when used in photopatterning applications.

The crosslinking environment of these blended hydrogels is complex and should be investigated with the DoC measurement described in chapter 5. In particular, I hypothesize that adding collagen to a gelSH-pegNB hydrogel may sterically interfere with the crosslinking, and

crosslinking may not approach the theoretical limit as shown in Fig. 5-4. If true, one may decide to improve crosslinking by chemically modifying the collagen fibers.

Another approach to consider with this class of hydrogels is how the fibers thermally gel in relation to the photocrosslinks. When developing the approach to use a collagen-gelSH-pegNB gel within our lab, it was not clear to use if allowing thermal gelation prior to photocrosslinking would affect the density of the resulting gel. The DoC measurement described in chapter 5 would shed light on this complex system by showing if crosslinking rate or extent of crosslinking was affected by thermal gelation. In conclusion, the knowledge gained from the DoC measurement will impact the overall strategy for employing hydrogel blends in various settings.

6.3 References

(1) Talbot, S.; Foster, S. L.; Woolf, C. J. Neuroimmunity: Physiology and Pathology. *Annu. Rev. Immunol.* **2016**, *34* (1), 421–447. https://doi.org/10.1146/annurev-immunol-041015-055340.

(2) Rankin, L. C.; Artis, D. Beyond Host Defense: Emerging Functions of the Immune System in Regulating Complex Tissue Physiology. *Cell* **2018**, *173* (3), 554–567. https://doi.org/10.1016/j.cell.2018.03.013.

(3) Rochlitzer, S.; Veres, T. Z.; Kühne, K.; Prenzler, F.; Pilzner, C.; Knothe, S.; Winkler, C.; Lauenstein, H.-D.; Willart, M.; Hammad, H.; Müller, M.; Krug, N.; Lambrecht, B. N.; Braun, A. The Neuropeptide Calcitonin Gene-Related Peptide Affects Allergic Airway Inflammation by Modulating Dendritic Cell Function. *Clin. Exp. Allergy* **2011**, *41* (11), 1609–1621. https://doi.org/10.1111/j.1365-2222.2011.03822.x.

(4) Kashem, S. W.; Riedl, M. S.; Yao, C.; Honda, C. N.; Vulchanova, L.; Kaplan, D. H. Nociceptive Sensory Fibers Drive Interleukin-23 Production from CD301b+ Dermal Dendritic Cells and Drive Protective Cutaneous Immunity. *Immunity* **2015**, *43* (3), 515–526. https://doi.org/10.1016/j.immuni.2015.08.016.

(5) Peyrin, J.-M.; Deleglise, B.; Saias, L.; Vignes, M.; Gougis, P.; Magnifico, S.; Betuing, S.; Pietri, M.; Caboche, J.; Vanhoutte, P.; Viovy, J.-L.; Brugg, B. Axon Diodes for the Reconstruction of Oriented Neuronal Networks in Microfluidic Chambers. *Lab. Chip* **2011**, *11* (21), 3663–3673. https://doi.org/10.1039/C1LC20014C.

(6) Wang, A.; Guilpain, P.; Chong, B. F.; Chouzenoux, S.; Guillevin, L.; Du, Y.; Zhou, X. J.; Lin, F.; Fairhurst, A.-M.; Boudreaux, C.; Roux, C.; Wakeland, E. K.; Davis, L.; Batteux, F.; Mohan, C. Dysregulated Expression of CXCR4/CXCL12 in Subsets of Patients with Systemic Lupus Erythematosus. *Arthritis Rheum.* **2010**, *62* (11), 3436–3446. https://doi.org/10.1002/art.27685.

(7) Zhao, L.; Liang, D.; Wu, X.; Li, Y.; Niu, J.; Zhou, C.; Wang, L.; Chen, H.; Zheng, W.; Fei, Y.; Tang, F.; Li, Y.; Zhang, F.; He, W.; Cao, X.; Zhang, X. Contribution and Underlying Mechanisms of CXCR4 Overexpression in Patients with Systemic Lupus Erythematosus. *Cell. Mol. Immunol.* **2017**, *14* (10), 842–849. https://doi.org/10.1038/cmi.2016.47.

(8) Kubo, S.; Yamaoka, K.; Kondo, M.; Yamagata, K.; Zhao, J.; Iwata, S.; Tanaka, Y. The JAK Inhibitor, Tofacitinib, Reduces the T Cell Stimulatory Capacity of Human Monocyte-Derived Dendritic Cells. *Ann. Rheum. Dis.* **2014**, *73* (12), 2192–2198. https://doi.org/10.1136/annrheumdis-2013-203756.
(9) Lee, M. H.; Shin, J. I.; Yang, J. W.; Lee, K. H.; Cha, D. H.; Hong, J. B.; Park, Y.; Choi, E.; Tizaoui, K.; Koyanagi, A.; Jacob, L.; Park, S.; Kim, J. H.; Smith, L. Genome Editing Using CRISPR-Cas9 and Autoimmune Diseases: A Comprehensive Review. *Int. J. Mol. Sci.* **2022**, *23* (3), 1337. https://doi.org/10.3390/ijms23031337.
(10) Luther, S. A.; Bidgol, A.; Hargreaves, D. C.; Schmidt, A.; Xu, Y.; Paniyadi, J.; Matloubian, M.; Cyster, J. G. Differing Activities of Homeostatic Chemokines CCL19, CCL21, and CXCL12 in Lymphocyte and Dendritic Cell Recruitment and Lymphoid Neogenesis. *J. Immunol.* **2002**, *169* (1), 424–433. https://doi.org/10.4049/jimmunol.169.1.424.
(11) Wang, X.; Liu, Z.; Pang, Y. Concentration Gradient Generation Methods Based on Microfluidic Systems. *RSC Adv.* **2017**, *7* (48), 29966–29984. https://doi.org/10.1039/C7RA04494A.
(12) Boehnke, J.; Atakhanov, S.; Toledo, M. A. S.; Schüler, H. M.; Sontag, S.; Chatain, N.; Koschmieder, S.; Brümmendorf, T. H.; Kramann, R.; Zenke, M. CRISPR/Cas9 Mediated CXCL4 Knockout in Human IPS Cells of Polycythemia Vera Patient with JAK2 V617F Mutation. *Stem Cell Res.* **2021**, *55*, 102490. https://doi.org/10.1016/j.scr.2021.102490.
(13) Zhao, R.; Liu, J.; Li, Z.; Zhang, W.; Wang, F.; Zhang, B. Recent Advances in CXCL12/CXCR4 Antagonists and Nano-Based Drug Delivery Systems for Cancer Therapy. *Pharmaceutics* **2022**, *14* (8), 1541. https://doi.org/10.3390/pharmaceutics14081541.